Autoresonance in Stimulated Raman Scattering

Chapman Docteur Thomas

To cite this version:

Chapman Docteur Thomas. Autoresonance in Stimulated Raman Scattering. Plasma Physics [physics.plasm-ph]. Ecole Polytechnique X, 2011. English. NNT : . pastel-00674111

HAL Id: pastel-00674111
https://pastel.hal.science/pastel-00674111v1

Submitted on 25 Feb 2012

Thèse

présentée pour obtenir le grade de

Docteur de l'Ecole Polytechnique

Specialité : Physique Théorique

par

Thomas D. CHAPMAN

Autoresonance in Stimulated Raman Scattering

soutenue le 22 Novembre 2011 devant le jury composé de

M.	Tony Bell	Senior Research Fellow, Department of Physics, University of Oxford, England	Rapporteur
M.	Michel Casanova	Ingénieur de recherche au CEA, CEA/Bruyères-le-Châtel, France	
M.	Alain Ghizzo	Professeur des Universités, LPMIA, Nancy, France	Rapporteur
M.	Stefan Hüller	Directeur de Recherche, CPHT, Ecole Polytechnique, France	Co-directeur de thèse
Mme.	Christine Labaune	Directrice de Recherche, LULI, Ecole Polytechnique, France	Présidente du jury
M.	Paul-Edouard Masson-Laborde	Ingénieur de Recherche au CEA, CEA/Bruyères-le-Châtel, France	
M.	Jean-Marcel Rax	Directeur de Recherche, LOA, Ecole Polytechnique, France	
M.	Wojciech Rozmus	Professor of Physics, Department of Physics, University of Alberta, Canada	Co-directeur de thèse

Abstract

Stimulated Raman scattering (SRS) is studied in plasmas relevant to inertial confinement fusion (ICF) experiments. The excitation of autoresonant Langmuir waves in inhomogeneous plasmas is investigated as a mechanism for the enhancement of SRS in the kinetic regime ($k_L\lambda_D > 0.25$). It is shown that weakly kinetic effects like electron trapping, described via an amplitude-dependent frequency shift, may compensate the dephasing of the three-wave resonance of SRS that normally occurs in inhomogeneous plasmas. Under conditions relevant to current and future ICF experiments (National Ignition Facility, Laser Mégajoule), a simple analytical model is found to predict to good accuracy the observed growth, saturation and phase of Langmuir waves, in both three-wave coupling and kinetic (particle-in-cell) simulations. Through autoresonance, observed SRS levels far exceed the spatial amplification expected from Rosenbluth's model in an inhomogeneous profile [M. N. Rosenbluth, Phys. Rev. Lett. **29**, 565 (1972)]. A potential application of autoresonance is proposed in the form of a Raman amplifier.

La diffusion Raman Stimulée (DRS) est étudiée dans le contexte des plasmas qui sont pertinents pour la Fusion par Confinement Inertielle (FCI). Dans un plasma inhomogène le processus d'auto-résonance de l'onde Langmuir, générée par DRS, peut se produire dans le régime cinétique ($k_L\lambda_D > 0.25$*) et conduire à des amplitudes au delà du niveau de l'amplification attendue due à l'inhomogénéité selon Rosenbluth [M. N. Rosenbluth, Phys. Rev. Lett.* ***29****, 565 (1972)]. On démontre que des effets cinétiques faibles, comme le piégeage d'électrons donnent lieu à un décalage de fréquence non-linéaire (dépendant de l'amplitude), et peuvent compenser le déphasage de la résonance de DRS des trois ondes, observé dans les plasmas inhomogènes. Un modèle analytique du processus d'auto-résonance décrivant à la fois la croissance, la saturation et la phase des ondes de Langmuir a été développé. Ce modèle est en excellent accord avec les résultats des simulations cinétiques (particle-in-cell) pour des paramètres proches des conditions des plasmas des expériences de la fusion laser (Laser Mégajoule, National Ignition Facility). Une application possible de l'autorésonance est proposée sous la forme d'un amplificateur de Raman.*

Foreword

Many people deserve praise and thanks for helping me during my thesis. Dr. Hüller has been dedicated, patient, and extremely generous with his time. I am indebted to him for assisting me through every stage of this thesis programme, from supporting my application for a place and funding at the Ecole Polytechnique, to the defence of my thesis three years and three months later and beyond. Prof. Rozmus has helped me greatly over the course of this thesis, providing invaluable assistance to my work at pivotal moments and organising additional funding to support my time at the University of Alberta. From the early stages of my work, Dr. Paul-Edouard Masson-Laborde has helped me a great deal, both performing simulations at the CEA relevant to my work and offering me advice when modifying and running Particle-in-Cell (PIC) codes from his own vast experience with them. The PIC code developed by Dr. Anne Héron and Dr. Jean-Claude Adam was ultimately the PIC code used to produce the results that went into published work during my thesis; Dr. Héron's assistance in modifying and running this code was essential to this work. Dr. Denis Pesme has been of great help, lending his expertise in the field of parametric instabilities and making important improvements to the publications that arose from this thesis.

The principle inspiration for the work undertaken in this thesis originally arose from a conversation between Prof. Wojciech Rozmus and Dr. Stefan Hüller, who noted in 2008 that similar work undertaken by Dr. Oded Yaakobi, under supervision from Prof. Lazar Frièdland, could be applied to plasmas in a regime relevant to fusion. The suggestion was then made that I look at the possibility of autoresonance in a simple single-equation model, incorporating basic physics arising in the so-called kinetic regime that is known to be of importance to current experiments in fusion.

Based on the positive results of this initial study, a three-wave model was made and studied. The results of these studies formed the first peer-reviewed publication to come out of my time at Ecole Polytechnique. When applying at the Ecole Polytechnique, I simultaneously applied for funding that gave me the opportunity to spend time abroad from France at another institution. It was through Dr. Hüller that I met Prof. Rozmus, and it was my time at the University of Alberta, Canada, that led to further articles on the subject of autoresonance that made use of PIC codes.

My academic career would not have been possible without the past and continued support of my family, to whom this thesis is dedicated.

Biographical note

Thomas Daniel Chapman was born in Oxford, England, and was raised near Cambridge until age 18. He entered Magdalen College, Oxford, in 2004, where he read physics and graduated from the M.Phys. program with 1st class honours in 2008. In 2008, Thomas began a Ph.D. at the Ecole Polytechnique in Palaiseau, France, where he graduated in 2011. His interests lie in a broad range of fusion-relevant physics, motivated by the ever-growing need for a clean, long-term solution to the world's energy requirements.

Overview

This thesis summarises a study of the impact of spatial autoresonance on the evolution of stimulated Raman scattering in warm plasmas. Due to the high light intensities encountered and the small temporal and spatial scales over which inertial confinement fusion experiments are conducted, directly observing the inner workings of laser-plasma interactions under such conditions is rarely possible. Various diagnostics present pieces of information that, when taken together, present a picture that is at best incomplete. Much of the physics responsible for experimental observations is poorly understood, but with the arrival of ever higher-powered lasers and improved engineering techniques, progress in the field of inertial confinement fusion is perhaps faster now than ever.

Kinetic simulations that model the behaviour of individual particles in plasmas provide a means to test our understanding of laser-plasma interaction and offer the possibility of guiding experimental work down fruitful avenues. However, even these computational results frequently remain difficult to interpret. Reduced models that strip away less important physical phenomena allow a concrete understanding of the key processes responsible for the behaviour of laser light in plasma. While not intended as models of real experiments, they offer invaluable insight into the relevant physics.

This thesis uses various models to demonstrate the possibility of autoresonance in plasmas. With a few relatively simple equations, the behaviour of complex kinetic simulations is reproduced, reflecting a good understanding of the important physical process at work. This thesis is organised in the following way:

Chapter 1

The context of this thesis is presented. The importance of stimulated Raman scattering in current ICF experiments is described, in addition to other relevant wave interactions present in warm plasmas.

Chapter 2

The equations necessary to described stimulated Raman scattering and autoresonance in plasmas are derived.

Chapter 3

Autoresonance is demonstrated using Langmuir waves driven by a prescribed ponderomotive force. A Hamiltonian approach is taken to explain the key features of autoresonance.

Chapter 4

Autoresonance is demonstrated in three-wave coupling simulations in linear and parabolic density profiles. Autoresonance is discussed in the context of a Raman amplifier.

Chapter 5

The plasma reflectivity in density profiles that increase in the direction of the high-frequency laser propagation is compared to the plasma reflectivity in those that decrease in the same direction. Reflectivity enhancement due to autoresonance is observed in kinetic simulations, and the results of kinetic and fluid simulations are compared.

Chapter 6

The findings of this thesis are summarised and future work discussed.

Contents

List of Figures

Chapter 1

Introduction to LPI and autoresonance

1.1 Laser plasma interaction

Laser plasma interaction (LPI) describes the wide array of physical processes that may take place as an intense electromagnetic wave propagates through plasma. The electromagnetic waves may modify the plasma, driving matter waves and reshaping the fluid-like distribution of ions and electrons that make up the plasma. These changes in the plasma may then in turn alter the laser light, redirecting, scattering or absorbing it, often leading to complex nonlinear phenomena.

Interaction between laser light and plasma arises in countless experiments and industrial applications, either by design or to the detriment of the task at hand. One field in which LPI plays both the role of hero and villain is inertial confinement fusion (ICF): In laser-driven ICF schemes, the goal is to deposit laser energy at a particular density in the plasma in order to drive the compression and subsequent heating of a target pellet of hydrogen. If the target is compressed sufficiently, it may undergo fusion, leading to the release of a large amount of energy. However, the laser may interact with the plasma at a density different to that which is intended, leading to myriad undesirable effects and preventing the effective implosion of the target.

1.2 Fusion

The ultimate goal of fusion energy research is to achieve the net gain in energy that is theoretically possible through the harnessing of the energy released by the fusion of light nuclei. In order to bring the nuclei sufficiently close together that they may undergo fusion, it is necessary to overcome the energy barrier posed by the Coulomb interaction. It is in fact sufficient for the nuclei to have a kinetic energy that is close but inferior to this barrier, owing to the ability of the nuclei to undergo quantum tunneling. The likelihood of two nuclei undergoing fusion at a particular kinetic energy in the centre-of-mass frame is described by their "cross-section". This quantity is a useful measure of the viability of a particular fusion process. The fusion of deuterium (D) and tritium (T) nuclei is known to have a comparatively large cross-section at realistically achievable kinetic energies, and releases a significant amount of energy. The mechanism is the following:

$$\mathrm{D} \;+\; \mathrm{T} \;\;\longrightarrow\;\; \alpha(3.5\,\mathrm{MeV}) \;+\; \mathrm{n}(14.1\,\mathrm{MeV}) \tag{1.1}$$

where α is the alpha particle and n is the unbound ejected neutron. Other so-called "advanced" fuel mixtures that when undergoing fusion release energy in the more practical form of charged particles have been proposed. However, due to the lower cross-sections of these mixtures at energies that can currently or foreseeably be practically achieved, all major current ICF experiments use a DT mixture.

The density, temperature control and symmetry required to fuse nuclei are dauntingly difficult to realise. The Sun, like all active stars, achieves the necessary density and confinement of the plasma through its crushing gravitational pressure; the density and sheer size of the sun provide conditions conducive to the fusion of an array of elements. These conditions are not reproducible on earth. Nor indeed would doing so be useful since, at 276.5 Wcm^{-3}, the net energy produced per unit volume at the core of the Sun is equivalent only to that of a lizard's metabolism. The two methods of achieving fusion on earth that have gathered most research interest and recent funding are magnetic confinement fusion, where strong magnetic fields are used to balance the fluid pressure of the plasma, and inertial confinement fusion (ICF), where typically laser energy is used to provide the necessary compression of the plasma. It is this second method, laser-driven ICF, that is the method to which the results of this thesis are applicable. Laser-driven ICF, referred to henceforth in this thesis as simply ICF, may be further subdivided into two approaches, called simply direct-drive and indirect-drive.

1.3 Direct- and indirect-drive ICF

In direct-drive ICF, a target is directly irradiated by laser light. The laser light is typically applied in the form of a large number of beams in order to irradiate the target as symmetrically as possible to ensure the efficient spherical compression of the target. This method is currently employed on a number of laser facilities, including the OMEGA laser in Rochester (USA) and the GEKKO/LFEX laser in Osaka (Japan). At the LULI at École Polytechnqiue (Palaiseau, France),

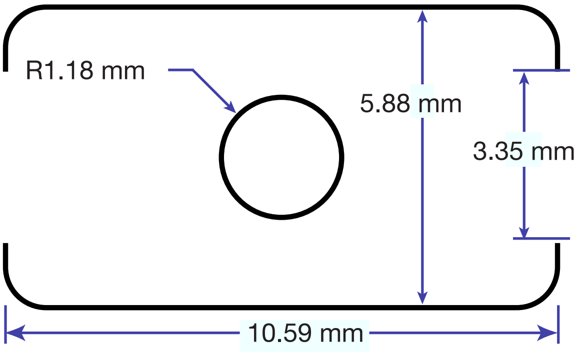

Figure 1.1: Cross-section of a hohlraum and target, designed for ignition at the NIF. Figure adapted from Ref.[1].

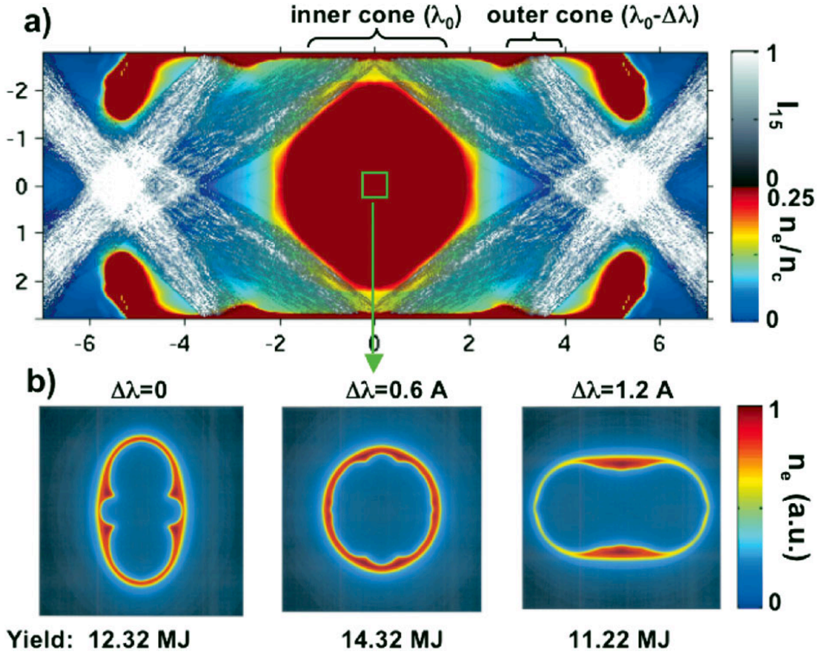

Figure 1.2: (a) Simulation of a hohlraum undergoing laser irradiation. The figure was generated with the radiative hydrodynamics LASNEX code at the NIF. (b) The fuel pellet undergoing compression with a range of beam energy distributions. Figure adapted from Ref.[2].

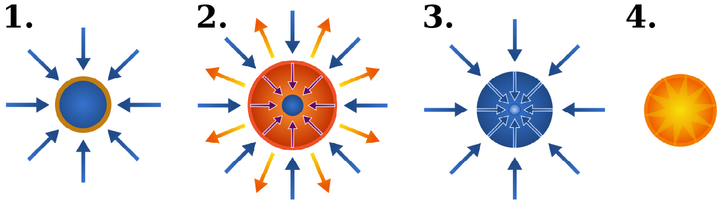

Figure 1.3: The four stages of target implosion during laser-driven ICF. 1. The target is irradiated (blue arrows) either directly by laser light or indirectly via laser-generated x-rays, leading to the formation of a plasma corona. 2. Ablation of high-temperature surface material (orange arrows), and compression of the target (purple arrows). 3. The target size decreases rapidly and shock waves converge at the core. 4. The remaining fuel undergoes fusion, releasing energy. Figure adapted from Ref.[3].

direct drive experiments are performed in order to study fundamental physics. The coming PETAL facility will provide the necessary laser intensities to study a range of direct drive schemes, in particular so-called fast ignition.

The quality and uniformity of the high number of beams required for sufficiently spherical irradiation of the target in direct-drive schemes poses a number of engineering problems. A potential solution to these obstacles is proposed in the form of a *hohlraum*. The hohlraum is a typically cylindrical high-Z metal (such as gold) cage, with openings at both ends of its principle axis (see Fig. 1.1). Laser light is then introduced through these openings, irradiating the inner walls of the hohlraum and heating the metal. The heated walls generate large quantities of X-rays, with a radiation temperature of around $200 - 300$ eV. Although significantly less efficient than direct drive schemes due to the intermediate interaction of the laser light with the hohlraum before reaching the target (and the simple geometrical consideration that many X-rays miss the target), the geometry of the hohlraum may be fine-tuned so as to provide a highly symmetric target irradiation. Indirect drive fusion is the primary approach to fusion being investigated at the National Ignition Facility (NIF) in Lawrence Livermore National Laboratories (LLNL), USA, and the Laser Mégajoule (LMJ) in Bordeaux, France. A simulated cross-section of a hohlraum undergoing laser illumination is shown in Fig. 1.2a, generated with the radiative hydrodynamics LASNEX code at the NIF. Below (Fig. 1.2b), three figures show the target during implosion for different beam configurations. The central image of implosion is the most symmetric and therefore efficient result, producing the highest energy yield.

In both direct and indirect schemes, the eventual mechanism is identical: Laser light, either directly or indirectly via the walls of the hohlraum, irradiates a cryogenically frozen DT pellet, encased in a thin shell of composite materials. The laser is absorbed at the surface of the target, quickly forming a plasma corona that surrounds the target. Ablation of the outer layer of the target drives the compression of the remaining fuel through the rocket-like blow-off of hot surface material, causing the density of the rapidly shrinking target to increase dramatically. Shock waves then converge at the core of the target, finally producing the conditions necessary for fusion. The remaining fuel then undergoes fusion, releasing energy. The stages of implosion are shown in Fig. 1.3.

1.4 LPI in the corona

At the NIF, both direct- and indirect-drive experiments are performed in what is initially a vacuum. The laser passes therefore from a vacuum through a plasma of generally increasing density until it is absorbed or scattered out of the plasma. For driving matter ablatively with laser beams, the preferred mechanism of energy deposition is inverse bremsstrahlung (commonly referred to as collisional absorption) near the “critical density” n_c, the density at which the laser interacts resonantly with the plasma. Collisional absorption is desirable since the deposited energy is thermalised locally (important for the precise timing required for successful ICF), while other absorption or scattering mechanisms typically drive waves that propagate before thermalising.

Near the critical density, two other classes of energy absorption in addition to collisional absorption are typically defined: resonance absorption, and scattering by wave excitation. The oblique incidence of laser light on a plasma with a density gradient allows for resonance absorption, where the component of the electromagnetic field parallel to the vector along which the gradient changes is non-zero (in the maximal case, this is described as p-polarised light), resonantly driving an electron-plasma wave at a density of $n_c \sin^2 \theta$, where θ describes the angle between the wave vector of the incident laser light and the density gradient vector. Laser light may also drive a variety of electrostatic waves by coupling to them through the “ponderomotive force”. These couplings are the basis of *parametric instability*, and may occur at densities well below n_c. Parametric instabilities, and in particular stimulated Raman scattering, are discussed at length later in the chapter.

In the 1980s, experiments testing the absorption of laser light were performed using CO_2 lasers, operating with a wave length of $\lambda_0 = 10\ \mu$m. These CO_2 lasers, such as the Antares laser (Los Alamos, USA) were attractive for a number of reasons, including their relatively low cost, high efficiency and high repetition rate of the pulses fired (see Ref.[8]). However, the long wavelength of these lasers meant that their energy deposition in the plasma was poor; collisional absorption scales with λ_0^{-2}, and, furthermore, unwanted LPI scales with $I\lambda_0^2$. Unwanted LPI may not only reduce the amount of light reaching the critical density (and therefore driving the ablation of surface material) by scattering, but it may also generate hot electrons. While a high target temperature (and therefore kinetic energy) is ultimately necessary for fusion, a hot target is substantially more difficult to compress than a cold one. Successful fusion therefore requires an element of timing, where compression is begun before the target temperature becomes too high. Hot electrons may propagate deep into the target before thermalising, raising the temperature and preventing the successful compression of the target (a process referred to as "pre-heating"). Together, these two effects, poor collisional absorption and hot electron generation, class CO_2 lasers as unsuitable for ICF (an excellent summary of studies performed with CO_2 lasers and their inherent difficulties is given in Ref.[8]). In experiments, the principle problematic LPI was deemed to be either backwards stimulated Raman scattering or Raman side scattering (defined later in the chapter), or a combination of the two[9].

Consequently, many current or planned ICF experiments use Nd:glass lasers with a fundamental wavelength of 1.057 μm. Experiments performed in the late 1970s and early 1980s using, for example, the Shiva laser system[10] showed persistently high levels of stimulated Raman scattering (in particular, in the plasma corona at a density of $n_c/4$) in addition to the reduced operating efficiency of the Nd:glass laser. As a result, laser light from Nd:glass lasers is often doubled or tripled in frequency to 527 or 351 nm. The NIF and LMJ both employ frequency-tripled Nd:glass laser systems.

Each pellet of fuel allows for a net gain in energy of approximately 100 MJ. A 1 GW fusion reactor would therefore require 10 pellets per second to be ignited, unachievable using current Nd:glass systems where the repetition rate is limited to a few shots per hour. The drawbacks of Nd:glass-based laser systems are sufficiently large that other sources of confinement are sought. Solid-state pumped-diode KrF lasers, such as the NIKE laser at the Naval Research Laboratory (NRL), have a higher repetition rate and shorter operating wavelength of 248 nm, thus reducing unwanted LPI, although the laser intensities so far achieved are much weaker than those of Nd:glass lasers (of the order of kJs rather than MJs). Heavy ion beams have also been considered as a method to efficiently heat the hohlraum. Another method, known as the Z-pinch, uses a high current dumped into an arrangement of wires to generate a magnetic field that inertially confines the plasma. Research in all of these areas is ongoing.

1.5 Parametric instability

In indirect-drive experiments, the expansion of the plasma generated by the heating of the hohlraum walls is undesirable. In order to slow the expansion of this high-Z plasma, a light gas mixture (typically helium and hydrogen) is injected into the hohlraum, with a density of up to $0.1n_c$. This mixture, in addition to the outer surface of the target, quickly becomes a plasma under laser irradiation, meaning that the laser beams must propagate ~ 3 mm through a low density plasma before even reaching the hohlraum walls. In both direct- and indirect-drive schemes, the expanding plasma corona surrounding the target is mostly below critical density. Plasma densities below n_c are typically referred to as "under-dense". As explained in the previous section, it is known from experiments that LPI in under-dense plasmas is a significant source of efficiency loss in ICF experiments. Near the entrance to the hohlraum and in the corona, the plasma density is also significantly inhomogeneous (visible in Fig. 1.2a). Typically, laser light in ICF experiments will pass through a plasma of increasing density as it propagates.

An electromagnetic wave with electric and magnetic field (E_0,B_0) travelling through a plasma of increasing density will become evanescent when the electron density n_e nears the critical value n_c. At this density, the electromagnetic wave frequency ω_0 is equal to the cold electron plasma frequency ω_{pe}, where ${\omega_{pe}}^2 = n_e e^2/\epsilon_0 m_e$, and the incident wave is reflected or absorbed. This resonance results in a "cut-off" in the frequencies that may propagate through the plasma, and is applicable to both electromagnetic and electrostatic waves.

The simplest and most important LPIs take the form of three-wave interactions: A transverse electromagnetic wave (the laser, often described as a"pump" wave, since it is the laser that drives the interactions) decays into two daughter waves. The three waves are nonlinearly coupled, where each of the two daughter waves is driven by the beating of the other daughter wave with the pump wave. The pump (ω_0, k_0) and two daughter waves $(\omega_{1,2}, k_{1,2})$ will exchange energy resonantly when their frequencies and wave vectors satisfy the following conditions, representing conservation of energy and momentum:

$$\omega_0 = \omega_1 + \omega_2, \qquad \vec{k_0} = \vec{k_1} + \vec{k_2}, \tag{1.2}$$

where we define without loss of generality $\omega_{0,1,2} > 0$ and $k_0 > 0$. This widely-studied parametric interaction is a mechanism of nonlinear mode conversion in plasmas, from electromagnetic to electrostatic and high-frequency to low-frequency waves.

We consider initially a plasma in which none of the waves are damped. In order for an interaction to take place, an arbitrarily small "seed" (the seed being either of the daughter waves) is necessary, typically provided by thermal fluctuations

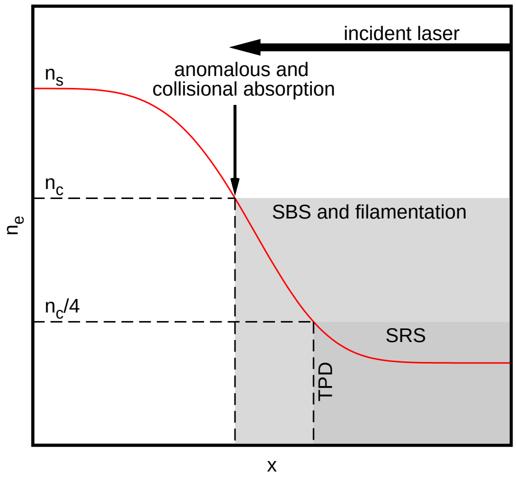

Figure 1.4: The regimes in which the various LPI take place.

in the plasma. The laser will then beat with the seed. The second daughter wave will be resonantly driven by the beating of the laser and the first daughter wave, causing it to grow. As a given daughter wave grows, its higher amplitude of oscillation increases the coupling of the other daughter wave to the laser, and *vice versa* in a positive feed-back loop. This process leads initially to the exponential growth of both parametrically excited daughter waves. Without depletion of the laser light or some other saturation mechanism, the daughter waves are said to be unstable, since their growth is unbounded. Parametric excitation may be defined as an amplification of an oscillation due to a periodic modulation of a parameter that characterises the oscillation. Accordingly, we call this exponential process a “parametric instability”. The various daughter waves that may be involved are discussed in the following section. The impact of damping on parametric instability is discussed in the next chapter.

1.5.1 Important three-wave interactions in ICF

Three-wave interactions of particular interest in ICF are listed below. The focus of this thesis is stimulated Raman scattering in ICF, so it is with this in mind that certain processes not relevant to stimulated Raman scattering are either briefly summarised or neglected. The general regime in which the discussed scattering processes are important is shown in Fig. 1.4.

Stimulated Raman scattering (SRS): An incident pump wave may scatter off a perturbation of the electron density of the plasma (a plasmon). The ions provide a neutralising charge background, but do not make a significant contribution to the dynamics of the wave. The resultant scattered electromagnetic wave beats with the pump wave, ponderomotively driving an electron plasma wave (EPW), otherwise known as a Langmuir wave (LW). For all three waves to be able to propagate, it is necessary that $\omega_{0,1,L} > \omega_{pe}$, where ω_L is the Langmuir wave frequency. From Eq. (1.2), this process may therefore occur only where $\omega_0 \geq 2\omega_{pe}$, or $n_e/n_c \leq 0.25$. The electromagnetic wave may be scattered in any direction, but the LW will grow fastest when the pump is scattered backwards and parallel to its initial direction.

Stimulated Brillouin scattering (SBS): An incident pump wave may scatter off of a perturbation of the ion density of the plasma (a phonon), resulting in an ion-acoustic wave (IAW). The ionic mass determines the inertia of the motion, while the pressure provides the restorative force. The electrons simply follow the motion of the ions. The dispersion relation of the long-wavelength IAW is only weakly dependent on the plasma density and therefore is not subject to the same frequency cut-off of the electron plasma frequency. Thus, SBS may effectively occur everywhere for which $\omega_0 \geq \omega_{pe}$.

Two-plasmon decay (TPD): An incident pump wave may decay into two plasmons (or LWs). Since $\omega_L \approx \omega_{pe}$, this process generally takes place when $\omega_0 \approx 2\omega_{pe}$. TPD is interesting as a source of diagnostics in ICF experiments due to the production of harmonics of the laser, scattered at predictable angles[11], arising when a decay plasmon is “added” to a photon of laser light, resulting in the $3\omega_0/2$ harmonic. It is also a source of hot electrons, leading to unwanted preheating of the plasma. The growth rate is maximised when the plasmons propagate at 45° to k_0 in the $k_0 - E_0$ plane.

Ion acoustic decay (IAD): An incident pump wave may decay into a plasmon and a phonon. Due to the comparatively high mass of the ions upon which the phonon frequency depends, the phonon frequency is small. Consequently, this process occurs near the critical density where $\omega_0 \sim \omega_{pe}$ and is regarded as an absorption mechanism, also acting as a source of hot electrons. IAD is often also referred to as plasmon-phonon decay (PPD), or simply as parametric decay.

Plasmon decay: Any plasmon may itself decay into a phonon and another plasmon, scattering in either the forwards or backwards direction. This process is responsible for the Langmuir decay instability (LDI), in which the primary Langmuir wave decays into another Langmuir wave and an ion acoustic wave. If driven strongly enough, the daughter Langmuir wave may also parametrically decay by the same process, resulting in a cascade until the last daughter Langmuir wave is below threshold for the LDI process. LDI acts therefore to saturate SRS.

1.5.1.1 Hot-spots and filamentation

In ICF experiments, the laser beam is processed a great deal before it reaches the target, through several stages of amplification, polarisation, frequency doubling or tripling, transportation and focusing. Consequently, the resultant beam does not have a smooth spatial profile, or spot, and has instead regions of higher and lower intensity. The high intensity regions in the beam are referred to as "hot-spots", which due to the raised laser intensity, are particularly susceptible to LPI. A wide array of techniques, such as random and kinoform phase plates (RPPs and KPPs), smoothing by spectral dispersion (SSD) in the longitudinal and transverse directions, and polarisation smoothing (PS), are used to smooth the beam profile or to shift the "speckle" pattern of laser intensity in space and time, thereby reducing, on average, the spatial and temporal correlation of LPI processes. The statistical properties of the smoothed beam profile are generally well-understood, and the intensity within the laser spot in typical NIF experiments varies between $\sim 5 \times 10^{14}$ and $\sim 1 \times 10^{16}$ W/cm^2, with an average power of 5×10^{15} W/cm^2. Hot-spots typically have a length of the order of 100 μm. In the future, a scheme by which the laser power may be switched on and off in rapid succession to form a series of pulses rather than a continuous beam [referred to as Spike Trains of Uneven Duration (STUD)] may provide a means to dramatically reducing LPI in ICF experiments[12].

SBS may drive zero-frequency density perturbations in the plane orthogonal to the wave vector of the laser beam. These growing ponderomotively-driven fluctuations, in addition to thermal and relativistic effects[13,14], may result in an optical turbulence that is capable of both steering the beam and causing the beam to undergo self-focusing, spoiling the precise pattern of laser light irradiation required for symmetric target compression. The growing ponderomotively-driven fluctuations, known as the "filamentation instability", have a growth rate that is typically small compared to SRS. However, the filamentation of the beam may result in the formation of hot-spots, and the behaviour of convective instabilities may become highly nonlinear[15].

1.5.2 Stimulated Raman scattering in experiments

As discussed earlier in the chapter, experiments conducted using a variety of laser systems have shown that SRS is of great concern in ICF experiments across a range of laser wavelengths. Classical models of SRS predict a Landau damping (discussed in the following chapter) of the Langmuir wave strong enough to prevent the amplification of thermal fluctuations to levels consistent with experimental observations. In experiments performed on the Nova laser at LLNL, the level of SRS reflectivity was found to reach high levels (up to 50% of the laser energy), while displaying a low sensitivity to the plasma conditions (i.e., the reflectivity varied weakly with $k_L\lambda_D$)[16], in stark contradiction with classical predictions. Recent experiments at the NIF have also shown similarly high levels of backwards SRS, in which SRS has been identified as the most deleterious of the laser-plasma interaction processes[17].

Through nonlinear wave-particle interaction (or "kinetic effects"), Landau damping may be reduced, thereby increasing the level of SRS in the plasma above classically predicted levels. However, if the damping of the waves driven by the laser were to be completely suppressed, this would lead to levels of reflectivity higher still than those observed in experiments. Therefore, it is generally accepted that two processes are at work: First, wave-particle interactions greatly reduce the effectiveness of Landau damping, leading to a rapid growth in the scattered light. Second, a nonlinear process (or processes) slows or even stops completely the growth of the scattered light. In addition, the scattered light often displays "bursty" behaviour, with strong, short-duration surges in the level of reflectivity. This second process has been a subject of intense study over the last 15 years, with many theories put forward. However, to date, no approach has offered a satisfactory and comprehensive explanation of the observed behaviour of the reflected light in experiments or indeed particle-in-cell simulations.

1.5.2.1 The kinetic frequency shift, inhomogeneity and autoresonance

The mechanism by which Landau damping is reduced by kinetic effects was described by O'Neil (1965)[5]. Through the same mechanism, growing kinetic effects in the plasma may herald the onset of a frequency shift in the driven Langmuir wave. This frequency shift, predicted and calculated by Morales and O'Neil (1972)[18] and Dewar (1972)[19], has been investigated as being the mechanism responsible for the saturation of the growth of the scattered light: Through a decrease in the frequency of the driven Langmuir wave, the resonance between the laser, scattered light and Langmuir wave may be lost, ending the process of positive feedback that provokes the rapid growth in scattered light. The magnitude of this frequency shift is then dependent on the local Langmuir wave amplitude.

As discussed previously, gradients in plasma density exist near the entrance to the hohlraum in indirect-drive ICF experiments, while strong gradients are inherent also to the expanding plasma corona that surrounds the irradiated target in both direct- and indirect-drive schemes. In the absence of kinetic effects, SRS was shown by Rosenbluth[20] (1972) to be saturated by a linear density gradient that acts to shift the wave numbers of the laser, scattered light and Langmuir wave as they propagate through the inhomogeneous plasma.

In this thesis, a mechanism for the enhancement of SRS is proposed, whereby the detuning from resonance caused by a density gradient in the plasma is counteracted by a frequency shift due to wave-particle interaction. During this process, the Langmuir self-adjusts its frequency via its amplitude so as to cancel exactly the wave number shift that would otherwise detune the resonance; this behaviour is described as “autoresonance”. Since the wave number shift increases with distance from the initial three-wave resonance point, a Langmuir wave propagating from this point will then grow rapidly in amplitude in order to remain phase-locked to the electromagnetic waves. It is shown in the coming chapters that autoresonance may provoke a growth in the daughter waves far above the level predicted by Rosenbluth in the absence of kinetic effects. The combination of density gradients and laser hot-spots may provide ideal conditions for growth of this nature. It is also shown that autoresonance may occur in a broad range of plasma conditions, and may be important in Raman amplifier designs.

Chapter 2

Three-wave coupling in stimulated Raman scattering

Stimulated Raman scattering (SRS) in warm plasmas is the parametrically unstable three-wave process describing the scattering of laser light from an electron density fluctuation, or Langmuir wave. As discussed in the previous chapter, it is of great interest in current inertial confinement experiments, where it provides a potent scattering mechanism of laser light that acts to reduce the efficiency of energy deposition at the precise spatial locations required for successful implosion and ignition. From a purely academic perspective, SRS presents a canonical example of three-wave coupling, and presents a rich range of interesting problems.

At its simplest, SRS is the inelastic scattering of a photon, named after its discoverer Sir Chandrasekhara Venkata Raman, who observed inelastic photon scattering in liquids in 1928[21] (The independent work of Landsberg and Mandelstam also identified inelastic photon scattering in crystals in the same year[22]. The Nobel Prize was awarded to Raman, however.). In 1965, Dubois and Goldman[23] discussed the possibility of the existence of radiation-induced plasma oscillations that could grow sufficiently quickly so as to overcome dissipation rates and become parametrically unstable.

The importance in ICF experiments of various parametric instabilities, including SRS, was identified in the 1960s by numerous authors. A great deal of work was done in the 1960s and 1970s investigating the behaviour of parametric instabilities, particularly the mechanisms by which the growth of the daughter waves could be slowed or saturated. One such mechanism is inhomogeneity in the electron density of the plasma: In SRS, the three-wave resonance required for efficient coupling of the waves to each other may be detuned by the inhomogeneity. This detuning arises because the three waves, in particular the Langmuir wave, are subject as they propagate to dispersion relations that vary with the local value of the electron plasma frequency, itself a function of the local density.

In 1972, Rosenbluth[20] calculated the impact of this detuning, most notably calculating the amplitudes at which the daughter waves saturate in a linear density profile. A string of subsequent publications (e.g. those of Liu, Rosenbluth and White[24,25]; and DuBois, Forslund and Williams[26]) expanded upon this work, and are relevant to modern day ICF experiments where the growth rates and saturation levels of instabilities (diagnosed primarily through measured plasma reflectivities) are of central importance.

A plasma may support a variety of matter waves (i.e. propagating perturbations of the electron or ion densities). The constituent particles of the medium through which the wave travels may themselves interact with this wave. The resultant wave-particle interaction phenomena are broadly referred to as “kinetic effects”, and are of great importance in modern ICF experiments. The most well-known of these effects is “Landau damping”, describing the energy exchange of the wave with particles in the plasma which have velocities near the phase velocity of the wave. In plasmas with temperatures relevant to ICF (the velocity distribution of the particles is initially determined by the temperature of the plasma), the particles drain energy from the wave, in effect damping the wave and slowing its growth or even preventing parametric instability entirely. This effect, although experimentally observed earlier, was studied analytically by Zakharov and Karpman in 1963[27] and by O’Neil in 1965[5]. A great number of kinetic simulations, designed to describe the physical processes responsible for Landau damping and other kinetic effects, have been performed since the work of Forslund *et al.* (simulation results are given in Ref.[28] and the accompanying theory in Ref.[29]) in which electron trapping and wave breaking (both defined later in the chapter) were observed. Advances in the modelling of kinetic effects are ongoing to this day.

In this chapter, the equations governing the propagation of electromagnetic and electrostatic waves relevant to SRS are derived (the methods employed are however applicable to a broad range of parametric instabilities), as well as the growth rates of the daughter waves. The three principle equations of SRS, describing the propagation of incident laser light, scattered light and a driven electron-plasma wave (the Langmuir wave), form the backbone around which a range of nonlinear phenomena are introduced and explored in this thesis. Perturbations to these equations are subsequently introduced in the form of terms incorporating the inhomogeneity of the plasma and the effects of wave-particle interactions. With the introduction of these terms, the possibility of autoresonance in the plasma is discussed, paving the way for further investigation in the following chapters.

2.1 Derivation of the three-wave equations

We derive here the three coupled envelope equations that describe the interaction of the pump, scattered and Langmuir waves in SRS. For simplicity, the following derivation assumes that the transverse electromagnetic (EM) waves are linearly polarised. The result however is equally applicable to circular polarisations. The electrostatic (ES) Langmuir wave is longitudinal.

We take as the point of departure Maxwell's equations, satisfied by waves with electric field $\vec{E} = (E_x, E_y, E_z)$ and magnetic field $\vec{B} = (B_x, B_y, B_z)$:

$$\nabla \cdot \vec{E} = \epsilon_0^{-1}\rho, \tag{2.1}$$

$$\nabla \cdot \vec{B} = 0, \tag{2.2}$$

$$\nabla \wedge \vec{E} = -\partial_t \vec{B}, \tag{2.3}$$

$$\nabla \wedge \vec{B} = \mu_0 \vec{J} + c^{-2}\partial_t \vec{E}, \tag{2.4}$$

where $\vec{J}$ is the charged particle current. The general solution to Eqs. (2.2) and (2.3) may be expressed in terms of the vector potential $\vec{A} = (A_x, A_y, A_z)$ and the scalar potential ϕ:

$$\vec{E} = -\nabla\phi - \partial_t \vec{A}, \tag{2.5}$$

$$\vec{B} = \nabla \wedge \vec{A}, \tag{2.6}$$

We work in the Coulomb gauge ($\nabla \cdot \vec{A} = 0$). The light waves are thus purely inductive (given by $\vec{A}$) while the Langmuir wave is electrostatic (given by ϕ). In the absence of a perturbation, the electron charge of the plasma is neutralised by the ions. Since the ion mass is so much greater than the electron mass, the ions are effectively stationary over the relevant timescales, thus we only consider here perturbations of the electron density. Taking the divergence of Eq. (2.5), we obtain Poisson's equation,

$$\nabla^2\phi = -\epsilon_0^{-1}\rho = \frac{e}{\epsilon_0}\delta n_e, \tag{2.7}$$

where δn_e is a perturbation of the background electron density n_e, such that the total density is given by $N_e = n_e + \delta n_e$.

2.1.0.2 The transverse electromagnetic waves

Inserting the potential expressions given by Eqs. (2.5) and (2.6) into Ampere's law Eq. (2.4), we find

$$\nabla \wedge \nabla \wedge \vec{A} = \mu_0 \vec{J} - c^{-2}\partial_t \nabla\phi - c^{-2}\partial_{tt}\vec{A}. \tag{2.8}$$

In the Coulomb gauge, we have the vector identity $\nabla \wedge \nabla \wedge \vec{A} = \nabla(\nabla \cdot \vec{A}) - \nabla^2 \vec{A} = -\nabla^2 \vec{A}$. We substitute this relation into Eq. (2.8) and rearrange to give

$$\partial_{tt}\vec{A} - c^2 \nabla^2 \vec{A} = \epsilon_0^{-1} \vec{J} - \partial_t \nabla \phi. \tag{2.9}$$

We choose $\vec{A} = A_y(x,t)\hat{y}$, giving

$$\partial_{tt} A_y - c^2 \partial_{xx} A_y = \epsilon_0^{-1} j_y, \tag{2.10}$$

where j_y is the transverse current induced in the plasma by the EM field. An expression for the transverse current is obtained by considering the motion of charged particles in the plasma due to the Lorentz force,

$$m \frac{d\vec{v_e}}{dt} = q(\vec{E} + \vec{v_e} \wedge \vec{B}), \tag{2.11}$$

where $\vec{v_e} = (v_x, v_y, v_z)$ is the electron velocity. Taking the longitudinal components and inserting Eqs. (2.5) and (2.6), we find

$$m \frac{dv_y}{dt} = -e(E_y - v_x B_z) = e(\partial_t A_y + v_x \partial_x A_y) = \frac{dA_y}{dt}, \tag{2.12}$$

giving the conservation of transverse canonical momentum $p_y = mv_y - eA_y$ (this simply arises from translational symmetry in the transverse direction). Assuming an initially stationary distribution of particles, it follows that

$$v_y = eA_y/m, \tag{2.13}$$

giving a transverse electron current of the following form:

$$j_y = -N_e e v_y = -\frac{N_e e^2}{m_e} A_y. \tag{2.14}$$

We see here that the contribution of the ions to the current is smaller by a factor of the ratio of the ion mass to the electron mass. Inserting Eq. (2.14) into Eq. (2.10) and writing $N_e = n_e + \delta n_e$, we find:

$$\partial_{tt} A_y - c^2 \partial_{xx} A_y + \omega_{pe}^2 A_y = -\omega_{pe}^2 \frac{\delta n_e}{n_e} A_y. \tag{2.15}$$

The LHS of this equation is satisfied by the familiar complex travelling wave solution $A_y(x,t) = A_{y0} \exp[i(kx - \omega t)]$, with dispersion relation $\omega^2 = \omega_{pe}^2 + c^2 k^2$. The RHS of the equation shows the coupling between density fluctuations (Langmuir waves) and EM waves, and will be developed later in this section.

2.1.0.3 The longitudinal Langmuir wave

We adopt a warm fluid model for the plasma. The high-frequency nature of Langmuir waves allows for the ions to be treated as a fixed, neutralising background. We begin by writing the continuity and conservation of momentum equations for the electrons, respectively, as

$$\partial_t N_e + \nabla \cdot (N_e \vec{v_e}) = 0, \tag{2.16}$$

$$m_e N_e \left[\partial_t \vec{v_e} + (\vec{v_e} \cdot \nabla)\vec{v_e}\right] = -eN_e(\vec{E} + \vec{v_e} \wedge \vec{B}) - \nabla p_e. \tag{2.17}$$

For the electron pressure p_e, we have from the closure of the equation of state

$$\frac{p_e}{N^\gamma} = \text{const.} \tag{2.18}$$

For Langmuir waves, the phase velocity $v_\phi = \omega_L/k_L$ is such that $|v_\phi| \gg v_{th}$. We thus consider the adiabatic equation of state, where $\gamma = (D+2)/D)$, where D is the number of degrees of freedom. For the 1-D wave propagation assumed here, $D = 1$, giving $\gamma = 3$.

It is useful to separate the velocity $\vec{v_e}$ into linear $\vec{v_e}^l$ and nonlinear $\vec{v_e}^{nl}$ parts, such that $\vec{v_e} = \vec{v_e}^l + \vec{v_e}^{nl}$. The electric $\vec{E}$ field may be decomposed into the applied field arising from the electromagnetic waves $\vec{E}^{EM}$ and a residual field $\vec{E}^r$, where $\vec{E} - \vec{E}^{EM} = \vec{E}^r$. We assume that the only significant magnetic field is that which is applied externally, $\vec{B}^{EM}$, thus $\vec{B} = \vec{B}^{EM}$ (i.e. magnetic fields generated by the electron motion are negligible). In the absence of the electron pressure, the response of the electrons to the applied transverse electric field is simply given by

$$m_e \partial_t \vec{v_e}^l = -e\vec{E}^{EM}, \tag{2.19}$$

and consequently, taking the vector curl of this expression,

$$m_e \partial_t \nabla \wedge \vec{v_e}^l = e\partial_t \vec{B}. \tag{2.20}$$

Since $\vec{v_e}^l = 0$ in the absence of this field, we may write

$$m_e \nabla \wedge \vec{v_e}^l = e\vec{B}. \tag{2.21}$$

We may now subtract the linear response of the electrons to the applied electric field from Eq. 2.17 and insert Eq. 2.21 to give

$$m_e N_e[\partial_t \vec{v_e}^{nl} + (\vec{v_e} \cdot \nabla)\vec{v_e}^{nl}] = -N_e[e\vec{E}^r + m_e \vec{v_e}^l \wedge (\nabla \wedge \vec{v_e}^l) + m_e(\vec{v_e} \cdot \nabla)\vec{v_e}^l] - \partial_x p_e. \tag{2.22}$$

The terms $(\vec{v_e}^{nl} \cdot \nabla)\vec{v_e}^l$ and $(\vec{v_e}^l \cdot \nabla)\vec{v_e}^{nl}$ are dropped due to being of higher order. Using a well-known vector calculus expression, we find

$$m_e \left[\vec{v_e}^l \wedge (\nabla \wedge \vec{v_e}^l) + (\vec{v_e}^l \cdot \nabla)\vec{v_e}^l\right] \equiv \frac{1}{2} m_e \nabla (\vec{v_e}^l)^2. \tag{2.23}$$

This expression gives the nonlinear force acting on the electrons due to the electromagnetic waves and, in the case of transverse translational symmetry, acts only along the x-axis. The residual field $\vec{E}^r$ (primarily a response to the electron pressure) and nonlinear velocity $\vec{v_e}^{nl}$, then share this same axis. Taking the longitudinal components of Eq. 2.22, we find the following:

$$m_e N_e(\partial_t v_x + v_x \partial_x v_x) = -N_e e E_x - \frac{1}{2} m_e N_e \partial_x v_y^2 - \partial_x p_e. \tag{2.24}$$

The electric field component E_x is then the longitudinal field of the Langmuir wave. This electrostatic wave satisfies Poisson's equation, such that

$$\partial_x E_x = -\frac{e\delta n_e}{\epsilon_0}. \tag{2.25}$$

For the term containing v_y, we have using Eq. 2.13 the following:

$$-\frac{1}{2} m_e \partial_x v_y^2 = -\frac{1}{2}\partial_x \frac{e^2 A_y^2}{m_e}. \tag{2.26}$$

This nonlinear force acts to couple the Langmuir wave to the EM waves and is responsible for driving the longitudinal density perturbation of the plasma. In this approximation, the total nonlinear force is given by the sum of the advective term and the electromagnetic coupling force. This force P is frequently referred to as the "ponderomotive force", as is given by the following equation:

$$P = -m_e v_x \partial_x v_x - \frac{1}{2}\partial_x \frac{e^2 A_y^2}{m_e}. \tag{2.27}$$

The nonlinear advective term $v_x \partial_x v_x$ does not couple the electromagnetic waves to the Langmuir wave; rather, it couples different harmonics of the Langmuir wave. While it is not essential in deriving the three-wave coupled envelope equations (and is consequently neglected for the time being), it may play a significant role as the Langmuir wave grows in amplitude. The implications of the advective term are discussed later in the chapter.

We linearise all remaining terms in the following way:

$$\partial_t \delta n_e + n_e \partial_x v_x = 0, \tag{2.28}$$

$$m_e \partial_t v_x = -eE_x - \frac{1}{2}\partial_x \frac{e^2 A_y^2}{m} - \frac{\partial_x \delta p_e}{n_e}, \tag{2.29}$$

$$\delta p_e = \gamma \frac{p_0}{n_e}\delta n_e = 3T_e \delta n_e, \tag{2.30}$$

where the ideal gas law $p_e = n_e T_e$ has been used in Eq. (2.30). We now insert Eq. (2.25) into Eqs. (2.28) and (2.30) to obtain the following:

$$v_x = \frac{\epsilon_0}{e n_e} \partial_t E_x, \tag{2.31}$$

$$\delta p = -3 \frac{\epsilon_0 T_e}{e} \partial_x E_x. \tag{2.32}$$

These may in turn be used to eliminate the pressure and velocity terms from Eq. (2.29), giving

$$\partial_{tt} E_x - 3 v_{th}^2 \partial_{xx} E_x + \omega_{pe}^2 E_x = -\frac{1}{2} \omega_{pe}^2 \partial_x \frac{e A_y^2}{m}. \tag{2.33}$$

In the absence of the electromagnetic waves (i.e. a freely-propagating wave), the LHS of Eq. (2.33) is satisfied by a longitudinal travelling wave of the form $E_x(x,t) = E_{x0} \exp[i(kx - \omega t)]$, giving the well-known Bohm-Gross dispersion relation $\omega^2 = \omega_{pe}^2 + 3 v_{th}^2 k^2$.

2.1.1 Envelope equations

In the previous subsections, we derived equations governing the propagation and nonlinear driving of the EM and ES waves. Using Eq. (2.25), we rewrite Eqs. (2.15) and (2.33) to give

$$\partial_{tt} A_y - c^2 \partial_{xx} A_y + \omega_{pe}^2 A_y = \frac{e}{m} A_y \partial_x E_x, \tag{2.34}$$

$$\partial_{tt} E_x - 3 v_{th}^2 \partial_{xx} E_x + \omega_{pe}^2 E_x = -\frac{1}{2} \omega_{pe}^2 \partial_x \frac{e A_y^2}{m}. \tag{2.35}$$

As discussed earlier this chapter, energy will only efficiently be transferred between the modes when the three waves are in resonance. Components of the waves that are far from resonance contribute little to the behaviour of the system, since their effect will quickly average to zero after integration over a few complete cycles of the wave. It is therefore convenient and useful to move to an *envelope formulation* of the waves, and consider only small perturbations in frequency (or wave number) from the resonant values. We label the forward-propagating and backward-propagating EM wave envelope amplitudes A_0 and A_1, respectively, and the Langmuir wave envelope amplitude E_L.

For the EM waves, we write the vector potential A_z as the sum of the counter-propagating terms in the following way:

$$A_z = \frac{1}{2} \left[A_0(x,t) e^{i(k_0 x - \omega_0 t)} + c.c. \right] + \frac{1}{2} \left[A_1(x,t) e^{i(k_1 x - \omega_1 t)} + c.c. \right], \tag{2.36}$$

and for the Langmuir wave:

$$E_x = \frac{1}{2}\left[E_L(x,t)e^{i(k_L x - \omega_L t)} + c.c.\right]. \tag{2.37}$$

The linear dispersion relation for each of the three waves is now easily obtained by neglecting the RHS wave coupling terms in Eqs. (2.34) and (2.35) and inserting the Eqs. (2.36) and (2.37). After differentiation, we find for the frequencies $\omega_{0,1,L}$ and wave numbers $k_{0,1,L}$ the following linear dispersion relations:

$$\omega_0^2 = \omega_{pe}^2 + c^2 k_0^2, \tag{2.38}$$

$$\omega_1^2 = \omega_{pe}^2 + c^2 k_1^2, \tag{2.39}$$

$$\omega_L^2 = \omega_{pe}^2 + 3v_{th}^2 k_L^2. \tag{2.40}$$

These dispersion relations are plotted in Fig. 2.1 for both forward SRS (FSRS) and backward SRS (BSRS), where $k_1 > 0, k_L > 0$ and $k_1 < 0, k_L > 0$, respectively. The dispersion relations may be solved for given values of T_e (where $v_{th}^2 = k_B T_e/m_e$, for which k_B is Boltzmann's constant) and $\omega_{pe}^2/\omega_0^2 = n_e/n_c$ in order to determine $\omega_{1,L}$ (and $k_{0,1,L}$) relative to ω_0 (and $c\omega_0$). For k_0, we have simply

$$k_0 = c^{-1}\sqrt{(\omega_0^2 - \omega_{pe}^2)}. \tag{2.41}$$

For $\omega_{1,L} > 0$, solving simultaneously Eqs. (2.39-2.40) produces two solutions, one corresponding to BSRS and the other to FSRS. It is not possible to succinctly write down an exact analytic solution, but straight-forward solutions may be approximated when $v_\phi \gg v_{th}$. In this regime,

$$\omega_L \simeq \omega_{pe} \quad \Rightarrow \quad \omega_1 \sim \omega_0 - \omega_{pe}, \tag{2.42}$$

and then

$$k_1 \simeq \pm c^{-1}\sqrt{(\omega_0 - \omega_{pe})^2 - \omega_{pe}^2} \tag{2.43}$$

$$\simeq \pm c^{-1}\sqrt{\omega_0^2 - 2\omega_0\omega_{pe}}, \tag{2.44}$$

and thus, using $k_0 = k_1 + k_L$,

$$k_L \simeq k_0 \mp c^{-1}\sqrt{\omega_0^2 - 2\omega_0\omega_{pe}}, \quad \omega_L = \sqrt{\omega_{pe}^2 + 3v_{th}^2 k_L^2}. \tag{2.45}$$

The values used for the wave numbers and frequencies in the coming chapters, however, are calculated by solving the dispersion relation equations numerically and are exact to an arbitrary precision.

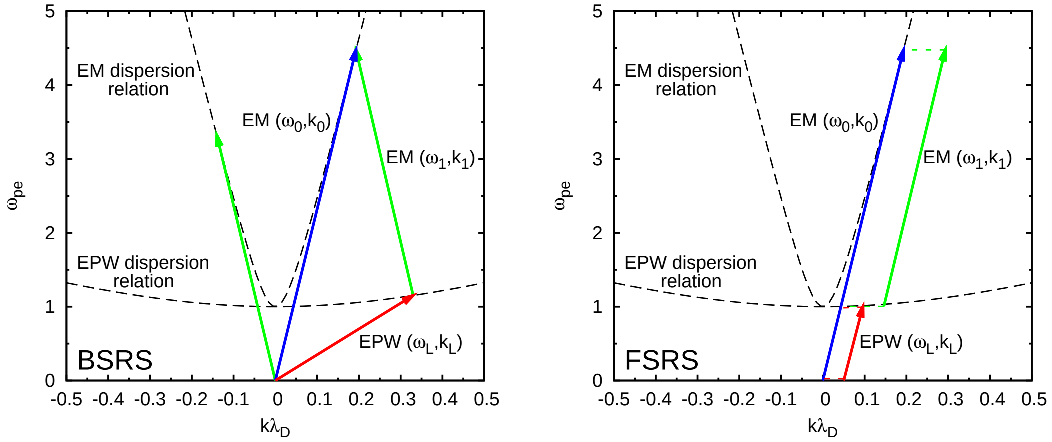

Figure 2.1: Dispersion relations for the electromagnetic and Langmuir waves for both BSRS and FSRS.

We require the envelopes to vary slowly with respect to the phase of the waves, such that $|A_0|^{-1}\partial_x|A_0| \ll |k_0|$, $|A_0|^{-1}\partial_t|A_0| \ll |\omega_0|$, and likewise for A_1 and E_L. Differentiating Eq. (2.36) and using the dispersion relation Eqs. (2.38) and (2.39) to eliminate terms, we find:

$$\begin{aligned}
&\frac{1}{2}\left[(\partial_{tt}A_0 - 2i\omega_0\partial_t A_0)e^{i(k_0x-\omega_0 t)} + \text{c.c.}\right] - \frac{1}{2}c^2\left[(\partial_{xx}A_0 + 2ik_0\partial_x A_0)e^{i(k_0x-\omega_0 t)} + \text{c.c.}\right]\\
&+\frac{1}{2}\left[(\partial_{tt}A_1 - 2i\omega_1\partial_t A_1)e^{i(k_1x-\omega_1 t)} + \text{c.c.}\right] - \frac{1}{2}c^2\left[(\partial_{xx}A_1 + 2ik_1\partial_x A_1)e^{i(k_1x-\omega_1 t)} + \text{c.c.}\right]\\
&= \frac{1}{4}\frac{e}{m_e}\left[(\partial_x E_L + ik_L E_L)e^{i(k_Lx-\omega_L t)} + \text{c.c.}\right] \times \left\{\left[A_0 e^{i(k_0x-\omega_0 t)} + \text{c.c.}\right] + \left[A_1 e^{i(k_1x-\omega_1 t)} + \text{c.c.}\right]\right\},
\end{aligned} \tag{2.46}$$

and similarly for the Langmuir wave. We multiply Eq. (2.46) by $\exp[-i(k_0x-\omega_0t)]$ (or $\exp[-i(k_1x-\omega_1t)]$) and average over the fast phase variation. The matching conditions for resonant backscatter naturally emerge from this approach. The result is an equation describing the envelope A_0 (or A_1). Assuming a slowly varying envelope such that $|\partial_{tt}A_0| \ll |\omega_0\partial_t A_0|$ (and likewise for A_1, E_L), we neglect the second order derivatives in time and space, giving:

$$-2i\omega_0\partial_t A_0 - 2ic^2k_0\partial_x A_0 = i\frac{e}{2m}k_0E_LA_1e^{-i[(k_0-k_1-k_L)x-(\omega_0-\omega_1-\omega_L)t]}, \tag{2.47}$$

Rearranging this equation and repeating the same process for the scattered and

Langmuir waves, we finally arrive at the coupled three-wave equations:

$$\mathcal{L}_0 A_0 = -\frac{e}{4m_e}\frac{k_L}{\omega_0}E_L A_1 e^{-i\Psi}, \tag{2.48}$$

$$\mathcal{L}_1 A_1 = \frac{e}{4m_e}\frac{k_L}{\omega_1}E_L^* A_0 e^{i\Psi}, \tag{2.49}$$

$$\mathcal{L}_L E_L = \frac{e}{4m_e}\frac{k_L}{\omega_L}\omega_{pe}^2 A_1^* A_0 e^{i\Psi}, \tag{2.50}$$

where

$$\mathcal{L}_{0,1,L} = \partial_t + c_{0,1,L}\partial_x, \tag{2.51}$$

are the linear propagation operators, for which the group velocities $c_{0,1,L} = \partial\omega_{0,1,L}/\partial k_{0,1,L}$. The phase mismatch $\Psi = (k_0 - k_1 - k_L)x - (\omega_0 - \omega_1 - \omega_L)t$ is discussed in the following sections.

2.2 Resonant growth rates

We consider now how the three coupled equations will evolve in a plasma that is effectively infinite in extent. The growth rates discussed here are derived in Ref.[30]. The pump wave is typically of high intensity compared to the daughter waves, thus we assume here that it is not significantly depleted by the initial growth of the daughter waves. The three waves will only efficiently exchange energy when they are resonant or nearly resonant, i.e. when the $\Psi \sim 0$. We begin by considering a simplified case where the propagation of the waves is unimportant to their growth, and allow a small frequency mismatch of the form

$$\delta\omega = \omega_0 - \omega_1 - \omega_L. \tag{2.52}$$

We then write down the reduced two-wave coupling equations as the following:

$$\partial_t A_1 = \frac{e}{4m_e}\frac{k_L}{\omega_1}E_L^* A_0 e^{-i\delta\omega t}, \tag{2.53}$$

$$\partial_t E_L = \frac{e}{4m_e}\frac{k_L}{\omega_L}\omega_{pe}^2 A_1^* A_0 e^{-i\delta\omega t}, \tag{2.54}$$

where the pump amplitude A_0 is fixed. Using the substitution $E_L = \tilde{E}_L \exp(-i\delta\omega t)$ and differentiating, we find

$$\partial_{tt}\tilde{E}_L - i\delta\omega\partial_t\tilde{E}_L - \gamma_0^2\tilde{E}_L = 0, \tag{2.55}$$

where

$$\gamma_0 = \frac{1}{4}k_L\frac{\omega_{pe}}{\sqrt{\omega_L\omega_1}}\left(\frac{eA_0}{m_e}\right). \tag{2.56}$$

We find therefore the solution

$$E_L, A_1 \sim \exp\left[\left(\sqrt{\gamma_0^2 - \frac{\delta\omega^2}{4}} - i\frac{\delta\omega}{2}\right)t\right], \tag{2.57}$$

for which growth requires

$$\frac{|\delta\omega|}{2} < \gamma_0. \tag{2.58}$$

This inequality defines an effective bandwidth for the resonance and is an important quantity when considering nonlinear effects later in the chapter.

The growth defined by $E_L, A_1 \sim \exp(\gamma_0 t)$ is purely temporal, and in the case of fixed pump amplitude, is also unbounded at every point in the plasma. We refer to growth of this nature as "absolute", for which $E_L, A_1(x, t \to \infty) \to \infty$.

From Eq. 2.56, we see that the resonant maximum growth rate is proportional to k_L. From Fig. 2.1, we see that for given ω_0, k_0, the growth rate for BSRS is consequently greater than that of FSRS. This is the case unless other processes interfere, such as damping of the Langmuir wave; linear Landau damping, described later in the chapter, increases with the parameter $k_L\lambda_D$, thus FSRS may become competitive with BSRS in certain regimes.

If we now allow the waves to propagate, the growth at every point in the plasma remains absolute, but is reduced provided the two daughter waves are counter-propagating (for copropagating waves, no absolute instability is possible). We assume a backward-propagating seed of initially small and localised amplitude in the form of a delta function at some point x_s. In this case, the growth rate at all points in the plasma is given by

$$\gamma_{abs} = 2\gamma_0 \frac{|c_L c_1|^{1/2}}{|c_L| + |c_1|}. \tag{2.59}$$

At $t = 0$, this initial seed is the point at which the amplitude of A_1 is a maximum. We label this maximum in the amplitude of A_1 as A_1^{max}. Although all points will experience absolute growth, A_1^{max} will propagate at the convective growth velocity $c_{conv} = (c_L + c_1)/2$. We define the point x^{max} such that $A_1(x^{max}) = A_1^{max}$, and $x_{max} = x_s + c_{conv}t$. The propagating maximum grows according to the convective growth rate γ_{conv}, where $\gamma_{conv} = \gamma_0$. This propagating maximum therefore grows faster compared to any fixed point in the plasma.

We may introduce damping to the wave equations. The light waves are damped primarily via collisional inverse-bremsstrahlung, while the Langmuir wave is primarily damped as a result of kinetic effects, discussed later in this chapter. We assign a damping rate ν_L' to the Langmuir wave and ν_1' to the backscattered wave, formally included in the envelope equations by modifying the momenta equations. A similar approach to deriving Eq. 2.57 yields, in the limit $\nu'_{0,1,L} \ll \omega_{0,1,L}$,

$$\gamma^{\nu}_{conv} = \sqrt{\gamma_0^2 + \frac{(\nu'_L - \nu'_1)^2}{4}} - \frac{(\nu'_L + \nu'_1)}{2}. \tag{2.60}$$

The threshold for convective growth is then simply

$$\gamma_0 > \gamma^{min}_{conv} \equiv \sqrt{\nu'_L \nu'_0}, \tag{2.61}$$

for which it should be noted that convective growth is always possible if one of the two daughter waves is undamped. For growth of an *absolute* nature, it is necessary that the stricter condition

$$\gamma_0 > \gamma^{min}_{abs} \equiv \frac{|c_L c_1|^{1/2}}{2} \left(\frac{\nu'_L}{|c_L|} + \frac{\nu'_1}{|c_1|} \right), \tag{2.62}$$

be satisfied. This damping results in a reduced absolute growth rate γ^{ν}_{abs}, such that

$$\gamma^{\nu}_{abs} = \gamma_{abs} \left(1 - \frac{\gamma^{min}_{abs}}{\gamma_0} \right). \tag{2.63}$$

For given plasma conditions and daughter wave damping rates, the conditions for SRS growth (convective or absolute) may be trivially rearranged to give a threshold in laser intensity. In all studies conducted later in this thesis, the laser intensity is well above threshold.

2.2.1 The spatial growth rate

Finally, in addition to the *temporal* growth rates, the *spatial* (convective) growth rate will also be a useful quantity to consider in autoresonance later in this thesis. The steady-state convective growth rate is easily obtained by assuming a fixed pump wave and neglecting the temporal derivatives in Eqs. (2.49) and (2.50), giving the following reduced set of equations:

$$c_1 \partial_x A_1 = \frac{e}{4m_e} \frac{k_L}{\omega_1} E_L^* A_0 e^{-i\delta\omega t}, \tag{2.64}$$

$$c_L \partial_x E_L = \frac{e}{4m_e} \frac{k_L}{\omega_L} \omega_{pe}^2 A_1^* A_0 e^{-i\delta\omega t}. \tag{2.65}$$

Substituting Eq. (2.65) into Eq. (2.64), we find the following spatial growth rate:

$$K_{max} = \frac{\gamma_0}{|c_L c_1|^{1/2}}. \tag{2.66}$$

In the presence of damping ($\gamma_{min}^{conv} < \gamma_0 < \gamma_{min}^{abs}$), this spatial growth rate is reduced to

$$K = \frac{\gamma_0^2 - {\gamma_{conv}^{min}}^2}{|c_L c_1 \max(\nu_L'/c_L, \nu_1'/c_1)|}. \tag{2.67}$$

It should be noted that the summary here misses a great deal of detail with regards to the subtleties of parametric instability. Indeed, for $c_L c_1 < 0$ (as is the case for BSRS), the simple treatment here provides a spatial gain that is imaginary: no growth is possible! One must perform careful contour integrals of the coupled mode equations in the Fourier-Laplace domain and pay attention to the branches of solutions found in order to retrieve the correct result. Such a treatment is given in Ref.[31].

2.3 Effect of finite plasma length

The discussion of growth rates and the notions of convective and absolute instability have up to this point been in the context of a plasma that is of infinite extent. The notion of instability in a finite plasma is similar, but differs in that there is no longer a truly convective instability, since A_1^{max} must eventually propagate out of the region in which the plasma exists (assuming that the group velocities, hence also the convective velocity, are constant). This does not mean that spatial growth is unimportant, since the convective growth may still have a significant impact on the evolution of the system (for example, it may still be able to amplify thermal fluctuations to an important, but not infinite, amplitude).

The analogue of absolute instability in an infinite plasma is then an instability in a finite plasma for which a perturbation at any point (or a number of points) may undergo growth to an unbounded amplitude. For a plasma of length L, we define a critical length L_{crit}. In the limit $\gamma_0 \gg \gamma_{abs}^{min}$, this critical length tends irrespective of damping towards to L_c:

$$L_{crit} \to L_c \equiv \frac{\pi}{2} \left(\frac{\gamma_0}{|c_L c_1|^{1/2}} \right)^{-1}, \tag{2.68}$$

and provided $L \gg L_{crit}$, the maximum growth rate tends towards γ_{abs}^{ν}. For $L > L_{crit}$, absolute growth is possible, and for $L \gg L_{crit}$, the growth is indistinguishable from an infinite plasma but for near the edges. The characteristic length over which the growth is unchanged from an infinite plasma is given simply by

$$L_{cha} = \frac{|c_L c_1|^{1/2}}{\gamma_0}, \tag{2.69}$$

In contrast, in the limit that $\gamma_0 \to \gamma_{abs}^{min}$, $L_{crit} \to \infty$.

For convective growth, in the regime $\gamma_0 > \gamma_{abs}^{min}$, $c_1 c_L > 0$ it is necessary that $L > L_{cha}$. For convective growth where $\gamma_{abs}^{min} > \gamma_0 > \gamma_{conv}^{min}$, the length L_{cha} is increased compared to that of absolute growth:

$$L_{conv} = \frac{|c_1 c_L| \max(\nu_L'/|c_L|, \nu_1'/|c_1|)}{\gamma_0^2 - \nu_L' \nu_1'}. \tag{2.70}$$

Under the conditions typically used in this thesis, $L \gg L_{crit}$, and the plasma may be thought of as infinite with respect to the nature of the instabilities present. It should again be noted that the situation is often more complex e.g. a reflection at a boundary may allow a convective instability in a finite plasma to behave in an absolute fashion as it bounces back and forth between boundaries.

2.4 Detuning mechanisms

In the previous section, the equations describing the resonant interaction between the pump and daughter waves were derived. These equations provide the backbone necessary to describe a wide variety of nonlinear processes that may alter SRS. Eqs. (2.48-2.50) describe the process by which laser light drives the growth of backscattered light and a Langmuir wave. As the daughter waves grow, energy will be drained from the laser. Thus, while the growth of the daughter waves is initially exponential, their growth is quickly saturated by the total depletion of the pump. In reality, this is seldom the case: nonlinear processes or physical considerations typically act to saturate the growth of the daughter waves through detuning the resonance or damping the daughter waves. However, in ICF experiments, the level at which the daughter waves are saturated is still considerable and is highly problematic.

We wish to model processes responsible for altering the growth rate and evolution of SRS. A range of important processes are covered in the following subsections.

2.4.1 Inhomogeneity

A wave propagating through an inhomogeneous medium will undergo a shift in wave number. We take as a point of reference an assumed resonance in the plasma. At this density, the matching conditions for resonance are satisfied. However, as the waves propagate away from this point, this matching will be lost, ending the process of positive feedback described earlier in the chapter that is necessary for parametric instability. From continuity, we assume a free wave propagating through an inhomogeneous medium will have a constant frequency. From the dispersion relations given in Eqs. (2.38-2.40), it is clear that the local value of the wave numbers are thus dependent on the local value of the plasma frequency. This effect is crucial to the mechanism of autoresonance, and thus features heavily in this thesis. In the following chapter, the wave number shift due to inhomogeneity is considered in both linear and parabolic profiles. We derive here therefore the behaviour of the wave number shift in both of these cases.

At the resonance point in the linear case, $\omega_0 - \omega_1 - \omega_L = \delta\omega = 0$. Each of the waves has phase $\psi_{0,1,L}(x,t) = \int_{x_{res}}^{x} dx' k_{0,1,L}(x') - \omega_{0,1,L} t$, such that $\Psi = \Psi(x) = \psi_0 - \psi_1 - \psi_L = \int_{x_{res}}^{x} dx' \Delta k(x')$, where $\Delta k(x') \equiv k_0(x') - k_1(x') - k_L(x')$ and x_{res} is the three-wave resonance point. For both clarity and simplicity of integration, it is convenient to make the substitution $E_L = \varepsilon_L \exp(i\Psi)$. This substitution eliminates the phase mismatch in Eqs. (2.48) and (2.49), and after differentiation on the LHS of Eq. (2.50), gives the following set of equations:

$$\mathcal{L}_0 A_0 = -\frac{e}{4m_e}\frac{k_L}{\omega_0}\varepsilon_L A_1, \tag{2.71}$$

$$\mathcal{L}_1 A_1 = \frac{e}{4m_e}\frac{k_L}{\omega_1}\varepsilon_L^* A_0, \tag{2.72}$$

$$\left(\mathcal{L}_L + ic_L[\partial_x \Delta k(x)]x\right)\varepsilon_L = \frac{e}{4m_e}\frac{k_L}{\omega_L}\omega_{pe}^2 A_1^* A_0. \tag{2.73}$$

The inhomogeneity is necessarily sufficiently weak such that $[\omega_{pe}(x = x_{res})^{-1}\partial_x \omega_{pe}] \ll k_{0,1,L}$ (slowly-varying envelope approximation).

In addition to detuning the three-wave resonance, inhomogeneity will cause the group velocities of the three waves to vary with the local density as they propagate. The basic conservation law for action density, valid for homogeneous or weakly inhomogeneous media, is given simply by

$$\partial_t S_i + \nabla \cdot (\vec{c}_i S_i) + 2\nu_i' S_i = 0, \tag{2.74}$$

where the action S_i of a wave labelled i is proportional to $E_i E_i^*$, c_i is the local group velocity and ν_i' is the rate of damping. We consider a simple example of an undriven EM wave propagating through a plasma that is inhomogeneous along x, from a lower density n_e^1 to a higher density n_e^2. The local wave number of the EM wave is then given by $k_i = (\omega_i/c)[1 - n_e(x)/n_c]^{1/2}$, and the local group velocity by $c_i = c^2 k_i(x)/\omega_i$. In the absence of damping, the steady state solution will obey the simple conservation of action flux, $\nabla \cdot (\vec{c}_i S_i) = 0$, and ω_i will be constant. Thus, the action fluxes in the two density regions are equal: $c_i^1 S_i^1 = c_i^2 S_i^2$. For the electric field, we find $E_i^2 = (c_i^1/c_i^2)^{1/2} E_i^1$. Since $n_e^2 > n_e^1$, we have $c_i^1 > c_i^2$ and thus $E_i^2 > E_i^1$. From this, we see that the EM wave slows as it propagates into the higher density region and grows in amplitude. This is simply understood via an argument from the conservation of photon number: as photons propagate to higher densities, their wave length increases and their group velocity slows. The photon number fluxes must be constant (equivalent to the action density flux), thus the number density at a given point must increase to conserve the flux.

In the coming chapters, where equations (2.71-2.73) are solved numerically, using varying local values of the group velocities may provoke numeric instability in three-wave coupling models. The inhomogeneity used is sufficiently weak that the approximation that the group velocities are constant throughout the window simulated is acceptable, and does not interfere with the physical discussion of autoresonance. Furthermore, as will be demonstrated in a linear density profile in Sec. 2.4.1.1, the product $c_L \partial_x \Delta k(x)$ describing the inhomogeneity does not depend directly on k_L and only varies weakly with x. However, in the kinetic (particle-in-cell) simulations presented in Chapter 5, the group velocity varies with the locally density.

2.4.1.1 Rosenbluth gain saturation

We define $x_{res} = 0$ and assume first a linear electron density gradient,

$$n_e = n_0 \left(1 + \frac{x}{L}\right) \tag{2.75}$$

where n_0 is the density at the three-wave resonance point. Under these conditions, $\omega_{pe}^2 = \omega_{pe}^2(x) = n_0(1 + x/L)e^2/m_e\epsilon_0$ and thus:

$$\partial_x \Delta k = \kappa' = \frac{\omega_{pe}^2(x=0)}{2L}\left(\frac{1}{3v_{th}^2 k_L} + \frac{1}{c^2 k_1} - \frac{1}{c^2 k_0}\right) \tag{2.76}$$

$$\approx \frac{\omega_{pe}^2(x=0)}{6v_{th}^2 L k_L}. \tag{2.77}$$

Since $3v_{th}^2 \ll c^2$ the total wave number shift is due solely to the propagation of the Langmuir wave to a good approximation.

In the much-referenced seminal paper of LPI written by Rosenbluth (1972)[20], the gain of an inhomogeneous plasma in the absence of nonlinear terms was calculated. It was shown that in the absence of nonlinear terms, a linear density profile does not support absolute growth, allowing only the convective growth until saturation of the daughter waves. The typical situation is the following: A plasma is bound by the limits $[x_L, x_R]$ (for the solution to be exact, these points lie at $\pm\infty$ on the x-axis). A forward-propagating pump wave is introduced at $x = x_L$ with intensity I_0, and a backward-propagating seed at $x = x_R$ with intensity I_1. The pump is of higher frequency than the seed, and the two EM waves are resonant with the Langmuir wave at a point $x = x_{res}$ in a plasma of linear density profile (the slope of the profile may be positive or negative). In a linear profile, it was shown that the daughter waves grow to a stable solution, displaying only a convective growth restricted to the vicinity of x_{res}. Provided that the pump is not significantly depleted by the growth of the daughter waves and that the plasma is large enough to allow the convective growth of the daughter waves to saturate, the seed was shown to be amplified in the following way:

$$I_1(x_L) = I(x_R)e^{2G_R}, \tag{2.78}$$

where G_R is the Rosenbluth gain saturation coefficient, given by

$$G_R = \frac{\pi\gamma_0^2}{|c_L c_1 \kappa'|}. \tag{2.79}$$

The level of saturation is, remarkably, independent of the damping of either daughter wave. For $\gamma_0 > \nu'_{L,1}$, the time taken to reach this saturation t_{sat} is well estimated by

$$t_{sat} \approx \frac{4\gamma_0}{|c_L c_1 \kappa'|}. \tag{2.80}$$

In the simulations presented in the coming chapters, this time is much smaller than the times for which the simulations are run. Gain saturation due to inhomogeneity is therefore an important and identifiable phenomenon. As the damping becomes large, so too does the time taken for the growth to reach saturation. In the regime $\gamma_{conv}^{min} \ll \gamma_0 < \nu'_{L,1}$,

$$t_{sat} \approx \frac{2\mathrm{max}(\nu'_{\mathrm{L}}, \nu'_1)}{|c_L c_1 \kappa'|}. \tag{2.81}$$

The key result given by Eq. 2.78 is valid only when L is sufficiently large so as to contain the region around the resonance point over which there is significant growth of the daughter waves (the case considered above being an infinite plasma). The distance from resonance to the point at which the solution changes from being growing to oscillatory, known as the “turning point”, is given by x_t, where

$$x_t = \frac{\pm 2\gamma_0}{|\kappa'||c_L c_1|^{1/2}}, \tag{2.82}$$

valid where $\gamma_0 > \gamma_{abs}^{min}$. In the regime $\gamma_{conv}^{min} \ll \gamma_0 < \gamma_{abs}^{min}$, the distance is altered to

$$x_t = \frac{\pm 1}{|\kappa'|}\mathrm{max}\left(\frac{\nu'_{\mathrm{L}}}{|\mathrm{c_L}|}, \frac{\nu'_1}{|\mathrm{c}_1|}\right). \tag{2.83}$$

These turning points lie either side of the resonance point, and together define an interaction length of $2x_t$ over which the daughter waves may grow. In the simulations and studies performed here in this thesis, $L \gg 2x_t$ (for resonance in the centre of the plasma), thus the effects of finite plasma length on the validity of this solution are not discussed. A full summary is given in Ref.[30].

For effective growth, we require $G_R > 1$. This is often approximated as

$$\left(\frac{v_{osc}}{c}\right)^2 k_0 L > 1, \tag{2.84}$$

where $v_{osc} = eA_0/m$, giving a threshold in laser intensity for SRS in inhomogeneous plasmas.

2.4.1.2 Growth in a parabolic density profile

In the following chapter, growth in a broad class of density profiles will be considered. We include here a discussion of the behaviour expected in a parabolic profile of the form

$$n_e = n_0 \left[1 + \left(\frac{x}{L}\right)^2\right], \tag{2.85}$$

giving rise to a wave number mismatch that is proportional to x^2 as opposed to x in the linear case. For the wave number mismatch gradient, we find:

$$\partial_x \Delta k = \kappa'' x = \frac{\omega_{pe}^2}{L^2}\left(\frac{1}{3v_{th}^2 k_L} + \frac{1}{c^2 k_1} - \frac{1}{c^2 k_0}\right) x \tag{2.86}$$

$$\approx \frac{\omega_{pe}^2}{3v_{th}^2 L^2 k_L} x. \tag{2.87}$$

This profile may support the absolute instability of counterpropagating daughter waves provided that the condition

$$\gamma_0 \geqslant \gamma_{abs}^{min}, \gamma_{inh} \tag{2.88}$$

is satisfied, where γ_{inh} is the inhomogeneous growth rate, given by

$$\gamma_{inh} \equiv \frac{|c_L c_1|^{1/2} |\kappa''|^{1/3}}{4^{2/3}}. \tag{2.89}$$

In the regime $\gamma_0 > \gamma_{abs}^{min}$ (where the growth is absolute), the turning points in this case lie at

$$x_{t,abs} = \pm 2 \left(\frac{\gamma_0}{|\kappa''||c_L c_1|^{1/2}}\right)^{1/2}, \tag{2.90}$$

In the regime $\gamma_{conv}^{min} \ll \gamma_0 < \gamma_{abs}^{min}$, where the growth is convective only, the turning points lie at

$$x_{t,conv} = \pm 2^{1/2} \left[\frac{\max\left(\frac{\nu_L'}{c_L}, \frac{\nu_1'}{c_1}\right)}{|\kappa''|}\right]^{1/2}, \tag{2.91}$$

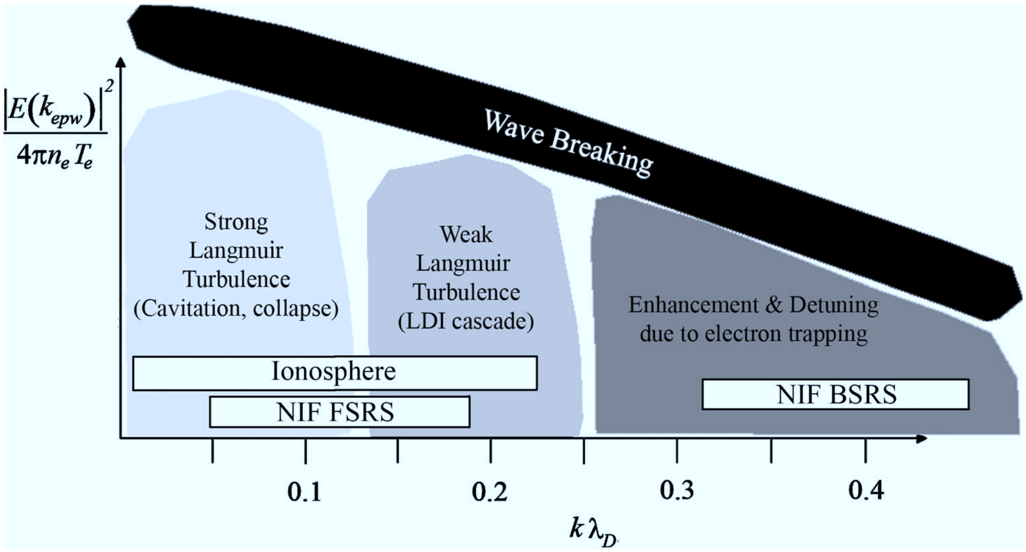

Figure 2.2: Three regimes characterised by different dominant nonlinear processes acting on the Langmuir wave, separated by distinct regions in $(k_L\lambda_D - \varepsilon_L)$ space, as defined by Kline *et al.*. Figure adapted from Kline *et al.* (2006)[4].

Finally, in the regime of strong damping, close to the threshold for convective growth where $0.5 \ll \nu \lesssim 1$, the turning points lie at

$$x_{t,thresh} = \frac{1}{2}\left(\frac{1-\nu}{\nu}\right)^{1/4} x_{t,conv}, \qquad \nu \equiv \left(\frac{\gamma_{conv}^{min}}{\gamma_0}\right)^2. \tag{2.92}$$

2.4.2 Nonlinearities and the importance of $k_L\lambda_D$

The dimensionless parameter $k_L\lambda_D$ is widely recognised as being useful as a means of theoretically determining which processes we expect to be dominant in the plasma for a given laser wavelength, plasma density and electron thermal temperature, where λ_D is the usual electron Debye length.

Kline *et al.* define by way of $k_L\lambda_D$ three distinct nonlinear regimes: Strong Langmuir wave turbulence, weak Langmuir wave turbulence, and the kinetic nonlinear regimes[4]. The size and shape of the turbulent regions defined by Kline *et al.* is based on theory and ionospheric[32,33] measurements. The onset and extent of the kinetic regime, however, are far from precisely defined, but based on particle-in-cell simulations may be applicable from $k_L\lambda_D \gtrsim 0.25$. The processes that we expected to be dominant across the $(k_L\lambda_D - \varepsilon_L)$ space are summarised in Fig. 2.2.

In the following chapter, autoresonance will be considered in two distinct regimes, namely that of low $k_L\lambda_D$, where we consider SRS in the range $k_L\lambda_D \lesssim 0.15$, and the kinetic regime, where we consider SRS in the range $k_L\lambda_D \gtrsim 0.25$. We summarise here the dominant nonlinear processes in the two regimes.

2.4.3 The fluid regime, $k_L\lambda_D \lesssim 0.15$

Through various perturbative approaches, Dewar and Lindl[34], Coffey[35] and Winjum[36] derived the correction to the Bohm-Gross relation arising from the taking into consideration of the presence of harmonics of the fundamental frequency of the Langmuir wave. Through the advective term in the ponderomotive force in Eq. 2.27, harmonics of the Langmuir wave become more important as the amplitude of the Langmuir wave grows, leading to a shift in frequency. The first harmonic does not actually produce a shift in frequency; it is necessary to calculate the second harmonic to arrive at a shift in frequency[36], while the third harmonic produces a frequency shift that is smaller by a factor of $v_{osc}/v_\phi = ek_L\varepsilon_L/n_e\omega_L^2 \ll 1$, where $v_{osc} = eA_0/m$. To lowest order and for where $v_{th} \ll v_\phi$, the following shift is obtained due to the second harmonic, dependent on the square of the Langmuir wave amplitude:

$$\omega_L^2 = \omega_{pe}^2 + 3v_{th}^2k_L^2 + \frac{15}{2}\frac{v_{th}^2}{v_\phi^4}\frac{\omega_L^4}{\omega_{pe}^2}\left(\frac{e|\varepsilon_L|}{m\omega_{pe}}\right)^2, \tag{2.93}$$

which, in the absence of a ponderomotive force or other nonlinear terms, gives

$$\left[\mathcal{L}_L + i\frac{15}{4}\frac{v_{th}^2c^2}{v_\phi^4}\frac{\omega_L^3}{\omega_{pe}^2}\left(\frac{e|\varepsilon_L|}{mc\omega_{pe}}\right)^2\right]\varepsilon_L = 0. \tag{2.94}$$

Relativistic considerations of the oscillation speed of the electrons give an additional term of similar magnitude and Langmuir wave amplitude dependence, but of differing sign. Using the expression given by Rosenbluth and Liu[37], we have for the relativistic correction

$$\left[\mathcal{L}_L - i\frac{3}{16}\omega_{pe}\left(\frac{e|\varepsilon_L|}{mc\omega_{pe}}\right)^2\right]\varepsilon_L = 0, \tag{2.95}$$

applicable when $e|\varepsilon_L|/mc\omega_{pe} \ll 1$. Since both terms are applicable in roughly the same regime, they were combined by Yaakobi *et al.*[38] to give the following total shift in Langmuir wave frequency:

$$\left(\mathcal{L}_L + i\beta|\varepsilon_L|^2\right)\varepsilon_L = 0, \quad \beta \equiv \left(\frac{15}{4}\frac{v_{th}^2c^2}{v_\phi^4}\frac{\omega_L^3}{\omega_{pe}^2} - \frac{3}{16}\omega_{pe}\right)\left(\frac{e}{mc\omega_{pe}}\right)^2 \tag{2.96}$$

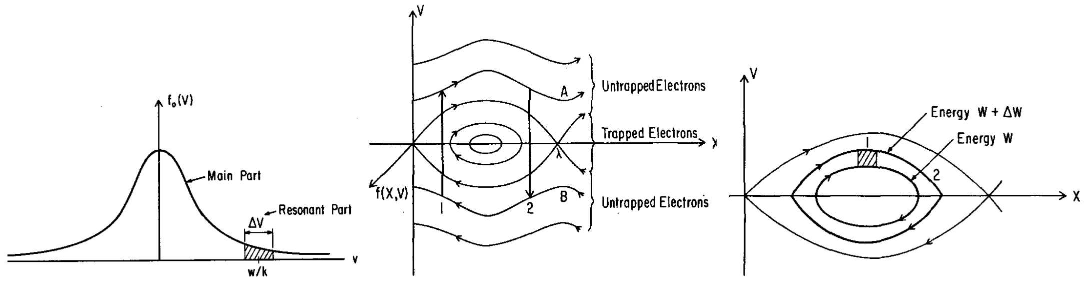

(a) (b) (c)

Figure 2.3: (a) A typical Maxwellian electron distribution function f_0, indicating the band Δv of the distribution function that is resonant with the Langmuir wave around v_ϕ. (b) The separatrix in the Langmuir wave frame, showing trapped and untrapped electron trajectories. (c) A band in phase space containing deeply trapped electrons. All figures adapted from Ref.[5].

The impact of these frequency shifts will be discussed and applied to the propagating Langmuir wave in the following chapter.

2.4.4 The kinetic regime, $k_L\lambda_D \gtrsim 0.25$

Landau damping describes a process by which energy is exchanged between a wave with phase velocity v_ϕ and particles in the plasma that interact resonantly with the wave (i.e. those that have velocities close to v_ϕ, shown in Fig. 2.3a). Particles which have velocities slightly greater than v_ϕ will lose energy, depositing it in the wave, while particles with velocities slightly lower than v_ϕ will drain energy from the wave. Ignoring nonlinear effects, the rate of Landau damping is determined solely by $k_L\lambda_D$ and, through the threshold of growth due to damping given earlier in the chapter, is important in understanding the initial onset of parametric instabilities. We parameterise Landau damping with the damping rate ν_L.

While it was already known that Landau damping exhibited nonlinear behaviour when the elapsed time t was of the order $t \sim (m/ek_LE_L)^{1/2}$, it was not until O'Neil (1965)[5] provided analytical insight into the behaviour of trapped particles that the mechanism was understood. In the so-called kinetic regime, the dominant nonlinear process originates from electron trapping in the potential well of the Langmuir wave. This electron trapping flattens the distribution of the electrons in the vicinity of v_ϕ, acting to reduce the strength of Landau damping. Landau damping is therefore highly nonlinear, dependent in this regime on the local degree of electron trapping and thus on the local amplitude of the Langmuir wave. It was shown by Vu *et al.* that linear models of Landau damping are inadequate to describe kinetic simulation results, and that a "kinetic inflation" of SRS (where Landau damping is reduced due to trapping) was likely responsible for the behaviour of the plasma reflectivity in the kinetic regime[39]. The transition from linear to nonlinear Landau damping, and from a fluid regime to a kinetic regime, was observed experimentally by Montgomery *et al.*[40] and Kline *et al.*[41] on the Trident laser facility, and continues to be an area of much research interest[42].

We consider a potential of the form $E_x(x,t) = E_L \sin(k_L x - \omega_L t)$ (i.e. a monochromatic travelling wave), as seen by a stationary observer in what is referred to as the "lab frame". In the frame of the wave, the potential is stationary and $\tilde{E}_x = E_x(x + v_\phi t, t) = E_L \sin(k_L x)$. Electrons may be roughly divided into two categories in $x - v_e$ phase space: trapped and passing. Trapped electrons are those that do not have sufficient energy to escape the potential wells of the sinusoidal stationary wave. Passing electrons are those that have sufficient kinetic energy in the frame of the wave that they pass either forwards or backwards over the peaks of the potential wells (in the lab frame, they are travelling too quickly or too slowly, respectively, to be trapped by the wave). In the wave frame, deeply trapped electrons appear to oscillate around a stationary point at the bottom of a potential well, while being swept along at an average velocity v_ϕ in the lab frame. The separatrix in the wave frame is shown in Fig. 2.3b. To second order in the wave frame, the energy W of the deeply trapped electrons (shown inside the separatrix in Fig. 2.3c) is given by the following:

$$W = \frac{1}{2} m_e v_e^2 + \frac{1}{2} e k_L E_L (x - x_0)^2 + \text{const.} \tag{2.97}$$

This equation is simply that of a harmonic oscillator with frequency

$$\omega_b = \sqrt{\frac{e k_L E_L}{m}}. \tag{2.98}$$

This deeply-trapped electron frequency is typically referred to as the "bounce frequency", related to the bounce time $\tau_b = 2\pi/\omega_b$, and is useful in parameterising the timescales relevant to electron trapping. At high Langmuir wave amplitudes, ω_b may grow to the order of the ω_L. Large numbers of formerly non-resonant electrons become trapped by the wave and are accelerated, rapidly draining energy from the wave over timescales of the order of ω_b^{-1}. Due to the sudden onset of this loss in wave energy (and consequently amplitude), this phenomenon is referred to as "wave-breaking". In warm plasmas, wave-breaking occurs at a somewhat lower amplitude than $\omega_b \approx \omega_L$ (the cold plasma limit) would suggest, since warm electrons are more easily brought into resonance. Furthermore, the electron pressure of the density perturbation of the wave provides an additional acceleration, further reducing the amplitude at which wave-breaking occurs[35].

In the regime $\omega_b^2/\omega_L \ll \nu_L \ll \omega_b \ll \omega_L$ (applicable to what we have described as the kinetic regime) and in the absence of other nonlinear effects, the Langmuir wave tends towards an undamped mode asymptotically in time, predicted in 1957 by Bernstein, Green and Kruskal[43], and commonly referred to as a BGK mode. This process takes only a few bounce periods, after which the electrons are fully sorted into being either trapped or untrapped and there is no longer a net exchange of energy with the wave over a bounce cycle. Landau damping is therefore not generally included in the equations governing the Langmuir wave used in various discussions later in this thesis, since it quickly becomes insignificant for timescales of $1-2$ ps (although it is not omitted from 3-wave or kinetic simulations).

2.4.4.1 The kinetic nonlinear frequency shift

In addition to altering the Landau damping rate, trapped particles in the kinetic regime play another important role: Trapped electrons are effectively removed from the bulk of the distribution, resulting in a localised drop in the electron pressure (defined earlier in the chapter when deriving the equation governing the propagation of the Langmuir wave). This modification of the electron distribution function results in a negative frequency shift of the Langmuir wave that is proportional to the square root of the Langmuir wave amplitude. The negative shift may be intuitively understood simply by noting that since $\omega_L \sim \omega_{pe} = \sqrt{n_e/n_c}$, a reduction of the local density will result in a lower plasma, and therefore Langmuir wave, frequency.

The resultant nonlinear Langmuir wave frequency may be written as the sum of its linear ω_L^l and nonlinear $\delta\omega^{nl}$ components such that $\omega_L = \omega_L^l - \delta\omega^{nl}$, where ω_L^l is given by the usual Bohm Gross relation. The nonlinear frequency component was calculated by Morales and O'Neil[18] to be the following:

$$\delta\omega^{nl} = \frac{\alpha}{\frac{\partial\epsilon_L}{\partial\omega}\big|_{\omega_L}} \frac{\omega_{pe}^2}{k_L^2} \Delta v_t \frac{\partial^2 f_0}{\partial v^2}\bigg|_{v_\phi}, \tag{2.99}$$

where ϵ_L is the dispersion relation of the Langmuir wave, $\Delta v_t = 2\omega_b/k_L$ is the velocity of deeply trapped electrons and f_0 is the unperturbed initial electron distribution function, normalised to n_0. The constant α is a numerically determined integral containing contributions α_t and α_{nt} from both trapped and nearly trapped electrons, respectively, where $\alpha = \alpha_t + \alpha_{nt} = 0.705 + 0.117 = 0.823$.

Using the approximated form of the dispersion relation $\epsilon_L \sim 1 - \omega_{pe}^2/\omega^2$ relevant to a cold fluid and the numerical value of α, we arrive at the following for the frequency shift:

$$\delta\omega^{nl} = 0.83\omega_L v_\phi^2 \left(\frac{e|\varepsilon_L|}{mk_L}\right)^{1/2} \frac{\partial^2 f_0}{\partial v^2}\bigg|_{v_\phi}, \tag{2.100}$$

This frequency shift, proportional to the square root of the Langmuir wave envelope amplitude, is often written simply as the following:

$$\delta\omega^{nl} = \tilde{\eta}|\varepsilon_L|^{1/2} \tag{2.101}$$

$$= \eta\omega_L \left|\frac{\delta n_e}{n_0}\right|^{1/2}, \tag{2.102}$$

for which

$$\tilde{\eta} \equiv 0.83\omega_L v_\phi^2 \left(\frac{e}{mk_L}\right)^{1/2} \frac{\partial^2 f_0}{\partial v^2}\bigg|_{v_\phi}, \quad \eta \equiv \frac{1}{\omega_L}\sqrt{\frac{n_0 e}{\epsilon_0 k_L}}\tilde{\eta} \tag{2.103}$$

where ε_L and $\delta n_e/n_0$ are simply related via Poisson's Law. There are several known expressions for the parameter η, the choice of which depends on the type of problem being considered (for example, whether the Langmuir wave is switched on suddenly or whether it is switched on adiabatically). However, the differences between these expressions are small, and all are consistent in predicting a negative frequency shift of the form given by Eq. (2.102). For the purposes of discussion, η is therefore held as a positive free parameter. To ensure the appropriate value of η is used in calculations and simulations, η is measured directly from PIC simulations in Chapter 5.

Similarly, kinetic effects in the evolution of IAWs are also important, but here the situation is more complex since both electrons and ions contribute terms of differing sign to the frequency shift[44]. Electron trapping may lead to a modulational instability,[45] typically referred to as the Trapped Particle Modulational Instability (TPMI). The importance of trapping has been observed in 2D[46] and 3D simulations[47]. In higher-dimension simulations (D> 1), LDI, self-focusing and filamentation of the Langmuir wave are also of great importance[48,49], each of which is affected by trapping.

Many attempts in the last 10 years have been made to better model kinetic effects in fluid models owing to the relevance to current ICF experiments and the difficulty of analysing kinetic simulations directly. Building on the theoretical descriptions of electron trapping first proposed in the 1960s, the last ten years has seen a large number of attempts to describe the results of kinetic simulations. Using an expression for the kinetic nonlinear frequency shift equivalent to that derived by Morales and O'Neil[18], Vu *et al.* (2002)[39] proposed a model similar to that described in this thesis for SRS and found agreement with reduced PIC simulations. Rose and Russell (2001)[50] derived a model based on the determination of the electron susceptibility in order to model kinetic effects, and found that their model suggested that efficient SRS amplification was not possible for $k_L\lambda_D \gtrsim 0.53$, although Vu *et al.* found significant SRS levels as high as $k_L\lambda_D = 0.55$. Lindberg *et al.* (2005)[51] developed a model in good agreement with Vlasov simulations for $k_L\lambda_D < 0.3$ through use of a carefully-chosen phenomenological description of electron trapping effects based on measurements taken from Vlasov simulations. In the context of Raman amplifiers, Yamplosky and Fisch (2009)[52] derived an expression for the time-dependent nonlinear Landau damping. Bénisti *et al.* (2010)[53] have proposed a relatively unconventional model that includes nonlinearity in the group velocity of the Langmuir wave and found agreement with the initial SRS growth observed in Vlasov simulations.

Many other models have been proposed, often applicable to slightly different regimes and with different purposes in mind. The approach in this thesis is most similar to that taken by Vu *et al.*, owing to its suitability for analytical study (the relatively complex and highly nonlinear model suggested by Bénisti *et al.*, for example, does not lend itself to analytic study). It should be stressed that the model presented here is not an attempt to capture the broad range of physics present in kinetic simulations or indeed experiments, but is meant instead to illuminate the key processes responsible for the behaviour of SRS in the kinetic regime.

2.5 Autoresonance

The various terms described at the end of this chapter all act to detune the three-wave resonance. A natural question arises: what happens when two or more shifts are combined? If the plasma is inhomogeneous and kinetic effects are important, there will be a shift both in wave number and in Langmuir wave frequency. In this instance, we write the following equation for the Langmuir wave, relevant to a warm plasma with a linear density profile in the kinetic regime:

$$\left(\mathcal{L}_L + ic_L\kappa' x - i\tilde{\eta}|\varepsilon_L|^{1/2}\right)\varepsilon_L = \frac{e}{4m_e}\frac{k_L}{\omega_L}\omega_{pe}^2 A_1^* A_0 \tag{2.104}$$

We consider the part of the plasma *ahead* of the resonance point, $x > 0$, towards which a Langmuir wave generated resonantly at $x = x_{res} = 0$ will propagate. Initially, the Langmuir wave amplitude is zero. It is clear that if $\kappa' < 0$, the two shifts will add to produce a larger negative shift away from resonance. However, if $\kappa' > 0$, the two shifts will, partially or totally, cancel each other out.

As discussed earlier in the chapter, the Langmuir wave will undergo a shift in wave number as it propagates away from the resonance point. At and around x_{res}, the Langmuir wave will experience a convective growth in the linear profile. As the Langmuir wave amplitude grows, electron trapping will begin to modify the distribution function, leading to a shift in the frequency of the Langmuir wave. The two shifts are of opposing sign, so whatever their respective magnitudes, they will at least partially cancel in the region $x > x_{res}$.

It is instructive to consider the wave number shift as something that is externally imposed upon the Langmuir wave. The ponderomotive force that drives the Langmuir wave may be considered in this way to be swept in wave number through space, much like a driver of a pendulum being swept in frequency through time (in reality, it is the wave number of the Langmuir wave, not the driver, that is swept). In the fluid regime, where the frequency shift of the Langmuir wave is due to thermal and relativistic effects as opposed to electron trapping, Yaakobi *et al.* [38] showed that the Langmuir wave can *phase lock* to the driver as it passes through resonance. During phase-locking, the Langmuir wave may then self-adjust its amplitude to maintain resonance with the driver as the Langmuir wave propagates. This process of automatic (without feedback) amplitude adjustment in order to maintain resonance is referred to as "autoresonance". The amplitude of the Langmuir wave must therefore grow in a predictable fashion, such that the two shifts remain equal and of opposite sign.

In this thesis, autoresonance in the kinetic regime is explored in the context of SRS. This phenomenon of cancellation between the two shifts forms the basis of the autoresonance mechanism that is the focus of this thesis.

2.6 Normalisation

We include here a brief note on normalisation in the coming chapters. It is convenient both in numeric simulations and calculations to normalise time and space by $t' = \omega_0 t$ and $x' = k_0 x$, respectively, and to normalise all fields by E_0, the maximum electric field amplitude of the pump wave at the LHS boundary of the simulation window. The quoted values of various parameters will be presented as unitless quantities normalised in this way unless the units are explicitly given.

2.7 Chapter summary

In this chapter, the three equations governing the propagation of an incident electromagnetic wave (the laser), a scattered electromagnetic wave and a driven electron-plasma wave (the Langmuir wave) through an inhomogeneous electron plasma density profile were derived. To these equations, wave-particle interactions, or kinetic effects, were subsequently introduced in the form of Landau damping and a nonlinear frequency shift that varies with the local amplitude of the Langmuir wave. Individually, the wave number shift of the three waves due to the inhomogeneity of the plasma and the nonlinear frequency shift due to kinetic effects both act to detune the three-wave resonance and saturate the growth of the Langmuir wave. Together, however, there is the possibility that these two effects may negate each other either partially or totally, allowing for the onset of autoresonance.

The autoresonant behaviour of the Langmuir wave, and the resultant impact on the behaviour of the electromagnetic waves, is explored in the following chapters, first analytically and subsequently in simulations.

Chapter 3

Autoresonance

In this chapter, the mechanism of autoresonance is discussed in detail. The simplest example is perhaps the driven pendulum, and it is this weakly nonlinear oscillator that is first used to introduce autoresonant behaviour and to demonstrate phase-locking between a nonlinear oscillator and its driver. Beginning from the equation governing the propagation of the Langmuir wave in a warm inhomogeneous plasma derived in the previous chapter, the impact of additional nonlinear terms is considered. Through the use of examples in the $k_L\lambda_D \lesssim 0.15$ regime, where the dominant frequency shift of the Langmuir wave arises due to fluid effects, and examples in the regime $k_L\lambda_D \gtrsim 0.25$, where the dominant frequency shift is due to kinetic effects, the robustness of autoresonance is explored. Autoresonance is shown to be a possible mechanism of Langmuir wave growth, which may far exceed the linear response to a fixed driver. Autoresonance is shown to be possible in any density profile that is of a positive gradient, and is shown to display a low sensitivity to nonlinear Landau damping in the kinetic regime.

An analytic model describing the behaviour of the autoresonant Langmuir wave is developed that is shown to be in agreement with numerical solutions to the Langmuir wave equation. Although the analysis and simulations presented here are 1D, studies by Frièdland[54] have shown that autoresonance is not susceptible to weak transverse nonuniformity in the interacting waves. Additionally, autoresonance was demonstrated in the fluid regime in 3D systems[55].

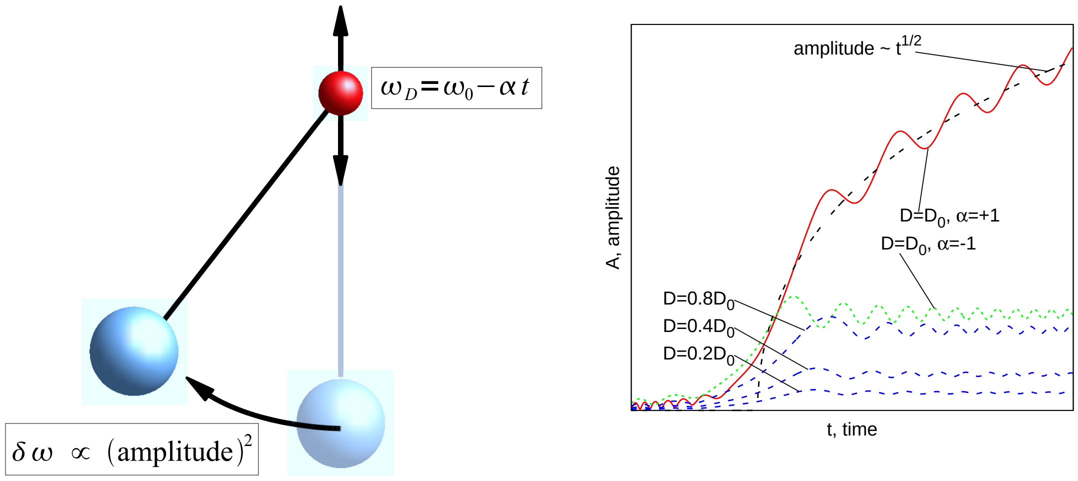

(a) (b)

Figure 3.1: (a) A pendulum of natural frequency ω_0, driven at a swept frequency ω_D. The pendulum oscillates at a frequency that decreases as the amplitude of oscillation grows. (b) The response of the pendulum to varying driver strengths D and driver frequency sweep direction α, showing linear responses below threshold (blue dashed lines) and autoresonance above threshold (red solid line). Also shown is the non-autoresonant response of the pendulum to a driver that is swept in frequency in the opposite direction (green dotted line).

3.1 Introduction to autoresonance

3.1.1 The pendulum

How can a nonlinear oscillator be driven to high amplitude without feedback? We consider first the simple case of a driven pendulum. If a drive of fixed frequency is applied to the pendulum, the amplitude of oscillation will initially increase. However, as the amplitude of the oscillation grows, the oscillation frequency will fall and the pendulum will quickly dephase from the driver, saturating the growth in amplitude. The result is a weak linear response to the driver, with the amplitude performing oscillations around a small and constant average value.

Consider now a driver frequency that is swept in time, decreasing and passing through the natural frequency ω_0 of the pendulum (see Fig. 3.1a). Under certain conditions, the pendulum may phase-lock to the driver. This well-known phenomenon is described in detail in Ref.[56]. During phase-locking, the pendulum will self-adjust its instantaneous amplitude in order to maintain resonance with the driver, allowing for the efficient exchange of energy between driver and pendulum.

We take as our point of departure the equation of a pendulum driven at a frequency ω_D that decreases according to $\omega_D = \omega_0 - \alpha t$, where t is the time, beginning at $t \ll 0$:

$$\ddot{\theta} + \omega_0^2 \sin\theta = \bar{D}\cos(\omega_0 t - \alpha t^2/2), \tag{3.1}$$

for which θ is the angle between the pendulum and the vertical and $\bar{D}$ parameterises the driver strength. In the weakly nonlinear limit,

$$\ddot{\theta} + \omega_0^2\left(\theta - \frac{\theta^3}{6}\right) = \bar{D}\cos(\omega_0 t - \alpha t^2/2) = \bar{D}\mathrm{Re}[\mathrm{e}^{\mathrm{i}(\omega_0 \mathrm{t} - \alpha \mathrm{t}^2/2)}]. \tag{3.2}$$

We begin by making the substitution $\theta = \mathrm{Re(A)}$. In the weakly nonlinear limit, A should have a frequency that remains close to ω_0. We therefore split A into slowly- and quickly-varying components, such that

$$A = A_s e^{i\omega_0 t}, \tag{3.3}$$

where $|A|^{-1}|\dot{A}| \ll \omega_0$. The detuning of A from its linear frequency is now contained in the slowly-varying phase of A_s, and

$$\dot{A} = \left(\dot{A}_s + i\omega_0 A_s\right) e^{i\omega_0 t}, \tag{3.4}$$

$$\ddot{A} = \left(\ddot{A}_s - \omega_0^2 A_s + 2i\omega_0 \dot{A}_s\right) e^{i\omega_0 t} \tag{3.5}$$

$$\approx \left(2i\omega_0 \dot{A}_s - \omega_0^2 A_s\right) e^{i\omega_0 t}. \tag{3.6}$$

Upon substitution into Eq. 3.2, we find

$$\dot{A}_s + i\frac{\omega_0 |A_s|^2}{16} A_s = -iDe^{-i\alpha t^2/2}, \tag{3.7}$$

where the approximation $\theta^3 \approx \mathrm{Re}[(3/4)|A_s|^2 A_s \exp(i\omega_0 t)]$ has been used and $D = \bar{D}/2\omega_0$ is the real normalised driver strength. Making the substitution $a_s = A_s \exp(i\alpha t^2/2)$, we may then write the following equation for the weakly-nonlinear pendulum:

$$\dot{a}_s + i\left(\frac{\omega_0 |a_s|^2}{16} - \alpha t\right) a_s = -iD. \tag{3.8}$$

In Eq. (3.8), the term $i\alpha t$ is due to the frequency shift of the driver, while $-i(\omega_0/16)|a_s|^2$ is the nonlinear frequency shift of the pendulum. During autoresonance, these two terms must cancel, allowing the efficient driving of θ by $\bar{D}$. Solutions to this equation are plotted in Fig. 3.1b for a range of parameters.

It is clear that in order for autoresonance to take place, $\alpha > 0$, and for exact cancellation of the frequency shifts we expect

$$|a_s| = \left(\frac{16\alpha}{\omega_0}\right)^{1/2} t^{1/2}. \tag{3.9}$$

When $\alpha < 0$, the pendulum responds essentially linearly (Fig. 3.1b, green dotted line). For $\alpha > 0$, the pendulum exhibits a sharp threshold behaviour: When the drive is below this threshold, autoresonance is not possible and the pendulum responds linearly to the drive (Fig. 3.1b, blue dashed lines). Above this threshold, autoresonance is observed, and the solution does not change significantly as the driver strength is increased further still (Fig. 3.1b, solid red line) until the pendulum leaves the weakly nonlinear regime. The observed autoresonant solution matches closely the curve expected if the cancellation between the frequency sweeping of the driver and the nonlinear frequency shift of the oscillation of the pendulum were exact, given by Eq. (3.9) (Fig. 3.1b, black dashed line). This behaviour is explained later in the chapter.

The equation governing the slowly-varying amplitude of the pendulum, Eq. (3.8), differs only trivially from the time-stationary equation of the Langmuir wave in the regime where the dominant nonlinear frequency shift arises due to fluid effects and the driving term is constant. This equation is similar also to the time-stationary equation of the Langmuir wave in the kinetic regime. While Langmuir waves evolve both in time and space, characteristics of the equation governing the propagation of the Langmuir wave in either regime may be constructed so that the resultant behaviour is analogous to the pendulum.

3.1.2 Autoresonance in other contexts

In addition to the simple pendulum, autoresonance may be observed in a wide variety of systems and is important in many experiments. It is particularly useful due to the absence of feedback in maintaining resonance; feedback in many situations is simply impossible to obtain and respond to with the necessary speed and precision required to maintain resonance artificially. Autoresonance was observed in electron beams in accelerators as early as 1945[57,58], and is used in modern accelerators to prepare the beam, where autoresonance in the cyclotron motion[59] of electrons in a magnetic field is utilised as a means of acceleration. Autoresonance has been observed in superconducting Josephson junctions[60], and the threshold effect may have useful applications to quantum state measurements.

Many applications of autoresonance have been considered in plasmas. At high Langmuir wave amplitudes, relativistic effects become important as the oscillation frequency of the electrons approaches c (discussed previously in Sec. 2.4.3), leading to the detuning of the Langmuir wave from a fixed-frequency driver[37]. In order to maintain resonance, a method of using a "chirped" driver, in which the frequency was decreased rapidly in time, was investigated for the first time by Ghizzo *et al.*[61]. In Vlasov simulations, the relativistic shift was seen to phase-lock to the chirping of the drive, allowing the driving of Langmuir waves to unconventionally high amplitudes with a view to particle acceleration. Autoresonance has also been used in experiments such as those conducted by Andresen *at al.*[62] in which a chirped frequency drive was used to autoresonantly excite an antiproton plasma in order to drive anitprotons into positrons to form antihydrogen.

The impact of autoresonance in SBS was discussed by Maximov *et al.*[63], then investigated by Williams *et al.*[64]. In the case discussed by Williams, trapping alters the frequency of the ion acoustic wave. In the presence of a plasma flow, such as that which might exist near the entrance to a hohlraum, the autoresonant behaviour of the ion acoustic wave may alter the energy transferred between the crossing beams, and is thus of relevance to ICF experiments.

Despite the success and wide use of BGK models for plasma waves, direct observation of such a wave has proved difficult. Autoresonance has been proposed as a mechanism by which such a wave could be excited and directly observed in a controlled fashion, rather than via instabilities such as SRS. Khain *et al.*[65] recently built on a model proposed by Frièdland[66] where a "hole" in phase space may be autoresonantly excited in the plasma through the use of a chirped drive, forming a BGK mode that could then be driven to high amplitude and directly observed.

3.2 Autoresonance at low $k_L\lambda_D$

Autoresonance in SRS was investigated by Yaakobi *et al.*[38] in a regime where the dominant nonlinear frequency shift was due to harmonics of the Langmuir wave and relativistic effects. In this regime, a growing Langmuir wave undergoes a shift in frequency that is proportional to the square of its amplitude. While the parameters used by Yaakobi are not of relevance to ICF experiments, this regime provides a useful introduction into the mechanism of autoresonance, and has interesting similarities and differences to the kinetic regime that is the focus of this work.

Derived in the previous chapter, the equation governing the motion of the Langmuir wave through a linear density profile in this regime is the following:

$$\left(\mathcal{L}_L + i\beta|\varepsilon_L|^2 + ic_L\kappa' x\right)\varepsilon_L = P. \tag{3.10}$$

where $P = (ek_L\omega_{pe}^2/4m_e\omega_L)A_1^*A_0$ is the ponderomotive drive for which the EM wave envelope amplitudes are prescribed (constant). Prescribing the amplitudes

$A_{0,1}$ allows the phenomenon of autoresonance to be investigated and analysed separately from SRS. The results of this analysis are later be applied to full three-wave coupling in the following chapters.

The strength of the nonlinear fluid frequency shift is parameterised by β, for which

$$\beta \equiv \left(\frac{15}{4} \frac{v_{th}^2 c^2}{v_\phi^4} \frac{\omega_L^3}{\omega_{pe}^2} - \frac{3}{16} \omega_{pe} \right) \left(\frac{e}{mc\omega_{pe}} \right)^2 \tag{3.11}$$

The parameter β is composed of two terms of differing sign. The term that dominates (and therefore the sign of β) is dependent on the values of ω_L, k_L and thus may change depending on whether FSRS or BSRS is considered. Typically, $\beta > 0$ for BSRS and $\beta < 0$ for FSRS. The parameter κ', parameterising the wave number detuning due to propagation through a linear density profile $n_e = n_0(1 + x/L)$ and defined in Eq. 2.77, is of a sign that depends on the direction of the density gradient: For $L > 0$ (referred to as a positive density profile), $\kappa' > 0$; for $L < 0$ (referred to as a negative density profile), $\kappa' < 0$. As in the case of the pendulum in the previous section, it is clear that autoresonance requires the wave number shift and the fluid nonlinear frequency shift to be of differing sign. Thus, for autoresonance to occur, the density gradient must be negative in the case of BSRS and positive in the case of FSRS[1]. Since the Langmuir wave propagates in the positive x-direction, autoresonance may only occur to the right ($x > 0$) of the resonance point $x = x_{res} = 0$.

The case considered by Yaakobi is applicable to a CO_2 laser (i.e. a laser wavelength much longer than the Nd:glass laser wavelength used in current ICF experiments and throughout this thesis). With the usual normalisation, Eq. (3.10) was solved under the following conditions: $n_0 = 5.6 \times 10^{17}$ cm^{-3} [or $n_e(x = 0)/n_c = 0.05$], $T_e = 0.1$ keV, $\lambda_0 = 10$ μm, $I_0 = 2 \times 10^{13}$ Wcm^{-2}, and $I_1 = 1.8 \times 10^8$ Wcm^{-2}, where $I_{0,1}$ are the intensities of the pump and seed that ponderomotively drive the Langmuir wave, here switched on at time $t = 0$ and constant throughout the simulation window. The plasma was chosen to have an electron density profile of the form $n_e = n_0(1+x/L)$, where $L = \pm 1$ cm. Using these parameters, at $x = 0$ we find $\omega_L = 0.23$, $k_L = 1.714$, $k_L\lambda_D = 0.11$, $P = 1.4 \times 10^{-5}$ and $\beta = 1.5 \times 10^{-2}$ for BSRS, and $\omega_L = 0.22$, $k_L = 0.23$, $k_L\lambda_D = 0.014$, $P = 1.9 \times 10^{-6}$ and $\beta = -1.2 \times 10^{-3}$ for FSRS. It can be seen in Fig. 2.2 that this is far from the kinetic regime.

While autoresonance in both the BSRS and FSRS cases is possible, only BSRS is typically important. This is due to two reasons: First, the Langmuir wave group velocity c_L is significantly smaller in the FSRS case. Since the growth of the Langmuir wave is tightly bound to the velocity at which the autoresonant wave front may propagate, the growth rate in the FSRS case is greatly reduced compared to

---

[1] The reverse is erroneously stated in Ref. [38].

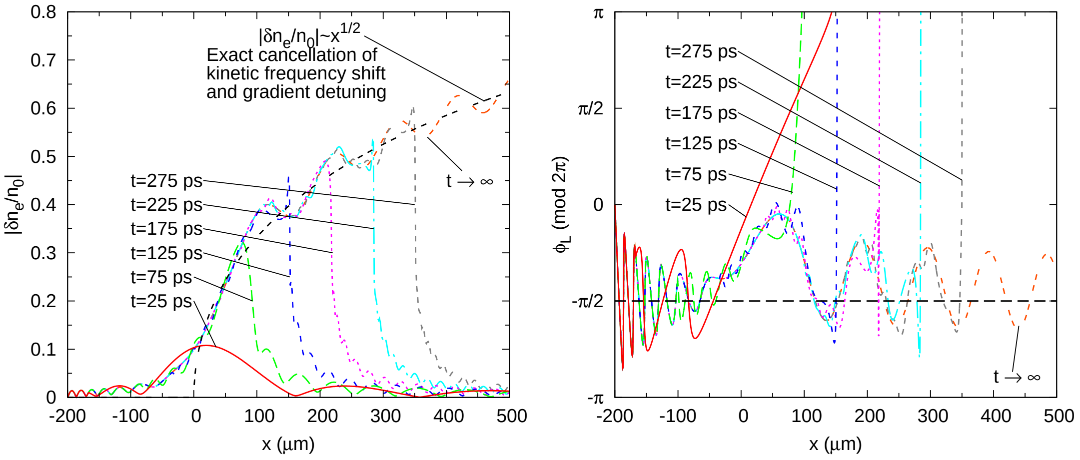

Figure 3.2: (Left) The envelope amplitude of the autoresonant Langmuir wave in the regime where the dominant frequency shift arises due to fluid effects. The black dashed line indicates the amplitude expected from an exact cancellation of the fluid frequency shift and the wave number shift due to inhomogeneity. (Right) The phase of the Langmuir wave, showing phase-locking around $\phi_L = -\pi/2$. The phase-locked region extends in tandem with the autoresonant wave front.

the BSRS case (in the case considered here, $c_L^{\mathrm{BSRS}}/c_L^{\mathrm{FSRS}} \approx k_L^{\mathrm{BSRS}}/k_L^{\mathrm{FSRS}} = 7.4$). Second, in the regime considered here where fluid nonlinear effects are dominant, the value of ω_L lies very close to ω_{pe}. In the FSRS case, the density gradient must be positive, and thus ω_{pe} increases as a function of distance. Since $k_L = [\omega_L^2 - \omega_{pe}^2(1 + x/L)]$, k_L quickly approaches zero and the Langmuir wave becomes evanescent.

3.2.1 The method of characteristics

In order to solve Eq. (3.10), we employ the method of characteristics and a simple finite difference scheme. The characteristics of equation (3.10) are the straight lines $x = (c_L/c_0)t + s_*$ in the (x,t)-plane, intercepting the x-axis at s_*, where s_* is real and of fixed value along a given characteristic. We make now the substitutions $t = (c_0/c_L)(s - s_*)$ and $x = s$, where s is a real variable. Therefore, along a given characteristic with a constant value of s_*, we may use the total derivative of ε_L with respect to s to rewrite equation (3.10) as the ordinary differential equation

$$\left(\frac{d}{ds} + i\beta|\varepsilon_L|^2 + ic_L\kappa' s\right)\varepsilon_L = P. \tag{3.12}$$

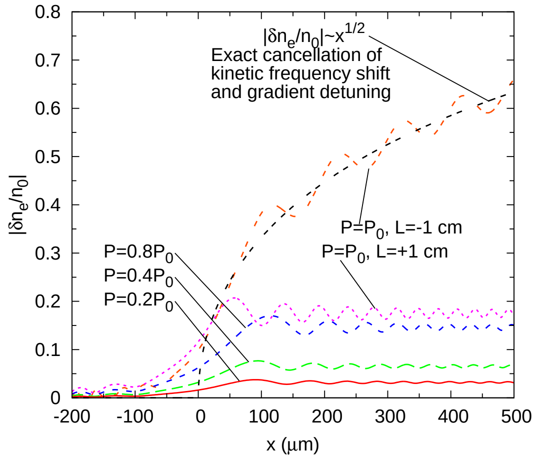

Figure 3.3: The envelope amplitude of the autoresonant Langmuir wave in the regime where the dominant frequency shift arises due to fluid effects. The black dashed line indicates the amplitude expected from an exact cancellation of the fluid frequency shift and the wave number shift due to inhomogeneity. A sharp threshold in driver strength is present at $P/P_0 \sim 0.9$.

The characteristic of the Langmuir wave evolution is analogous to the equation governing the behaviour of the weakly nonlinear pendulum, Eq. (3.8).

We consider a plasma with the LHS and RHS boundaries x_L, x_R. A prescribed ponderomotive drive $P = P(t) = P_0 H(t)$ is applied, where H is the Heaviside function and P_0 is a constant, and the system is solved up to a time t_{max}. Equation (3.12) is easily solved numerically with boundary conditions $\varepsilon_L(s = x_L) = 0$ and ε_L, $P = 0$ for $s < s_*$. By solving in the domains $s \in [x_L, x_R]$ and $s_* \in [x_L - (c_L/c_0)t_{max}, x_R]$, the full spatio-temporal evolution of ε_L may be recovered up to time t_{max}. By simply neglecting the temporal derivative ∂_t in Eq. (3.10), the time-stationary case $(t \to \infty)$ may also be obtained, towards which the system evolves.

The solution to Eq. (3.12) in the BSRS case is shown in Fig. 3.2. As the Langmuir wave propagates from the point of resonance $x = 0$, it grows in amplitude in a predictable fashion, namely that which would be expected if the cancellation of the nonlinear fluid frequency shift and the wave number detuning due to inhomogeneity were exact, or

$$i\beta|\varepsilon_L|^2 = ic_L\kappa' x \implies |\varepsilon_L| = \left(\frac{c_L\kappa'}{\beta}\right)^{1/2} x^{1/2}. \tag{3.13}$$

In this case, the autoresonant wave front simply propagates at the group velocity c_L. This exact cancellation is also plotted in Fig. 3.2 (black dashed line). The phase of the Langmuir wave ϕ_L is also shown in Fig. 3.2. The phase is observed to oscillate around a constant average value of $\phi_L = -\pi/2$ over a region that extends at the group velocity, corresponding to the distance propagated by the autoresonant wave front (In the FSRS case, the phase is locked at $\phi_L = +\pi/2$. Taking the conjugate of Eq. (3.12) transforms between the two cases, hence the change of sign in ϕ_L.).

Autoresonance of this type exhibits a sharp threshold phenomenon in the strength of the driver. A detailed explanation of this phenomenon is given later in the chapter. In Fig. 3.3, the response of the Langmuir wave to drives of various strengths in shown. For $P = P_0$ and below, the system is not autoresonant and the amplitude quickly saturates at a comparatively low level (the threshold is found at $P/P_0 \sim 0.9$). Below threshold, it is clear that halving the driver strength will halve the response in amplitude of the Langmuir wave. We identify this as the "linear regime". After the threshold in P is passed, increasing the drive has no significant impact on the behaviour of the Langmuir wave compared to the $P = P_0$ case, unless the linear response is greater still than the amplitude that would otherwise be reached through autoresonance. Also shown in Fig. 3.3 is the BSRS case when the gradient is of the incorrect (positive) sign for autoresonance to arise. Linear behaviour is once again observed.

3.2.2 Growth rate of fluid-type autoresonance and relevance to the NIF

By making the substitutions $\zeta = \sqrt{|\kappa'|}x$, $\tau = c_L\sqrt{|\kappa'|}t$ and $|\beta|\varepsilon_L^2 = c_L\sqrt{|\kappa'|}G^2$, Eq. 3.10 may be renormalised such that there is only a single free parameter. In the case of BSRS (and therefore a negative density profile), we find

$$\left(\partial_\tau + \partial_\zeta - i\zeta + i|G|^2\right) G = \Upsilon, \tag{3.14}$$

where $\Upsilon = \sqrt{\beta}/(c_L\kappa')^{3/2}P$. The threshold for whether autoresonance occurs is then only dependent on this single parameter Υ. It is shown later in the chapter that the critical value in driver strength, Υ_c, is simply given by $\Upsilon_c = (1/3)^{3/4}$. It is clear that given sufficient driver strength, autoresonance may occur for a very wide range of parameters. However, in full three-wave coupling, other processes may dominate the autoresonant growth. The important question, then, is whether the autoresonant growth rate is greater or smaller than other growth rates, particularly the convective growth rate γ_0 of SRS, and whether the saturation level of other growths is high enough to mask the effect of autoresonance.

We make here a general remark about spatially autoresonant growth in the low $k_L\lambda_D$ regime. For the reasons given earlier in the chapter, autoresonance in FSRS is unlikely to be significant in determining the behaviour of the Langmuir wave and ultimately the reflectivity of the plasma. Autoresonance in BSRS, while capable of provoking a significant growth in the Langmuir wave, may only arise in a negative density profile, essentially limiting the relevance for ICF to indirect-drive schemes where the density gradient in the plasma inside the hohlraum is less certain to be increasing over the whole of the path that the laser beam travels. In the low $k_L\lambda_D$ regime, the autoresonant wave front propagates at the group velocity of the Langmuir wave. Consequently, the temporal growth rate of the autoresonant solution is bound to the group velocity of the Langmuir wave (there are exceptions to this in three-wave coupling in the kinetic regime, discussed in the following chapter). Indeed, since the position of the wave front is given approximately by $c_L t$ (where $t = 0$ coincides with the laser beam passing through the resonance point), we may write for the autoresonant Langmuir wave amplitude

$$|\varepsilon_L| = \left(\frac{c_L\kappa'}{\beta}\right)^{1/2} (c_L t)^{1/2}, \tag{3.15}$$

and, for temporal growth rate of the maximum instantaneous amplitude (i.e. the amplitude at the autoresonant wave front) $|\varepsilon_L|_{max}$, we may write

$$\frac{d|\varepsilon_L|}{dt} = \frac{1}{2}\left(\frac{c_L\kappa'}{\beta}\right)^{1/2}\left(\frac{c_L}{t}\right)^{1/2} \tag{3.16}$$

Since the group velocity is given by $c_L = 3v_{th}^2 k_L/\omega_L = 3v_{th}(k_L\lambda_D)$, low values of $k_L\lambda_D$ (or even simply T_e) result in a slow autoresonant growth rate. For these reasons, autoresonance in the fluid regime is unlikely to be of relevance to the NIF.

3.3 Autoresonance in the kinetic regime

We consider now the regime discussed at the end of the previous chapter, where the dominant nonlinear frequency shift of the Langmuir wave is due to kinetic effects. The frequency shift in this case is proportional to the square root of the amplitude of the Langmuir wave, and we write the following for the Langmuir wave:

$$\left(\mathcal{L}_L + ic_L\kappa' x - i\tilde{\eta}|\varepsilon_L|^{1/2}\right)\varepsilon_L = P. \tag{3.17}$$

As discussed in the previous chapter, ICF experiments may provide conditions where autoresonance is strongly driven, with laser light encountering a relatively high-amplitude back-scattered beam near the entrance to a hohlraum and providing the ponderomotive drive. Autoresonance may also arise in a much more weakly-driven case, instead growing out of thermal noise in the plasma. For simplicity, we begin by discussing the strongly-driven case.

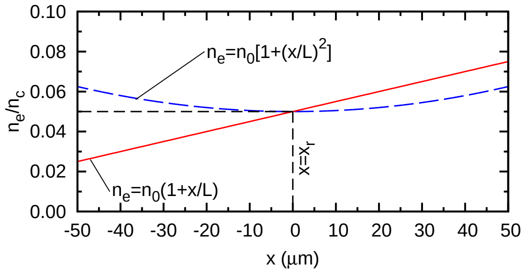

Figure 3.4: Electron density profile of the plasma used in simulations where the Langmuir wave has a prescribed driver for linear (red solid line) and parabolic (blue dashed line) density profiles. The density scale length L is equal in both cases.

We wish first to demonstrate that autoresonance is possible in the kinetic regime. Furthermore, we wish also to show that the phenomenon of autoresonance is not unique to a linear density profile. To this end, we define a positive linear density profile,

$$n_e = n_0(1 + x/L), \tag{3.18}$$

and a parabolic density profile,

$$n_e = n_0[1 + (x/L)^2], \tag{3.19}$$

It will be shown later, however, that cubic and higher powers still permit autoresonance. The Langmuir wave is initially resonant with the drive at $x = x_{res} = 0$ in both density profiles, shown in Fig. 3.4. We again restrict our discussion to BSRS; in addition to the lowering of c_L, the low values of $k_L\lambda_D$ associated with FSRS mean that kinetic effects are not usually significant.

For the linear profile, we have as before the following equation describing the envelope of the Langmuir wave:

$$(\partial_t + c_L\partial_x + ic_L\kappa' x - i\tilde{\eta}|\varepsilon_L|^{1/2})\varepsilon_L = P, \tag{3.20}$$

Defining $k_0 - k_1 - k_L = \Delta k = \kappa' x$, we find $\kappa' = \partial_x \Delta k \sim \omega_{pe0}^2/6Lv_{th}^2 k_L$, for which $\omega_{pe0} = \omega_{pe}(x = 0)$. Specifically, in this linear profile case, κ' is only dependent on x through k_L, thus varies weakly in space until k_L approaches its vanishing point. The cancellation between the wave number detuning and the kinetic nonlinear frequency shift thus leads to a parabolic growth in the Langmuir wave envelope amplitude, or

$$\left|\frac{\delta n_e}{n_0}\right| = \left(\frac{c_L\kappa'}{\omega_L\eta}\right)^2 x^2 = \left(\frac{c_L\omega_{pe0}^2}{6Lv_{th}^2 k_L\omega_L\eta}\right)^2 x^2, \tag{3.21}$$

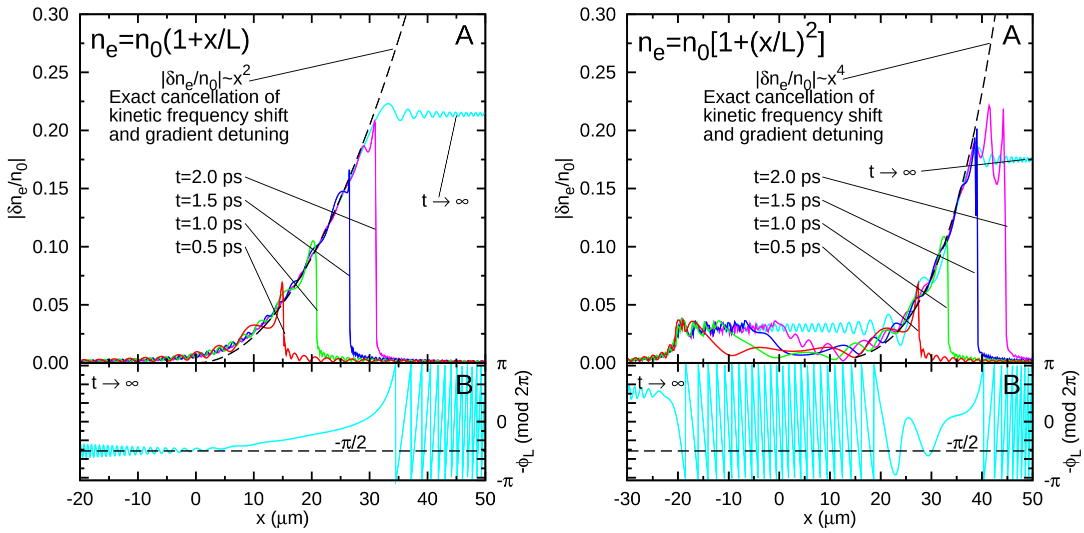

(a) (b)

Figure 3.5: (a) Envelope amplitude of the Langmuir wave in a linear profile with a prescribed driver, shown at a series of times, $t = 0.5, 1, 1.5, 2$ ps. The steady state solution ($t \to \infty$, cyan line) amplitude is also shown (upper figure) in addition to the Langmuir wave phase (lower figure). Due to phase-locking, the phase is constant at $-\pi/2$ behind the wave front where the wave is autoresonantly growing. Ahead of the wave front, the phase changes rapidly. (b) Envelope amplitude of the Langmuir wave in a parabolic profile with a prescribed driver. The steady state solution ($t \to \infty$, cyan line) amplitude is also shown (upper figure) in addition to the Langmuir wave phase (lower figure). The phase is approximately constant at $-\pi/2$ over the region of growth. Outside of this autoresonant region, the phase changes rapidly.

where ε_L, $\tilde{\eta}$, $\delta n_e/n_0$ and η are related by the expressions given in Eqs. (2.102-2.103) in the previous chapter. For the parabolic profile, we write the following similar equation:

$$(\partial_t + c_L\partial_x + ic_L\kappa'' x^2 - i\tilde{\eta}|\varepsilon_L|^{1/2})\varepsilon_L = P, \tag{3.22}$$

Defining $k_0 - k_1 - k_L = \Delta k = \kappa'' x^2/2$, we find $\kappa'' = \partial_{xx}(k_0 - k_1 - k_L) \sim (\omega_{pe0}^2/3L^2 v_{th}^2 k_L)$. In this parabolic profile case, the cancellation between the wave number detuning and the kinetic nonlinear frequency shift leads to a growth in the Langmuir wave envelope that scales with x^4, or

$$\left|\frac{\delta n_e}{n_0}\right| = \left(\frac{c_L\kappa''}{\omega_L\eta}\right)^2 x^4 = \left(\frac{c_L\omega_{pe0}^2}{3L^2 v_{th}^2 k_L\omega_L\eta}\right)^2 x^4. \tag{3.23}$$

To isolate the behaviour of autoresonance, we study Eqs. (3.20) and (3.22) in the absence of SRS by prescribing the drive of the Langmuir wave. The prescribed drive P is switched on suddenly at $t = 0$ in a plasma where $\varepsilon_L(x, t = 0) = 0$, hence $P = P_0 H(t)$, where $H(t)$ is the Heaviside step function and P_0 is a constant that describes the product of the electromagnetic (pump and seed) wave amplitudes, here constant throughout the simulation window.

In order to discuss autoresonance in the context of current ICF experiments, we choose parameters appropriate to plasma conditions at the NIF and a laser wavelength corresponding to a frequency-tripled Nd:glass laser. The solutions to Eqs. (3.20) and (3.22) are generated using identical laser parameters and plasma conditions (calculated here at $x = 0$) and differ only in density profile: $\lambda_0 = 351$ nm, $I_0 = 5 \times 10^{15}$ Wcm^{-2}, $I_1 = 1.1 \times 10^{12}$ Wcm^{-2}, $n_0 = 4.5 \times 10^{20}$ cm^{-3} ($n_e/n_c = 0.05$), $T_e = 1$ keV, $L = L_0 = 100$ μm and $\eta = 0.25$, where I_0 represents the laser beam intensity and I_1 the counter-propagating electromagnetic wave (as discussed in the following chapter, these may be assigned to, for example, laser light from the inner cone encountering counterpropagating backscattered light from the hohlraum wall due to laser light from the outer cone, or vice versa). The value of η is obtained from particle-in-cell simulations and is discussed further in the following chapter (here, $\eta = \eta_0 = 0.25$). Using these parameters, we find $k_L \lambda_D = 0.33$ and $P_0 = 3.5 \times 10^{-5}$.

The solutions to Eqs. (3.20) and (3.22) are shown in Figs. 3.5(a) and 3.5(b), respectively. Both solutions clearly exhibit phase-locking and autoresonant growth along a curve that closely matches the growth expected if the cancellation between the kinetic nonlinear frequency shift and the spatial wave number detuning arising from inhomogeneity were exact (Eqs. (3.21) and (3.23)).

The autoresonant behaviour displayed here in the kinetic regime differs strongly from the autoresonant behaviour in the fluid regime (and pendulum) earlier in the chapter:

1. Autoresonance will always begin; there is no threshold in the driver strength, regardless of the parameters chosen.
2. Autoresonance will always end. Regardless of the parameters chosen, the Langmuir wave envelope amplitude will eventually saturate, coinciding with a transition from phase-locking to rapid phase change.

In the full three-wave case, it is known that a parabolic profile may support absolute growth of the daughter waves[20]. In the parabolic case, the regime considered here has a growth rate above the threshold required for absolute growth, and autoresonance may compete with or even enhance this growth. We wish at this stage simply to show that autoresonance does not require a specific density profile and is a robust phase-locking mechanism.

3.4 A pseudoparticle model for autoresonance

We wish to understand the mechanism of the observed phase-locking in the kinetic regime and to be able to explain its key features, namely the absence of a threshold in driver strength and the finite spatial extent over which autoresonant occurs. We begin by permitting a generalised density profile of the following form:

$$n_0 = n_e(1 + \sum_1^n \frac{a_n x^n}{n}), \tag{3.24}$$

where a_n is a constant. Neglecting the derivatives of $k_{0,1}$ and assuming ω_L is constant as before, we find

$$\partial_x(-k_L) = \alpha \frac{d}{dx}\frac{n_0}{n_e} = \alpha \sum_1^n a_n x^{n-1}, \tag{3.25}$$

where $\alpha \equiv \omega_{pe0}^2/6v_{th}^2 k_L$. We thus write for the equation governing the Langmuir wave the following:

$$\left(\partial_t + c_L\partial_x + ic_L\alpha\sum_1^n a_n x^n - i\tilde{\eta}|\varepsilon_L|^{1/2}\right)\varepsilon_L = P. \tag{3.26}$$

We consider the time-stationary case and so neglect the temporal derivative. We adopt an action-angle (I, ϕ_L) formulation of the problem and accordingly make the substitutions $\varepsilon_L = |\varepsilon_L|\exp(i\phi_L)$ and $|\varepsilon_L|^2 = I$, giving, after separating real and imaginary parts,

$$\frac{dI}{dx} = \frac{2P}{c_L} I^{1/2}\cos\phi_L, \tag{3.27}$$

and

$$\frac{d\phi_L}{dx} = -\alpha\sum_1^n a_n x^n + \frac{\tilde{\eta}}{c_L} I^{1/4} - \frac{P}{c_L} I^{-1/2}\sin\phi_L. \tag{3.28}$$

This method is derived from the variational principle applied to nonlinear oscillators as developed by Witham[67]. It was applied to a broad class of nonlinear waves by Frièdland, and was shown to be applicable to multidimensional wave problems[68]. Frièdland applied the method to a variety of nonlinear phenomena including Kirchhoff vortices[69], Diocotron modes in accelerators, planetary motion, and the canonical example of the pendulum[56], and it is this action-angle approach that we take as our point of departure in modelling the behaviour of the autoresonant Langmuir wave.

During autoresonance, the phase ϕ_L should perform small oscillations around a constant average value[68]. In Figs. 3.5(a) and 3.5(b), we see that this is indeed the case and that, during phase-locking, $\phi_L \sim \pi/2$. We consider an average solution, with action $\bar{I}$ and phase $\phi_L = \pi/2$, for which the phase-locking is exact. During phase-locking, the action of the observed solution I, may be written as the sum of the average action and a small deviation σ, such that $I = \bar{I} + \sigma$. Starting from the initial point of resonance, the average action should thus grow slowly with respect to the scale on which σ varies. Since the phase should be constant along the average solution, we write

$$0 = -c_L \alpha \sum_1^n a_n x^n + \tilde{\eta} \bar{I}^{1/4} - P \bar{I}^{-1/2}. \tag{3.29}$$

Differentiating this expression, we find

$$\frac{d\bar{I}}{dx} = \frac{\alpha}{M} \sum_1^n a_n n x^{n-1}, \quad M \equiv \frac{\tilde{\eta}}{4 c_L \bar{I}^{3/4}} + \frac{P}{2 c_L \bar{I}^{3/2}}, \tag{3.30}$$

where M is a slowly-varying parameter. Expanding Eqs. (3.27) and (3.28) to lowest order around $\bar{I}$, we find for σ:

$$\frac{d\sigma}{dx} = \frac{2P}{c_L} \bar{I}^{1/2} \cos \phi_L - \frac{\alpha}{M} \sum_1^n a_n n x^{n-1}, \tag{3.31}$$

and for ϕ_L

$$\frac{d\phi_L}{dx} = \sigma M. \tag{3.32}$$

3.4.1 The pseudopotential

Eqs. (3.31) and (3.32) form a Hamiltonian system $\mathcal{H} = \mathcal{H}(\phi_L, \sigma, x)$. Taking the Hamiltonian equations

$$\frac{d\phi_L}{dx} = \frac{\partial \mathcal{H}}{\partial \sigma}, \quad \frac{d\sigma}{dx} = -\frac{\partial \mathcal{H}}{\partial \phi_L},$$

we integrate to find

$$\begin{aligned} \mathcal{H} &= \frac{M\sigma^2}{2} + \left(\frac{\alpha}{M} \sum_1^n a_n n x^{n-1} \phi_L - \frac{2P}{c_L} \bar{I}^{1/2} \sin \phi_L \right) \\ &= \frac{1}{2M} \left(\frac{d\phi_L}{dx} \right)^2 + V(\phi_L). \end{aligned} \tag{3.33}$$

Eq. (3.33) may be interpreted as a Hamiltonian that describes a pseudoparticle of effective pseudomass M, moving in a pseudopotential V. For autoresonance to occur, the pseudoparticle must remain trapped by the pseudopotential, resulting in small oscillations around a constant value of ϕ_L. For trapping to take place, we require a pseudopotential that possesses a minimum at the point of resonance. We may write V as a sum of two terms: a linear term $V_l = (\alpha \sum_1^n a_n n x^{n-1}/M)\phi_L$ and an oscillatory term $V_o = (2P/c_L)\bar{I}^{1/2}\sin\phi_L$. For a minimum in the pseudopotential to exist, the following condition must be satisfied:

$$\left|\frac{dV_o}{d\phi_L}\right|_{max} > \left|\frac{dV_l}{d\phi_L}\right|, \tag{3.34}$$

or, using the expressions for V_o and V_l,

$$\frac{2P}{c_L}\bar{I}^{1/2} > \frac{\alpha}{M}\sum_1^n a_n n x^{n-1}. \tag{3.35}$$

When this condition is satisfied, the pseudopotential takes the form of a series of wells superimposed on a linear slope. As x approaches the point of resonance $x = 0$, all terms for which $n > 1$ in Eq. (3.25) disappear. Thus, we expect the linear component of the gradient to dominate in the region close to the point of resonance.

This pseudoparticle trapping is analogous to the trapping mechanism responsible for the kinetic nonlinear frequency shift in the plasma. In the kinetic nonlinear frequency shift, particles with velocity near v_ϕ become trapped in a travelling wave and bounce back and forth in a local potential well. During autoresonance, the phase of the wave front of the Langmuir wave is trapped in a local pseudopotential, causing the phase, or pseudoparticle, to bounce back and forth and oscillate around a fixed value. This process maintains resonance beyond a single point in space, and allows the Langmuir wave envelope amplitude to grow beyond the linear response.

We are now in a position to explain the observed behaviour of the Langmuir wave. In both the fluid and kinetic regimes, we begin by considering the limit $I \to 0$ (or $\varepsilon_L \to 0$) at the resonance point from which autoresonance may begin. For the kinetic case, we see in Eq. (3.35) that as $I \to 0$, the RHS of the equation decreases faster than the LHS, i.e. the inequality becomes more easily satisfied. This means that at $x = 0$ (and $I(x = 0) \sim 0$), the system will begin in a phase-locked state. This is true for all values of a_n. Thus, assuming that the system is driven from the initial state $\varepsilon_L(x = 0) = 0$, any profile described by a polynomial with a positive gradient at $x = 0$ may undergo autoresonance in the kinetic regime.

However, as I (or ε_L) grows, the RHS of Eq. (3.35) begins to grow more quickly than the LHS. Therefore, as the Langmuir wave propagates from $x = 0$

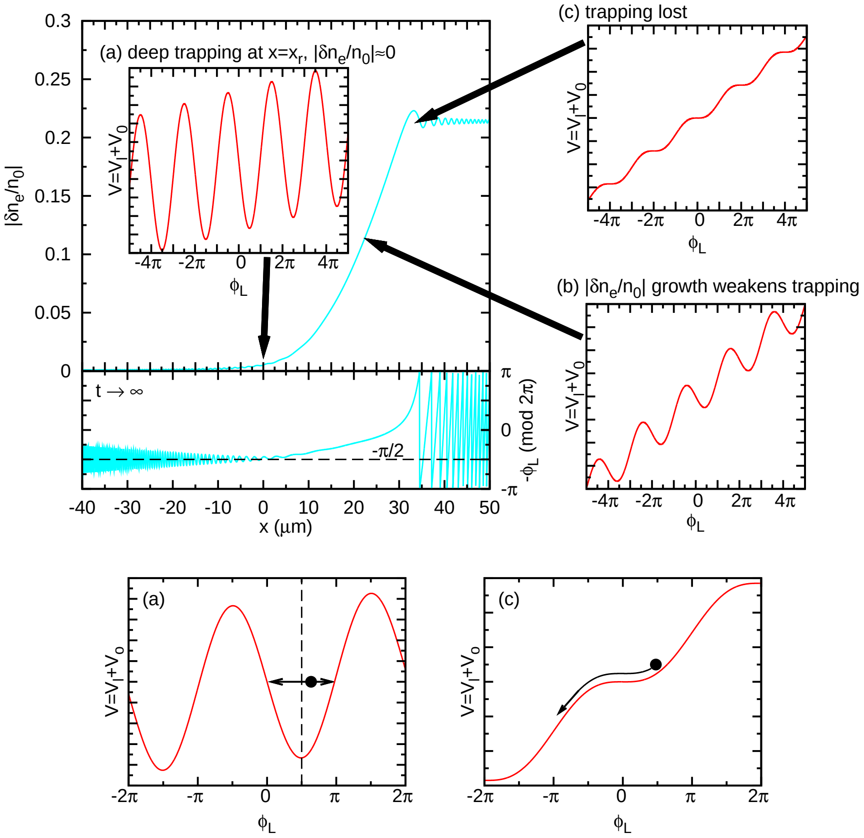

Figure 3.6: Development of the pseudopotential $V = V_l + V_o$ throughout autoresonance in a linear density profile. At (a), V is dominated by the oscillatory term V_o and the pseudoparticle describing the Langmuir wave envelope phase ϕ_L is deeply trapped, oscillating about $\phi_L = \pi/2$ (mod 2π). As the Langmuir wave propagates and grows along the parabola to (b), the linear component V_l increases more quickly than V_o and the trapping becomes weaker. At (c), the pseudopotential wells disappear. At this point, trapping is lost and the phase decreases rapidly, ending the efficient transfer of energy to the Langmuir wave and resulting in a plateau in amplitude.

and grows, the trapping of the pseudoparticle becomes progressively weaker. At the point at which

$$\left|\frac{dV_o}{d\phi_L}\right|_{max} \approx \left|\frac{dV_l}{d\phi_L}\right|, \tag{3.36}$$

the gradient of V_o is no longer sufficient to cause an oscillation in the overall sign of $dV/d\phi_L$ and the pseudopotential wells disappear. The phase ϕ_L is therefore no longer trapped and decreases rapidly, ending the efficient transfer of energy between the Langmuir wave and the driver. The Langmuir wave envelope amplitude then oscillates around a plateau, propagating with a near-constant amplitude. Each stage of this process is shown in detail in Fig. 3.6.

To a good approximation, for the parameters given earlier,

$$M = \frac{\tilde{\eta}}{4c_L\bar{I}^{3/4}} + \frac{P}{2c_L\bar{I}^{3/2}} \approx \frac{\tilde{\eta}}{4c_L\bar{I}^{3/4}}. \tag{3.37}$$

For a linear density profile ($a_1 = 1/L, a_{n\neq1} = 0$), we therefore simplify the condition given by Eq. (3.35) to the following:

$$\bar{I}^{1/4} < \frac{1}{2}\frac{\tilde{\eta}P}{\kappa' c_L^2}. \tag{3.38}$$

This equation is easily solved to find a maximum value of $\bar{I}$ (and thus $|\delta n_e/n_0|$) permissible by the condition that the pseudopotential must be able to trap the pseudoparticle (a more practical version of this equation is provided in the chapter summary). For the parameters used here, doing so gives $|\delta n_e/n_0| \approx 0.21$. This value is in close agreement with the level of the plateau in the Langmuir wave envelope amplitude observed in Fig. 3.6 (in this figure, the plateau is reached at $|\delta n_e/n_0| \approx 0.22$).

While autoresonance may arise for any values of the parameters $\tilde{\eta}$, κ' and P, both the spatial extent over which autoresonance will be maintained and the eventual saturation amplitude of the Langmuir wave are sensitive to the parameters chosen: Increasing κ' (i.e. steepening the density gradient) will steepen the gradient of the parabola along which the Langmuir wave grows, but will also reduce the final saturation amplitude; decreasing $\tilde{\eta}$ will steepen the parabola while again reducing the saturation amplitude; and increasing P will increase the saturation amplitude while leaving the gradient of the parabola unchanged.

The absence of a threshold in driver strength and the loss of autoresonance at high Langmuir wave envelope amplitude are both phenomena that are not present in the case where fluid effects provide the dominant frequency shift discussed earlier in the chapter and by Yaakobi *et al.* in Ref.[38]. A derivation of the threshold in this case is given in Ref.[56], and is simply obtained by following the pseudoparticle treatment of the Langmuir wave phase above with a fluid-type nonlinear frequency shift in place of the kinetic-type term used here. However, the difference in the autoresonant behaviour in the kinetic and fluid regimes may be intuitively understood. In the fluid case, close to the resonance point, the spatial growth gradient of the Langmuir wave is at a maximum: If the fluid nonlinear frequency shift exactly cancels the wave number detuning due to inhomogeneity, then $\varepsilon_L \sim x^{1/2}$ and $\partial_x\varepsilon_L \sim x^{-1/2}$. Thus, in the fluid case, the Langmuir wave must adapt to the density profile most quickly near the point of resonance. If the Langmuir wave is driven sufficiently strongly to do so, the system will enter autoresonance. As the Langmuir wave grows, the rate of change in amplitude required to maintain resonance decreases, and the system remains autoresonant until pump depletion or other effects dominate.

In the kinetic case, close to the resonance point, the spatial growth gradient of the Langmuir wave is at a *minimum*: If the kinetic nonlinear frequency shift exactly cancels the wave number detuning due to inhomogeneity, $\varepsilon_L \sim x^2$ and $\partial_x\varepsilon_L \sim x$. At resonance, this gradient is therefore at a minimum, and increases as the Langmuir wave propagates. The Langmuir wave envelope amplitude then grows until it is unable to adapt its amplitude rapidly enough to maintain the cancellation of the wave number detuning, and resonance is lost.

3.4.2 Driver threshold in the fluid regime and generalisation of the frequency shift

For completeness, we may we define a nonlinear frequency shift of general form such that

$$(\partial_t + c_L\partial_x + ic_L\alpha\sum_1^n a_n x^n + i\xi|\varepsilon_L|^m)\varepsilon_L = P. \tag{3.39}$$

In the kinetic regime, $\xi = -\tilde{\eta}$, $m = 1/2$, while in the fluid regime, $\xi = \beta$, $m = 2$. The pseudoparticle mass is now generalised to the form

$$M = \frac{m\xi\bar{I}^{m/2-1}}{2c_L} + \frac{P}{2c_L\bar{I}^{3/2}} \tag{3.40}$$

The pseudopotential will be of a similar form to Eq. (3.34), but care must be taken when finding the point at which the Langmuir wave is resonant with the drive (for example, in the fluid regime, resonance is found at $\phi_L = -\pi/2$ rather than $\phi_L = \pi/2$ in the kinetic regime, changing the sign of the driver).

We begin at the resonance point, where $\bar{I} \approx 0$. Regardless of the form of the nonlinearity (i.e. for all values of $m > 0$ and ξ, including the absence of a nonlinearity), as $\bar{I} \to 0$, the second term on the RHS of Eq. 3.40 is dominant, Eq. (3.34) is satisfied and there will be resonance. For $0 < m < 2$, as $\bar{I}$ grows, the RHS of Eq. (3.34) tends towards a growth rate that is higher than that of the LHS of Eq. (3.34). Thus, a loss of autoresonance is unavoidable. Physically, however, the value of $\bar{I}$ must remain less than 1, thus the limit on the saturation amplitude of the Langmuir wave may come from other sources (pump depletion, wave breaking etc . . .). For $m \geqslant 2$, there is a threshold, representing the point at which Eq. (3.34) is most difficult to satisfy. Provided that Eq. (3.34) is satisfied at this critical point, autoresonance will be maintained to arbitrarily high values of $\bar{I}$.

For $m = 2$, M tends towards a constant value. The threshold in this case can be easily calculated in order to give the threshold driver strength required to produce autoresonance, relevant to both the pendulum and the Langmuir wave in the fluid regime: Setting $\xi = \beta$, $m = 2$, $a_1 = -1/L$, $a_{n\neq 1} = 0$, it is clear that there is a value $\bar{I}_c$ at which Eq. (3.34) is hardest to satisfy. In the fluid regime,

$$M = \frac{\beta}{c_L} + \frac{P}{2c_L \bar{I}^{3/2}}, \tag{3.41}$$

where we note that the first term is now independent of $\bar{I}$. By differentiating $M\bar{I}^{1/2}$ and looking for the turning point, we find

$$\bar{I}_c = \left(\frac{P}{\beta}\right)^{2/3}, \tag{3.42}$$

giving, by substitution into Eq. (3.34), a critical driver strength P_c of the form

$$P_c = \frac{c_L^{3/2}}{\beta^{1/2}} \left(\frac{\kappa'}{3}\right)^{3/4}. \tag{3.43}$$

Thus, autoresonance is assured provided that $P > P_c$. In the case that $\kappa', \beta, c_L = 1$, the system is normalised to Eq. 3.14, and $P_c = (1/3)^{3/4} = 0.44$, in agreement with Ref.[38]. For the values given in Sec. 3.2, $P_c = 1.6 \times 10^{-5}$. From simulations, we find $P_c \approx 1.2 \times 10^{-5}$. While reasonably accurate, the pseudoparticle model outlined above is generally observed to overestimate P_c. This overestimation has two likely causes: The model involves a series of approximations, such as the smallness of the amplitude near resonance. In reality, the linear response of the oscillator means that this approximation is somewhat violated. Furthermore, the oscillator may still grow in amplitude just after the potential wells have disappeared, but before the gradient of the pseudopotential becomes very steep.

In the kinetic regime, where $\delta\omega = \tilde{\eta}|\varepsilon_L|^{1/2}$, there may be small fluctuations in the dependence of $\delta\omega$ on ε_L. The analysis above provides assurance that a perturbation in m away from $m = 1/2$, where $\delta\omega = \tilde{\eta}|\varepsilon_L|^m$, will not greatly alter the behaviour of the autoresonant Langmuir wave. Thus, autoresonance is robust to small variations in both the density gradient and the dependence of the frequency shift on the Langmuir wave amplitude.

3.4.3 Damping in autoresonance in the kinetic regime

We consider now a damping υ of the Langmuir wave. This term is introduced to Eq. (3.17) to give the following:

$$(\partial_t + c_L\partial_x + ic_L\kappa' x - i\tilde{\eta}|\varepsilon_L|^{1/2} + \upsilon)\varepsilon_L = P. \tag{3.44}$$

In Fig. 3.7, the impact of a fixed damping on the saturation amplitude of the autoresonant Langmuir wave envelope amplitude is shown, for both linear and parabolic profiles. While reducing the saturation amplitude of the Langmuir wave, the presence of damping does not alter the curve along which the autoresonant wave front grows. In the following chapter, the prescribed drive P is replaced by full three-wave coupling. In this case, both daughter waves may grow, leading to the enhancement of the local value of P that drives the Langmuir wave. This strengthening of the local ponderomotive drive suggests that the effect of damping is even less than that shown in Fig. 3.7, and that weak damping is not likely to prevent autoresonance in the kinetic regime.

In the regime considered here, Landau damping is initially the principle source of attenuation of the Langmuir wave. As discussed in the previous chapter, this damping is not constant in time: as electron trapping effects increase, the damping of the Langmuir wave by resonant particles is quickly reduced, resulting in a negligible residual damping after a few bounce periods of the trapped electrons. In Fig. 3.8, the impact of this type of damping on the growth of the autoresonant Langmuir wave is shown. Starting from the linear value of the Landau damping ν_L, the Landau damping is decreased in time in a prescribed fashion. Despite the initial damping, the saturation amplitude of the Langmuir wave is unchanged.

Figs. 3.7 and 3.8 demonstrate the robustness of the phase-locking between the Langmuir wave and the drive in the presence of damping. This result allows one to expect a growth that closely follows the curve suggested by an exact cancellation of the kinetic frequency shift and the wave number detuning due to inhomogeneity, even in an environment where the damping of the Langmuir wave is not constant. Thus, the autoresonant growth rate should be independent of the damping, and if the drive P is sufficient to allow autoresonance in the presence of the damping, the growth rate is also independent of P. Finally, the saturation amplitude of the autoresonant Langmuir wave envelope is unaffected by the presence of Landau damping, provided that the Landau damping is reduced in time (artificially or as a result of the growth of the Langmuir wave).

3.4.4 The parameter space and growth rate of autoresonance in the kinetic regime

In Sec. 3.2.2, it was shown that the equation describing the evolution of the Langmuir wave in the fluid regime could be normalised in such a way that there was only a single free parameter. This may also be done in the kinetic regime: By making the substitutions $\zeta = \sqrt{|\kappa'|}x$, $\tau = c_L\sqrt{|\kappa'|}t$ and $\tilde{\eta}\varepsilon_L^{1/2} = c_L\sqrt{|\kappa'|}Y^{1/2}$, the equation describing the evolution of the Langmuir wave through a linear density

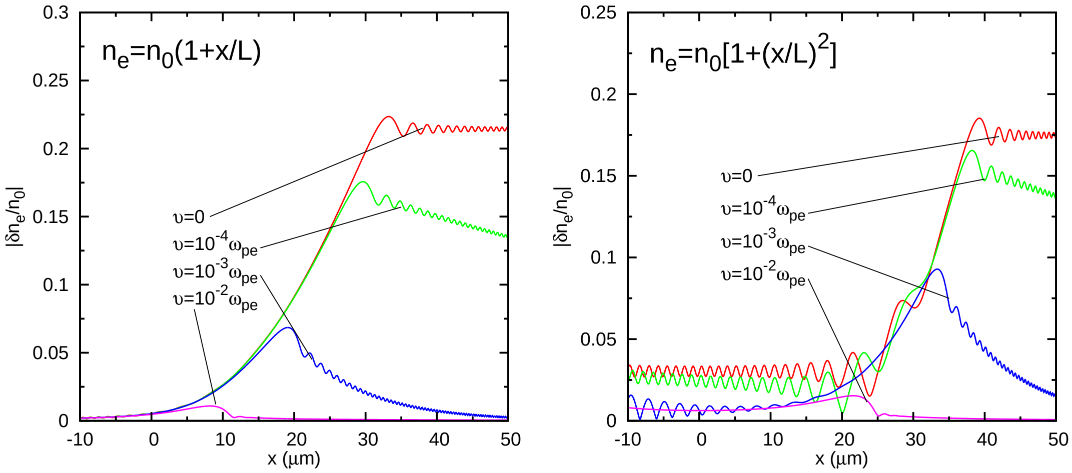

(a) (b)

Figure 3.7: Impact of a fixed damping on the saturation amplitude of the autoresonant Langmuir wave envelope, shown for both (a) linear and (b) parabolic profiles. The curve along which the autoresonant wave front amplitude grows is unchanged by the strength of damping.

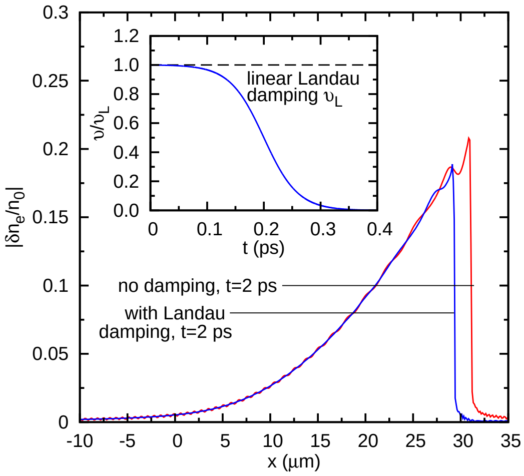

Figure 3.8: (Color online) Impact of a prescribed Landau damping on the growth of the autoresonant Langmuir wave envelope amplitude. If the damping is switched off, the saturation amplitude of the Langmuir wave is unchanged from the undamped case.

profile in the kinetic regime,

$$\left(\partial_t + c_L\partial_x + ic_L\kappa' x - i\tilde{\eta}|\varepsilon_L|^{1/2}\right)\varepsilon_L = P, \tag{3.45}$$

may be normalised to the following:

$$\left(\partial_\tau + \partial_\zeta + i\zeta - i|Y|^{1/2}\right)Y = \Upsilon, \tag{3.46}$$

where $\Upsilon = (\tilde{\eta}^2/c_L^3\kappa'^{3/2})P$. Solutions to the steady-state equation,

$$\left(\frac{d}{d\zeta} + i\zeta - i|Y|^{1/2}\right)Y = \Upsilon, \tag{3.47}$$

all show growth along the parabola simply given by $Y = \zeta^2$ and differ only in the level at which saturation in Y is reached. Varying the driver strength P (and hence Υ) changes the saturation level according to the Eq. (3.38), which after normalisation may be written simply as $Y < \Upsilon^2/4$. Varying L, however, changes both the value of Υ and how Y and ε_L are related. When considering the impact of changing the gradient of the plasma, it is therefore more instructive to retain the form of the equation governing the evolution of the Langmuir wave before normalisation to a single parameter. Solutions to the steady-state of Eq. (3.45) are shown in Fig. 3.9, with varying values of P, η and L. In each figure (left, centre and right), the solid red line shows the solution obtained using reference values of $P = P_0$, $\eta = \eta_0$ and $L = L_0$ (defined in Sec. 3.3). In Fig. 3.9, all parameters take these reference values unless explicitly stated otherwise. It can be seen that the approximate condition for the saturation of autoresonance given in Eq. (3.38) is valid here; increasing P_0 by a factor of 1.25 results in an increase in saturation amplitude of $1.25^2 \sim 1.5$.

It has been demonstrated in Sec. 3.4.1 that autoresonance in the kinetic regime may occur for any choice of the parameters P, η and κ. The question is not therefore whether autoresonance may arise, but whether it will give rise to a significant growth in the Langmuir wave sufficiently quickly that it is not dominated by other growth processes.

Assuming the Langmuir wave propagates at c_L, the growth rate of the maximum of the autoresonant wave front in a linear profile should be given by

$$\frac{d}{dt}\left|\frac{\delta n_e}{n_0}\right|_{max} = \frac{d}{dt}\left(\frac{c_L}{\omega_L\eta}\alpha\sum_1^n a_n(c_Lt)^n\right)^2, \tag{3.48}$$

or, for a linear density profile,

$$\frac{d}{dt}\left|\frac{\delta n_e}{n_0}\right|_{max} = 2\left(\frac{c_L^2\kappa'}{\omega_L\eta}\right)^2 t. \tag{3.49}$$

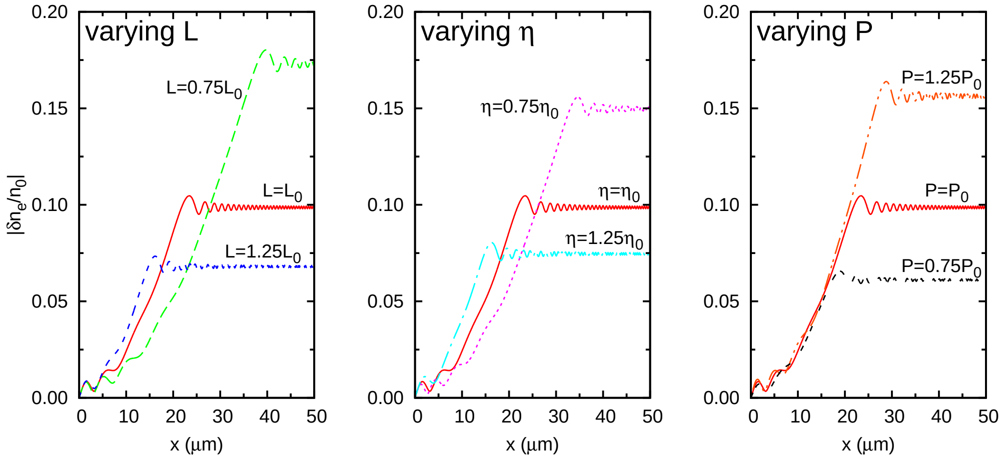

Figure 3.9: Steady-state solutions to Eqs. (3.45), showing the spatial growth and saturation of the autoresonant Langmuir wave. In each figure [(a), (b) and (c)], the solution depicted by the solid red line is obtained using reference values $P = P_0$, $L = L_0$ and $\eta = \eta_0$. All other solutions are calculated using parameters that are unchanged but for that which is explicitly stated.

Thus we see that the growth rate is zero initially but increases rapidly with time.

As discussed in the previous chapter, in the full three-wave coupling case, a linear profile will not support absolute growth of the daughter waves in the absence of kinetic (or other non-linear) effects, giving rise only to a stable convective growth. It will be shown in the following chapter that, for the ICF-relevant parameters used here, autoresonance in a linear profile is the dominant process in the determination of the Langmuir wave envelope amplitude. However, as discussed in Sec. 2.4.1.2, a parabolic profile may support absolute growth in the absence of kinetic effects, provided that the damping of the daughter waves is sufficiently small (or the laser sufficiently intense). In the absence of kinetic effects and damping, for the parameters given here, the growth rate is above the threshold required for absolute growth. Although the Langmuir wave here grows under a fixed-amplitude driver (i.e. the scattered wave is not amplified), a similar threshold is observed in Fig. 3.7b, where the linear response varies greatly with the damping (this is not the case in Fig. 3.7a, where the density profile is linear). The question is then whether the autoresonant growth rate is greater than or inferior to the absolute growth rate. Initially, the growth rate due to autoresonance is zero, but this rate increases quickly (particularly true for parabolic profiles).

For fusion-relevant parameters, it is not clear by simply comparing these growth rates whether the growth will be absolute or not, since kinetic effects may stabilise a growth that would otherwise be absolute. It seems likely that a purely parabolic profile that has a growth rate γ_0 far above the threshold for absolute growth ($\gamma_0 \gg \gamma_{min}^{abs}, \gamma_{inh}$, defined in Sec. 2.4.1.2) will support a growth that is dominated by the absolute growth rate rather than the autoresonant growth rate. However, the presence of damping may stabilise the absolute growth while still allowing a significant autoresonant growth, or kinetic effects may indeed be strong enough to stabilise the growth. Three-wave coupling simulations of growth in parabolic density profiles are presented in the next chapter.

3.5 Chapter summary

From the results of this chapter, it is clear that a driven nonlinear oscillator provides a suitable description of the behaviour of the prescriptively driven Langmuir wave. When the Langmuir wave is subject to a nonlinear frequency shift, under appropriate conditions, it may phase-lock to a driver that is swept in wave number as a function of space (or, as in the case of the pendulum, swept in frequency as a function of time), permitting an efficient exchange of energy between oscillator and driver and a growth in amplitude beyond the linear average value.

It was shown that autoresonance is possible for a broad class of nonlinear oscillators. In the kinetic regime ($k_L\lambda_D \gtrsim 0.25$), where the nonlinear frequency shift is proportional to the square root of the amplitude of the Langmuir wave envelope, it was shown that autoresonance is always possible (i.e. there is no threshold in the strength of the driver), provided that the gradient of the density profile is positive. Furthermore, it was observed in simulations and explained analytically that autoresonance will be lost for sufficiently high Langmuir wave amplitudes, but that these amplitudes may be so high that other saturation mechanisms, such as wave-breaking or depletion of the pump wave, will be the determining factor in saturating the Langmuir wave amplitude. In a linear density profile that increases in the direction in which the Langmuir wave propagates, the exact cancellation of the kinetic nonlinear frequency shift and the wave number detuning due to inhomogeneity results in a growth in the Langmuir wave amplitude that follows a parabola:

$$\left|\frac{\delta n_e}{n_0}\right| = \left(\frac{c_L\kappa'}{\omega_L\eta}\right)^2 x^2. \tag{3.50}$$

The maximum Langmuir wave amplitude that may be reached via autoresonance before phase-locking is lost is given by the following:

$$\left|\frac{\delta n_e}{n_0}\right|_{max} = \frac{k_L\epsilon_0}{n_0 e}\left(\frac{1}{2}\frac{\omega_L\eta P}{\kappa' c_L^2}\right)^2. \tag{3.51}$$

While damping may reduce the saturation amplitude of the autoresonant growth, the form of the parabola along which the Langmuir wave grows is unchanged from that defined above. For parameters relevant to ICF, a nonlinear Landau-type damping that is reduced in time does not affect the saturation amplitude.

Since the autoresonant growth rate is dependent on the group velocity of the Langmuir wave (and hence k_L), autoresonant BSRS is likely to be of much greater importance than FSRS. With regards to autoresonance in the regime dominated by fluid effects ($k_L\lambda_D \lesssim 0.15$), the timescales over which the autoresonant Langmuir wave growth might achieve a significant amplitude are likely to be too long to be of relevance to the NIF. In contrast, autoresonance in the kinetic regime displays a fast, important growth over timescales that suggest autoresonance may provide a significant mechanism for the enhancement of Langmuir wave amplitudes (and hence scattered light).

The results of this chapter provide motivation for further study of autoresonance in the kinetic regime. While it is clear that autoresonance is possible under the action of a fixed driver, it must now be shown that autoresonance may arise in three-wave coupling, where the amplitudes of the electromagnetic waves are not fixed.

Chapter 4

Autoresonance in three-wave interactions

It was shown in the previous chapter that autoresonance is possible in the kinetic regime when the Langmuir wave is driven by a prescribed (constant) ponderomotive force. We wish now to show that these results apply equally to full three-wave coupling. To this end, a three-wave fluid code was written to solve simultaneously the equations governing the evolution of the EM waves and the Langmuir wave.

We begin the chapter by seeding the three-wave system with a single frequency at a level that is consistent with the level of thermal noise expected in the plasma. In this situation, both SRS and autoresonance are possible only at a single point in the plasma. Later, we examine the effect of a broad-band seed, closer to that which would be present in experiments, on the growth of the Langmuir wave. This seed, if sufficiently broad in frequency, will allow SRS and autoresonance to begin at every point in the plasma.

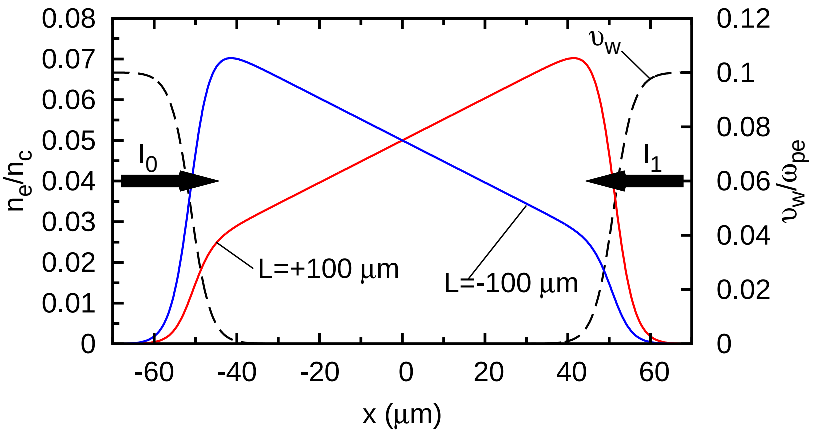

Figure 4.1: Linear density profile of the plasma used in three-wave coupling simulations. The red and blue lines give the density profiles for the autoresonant and non-autoresonant cases, respectively, while the black dashed line shows the damping ν_w that was applied to the edges of the simulation window to prevent Langmuir wave propagation into the vacuum.

4.1 Solving the three-wave equations

We solve the following three-wave system of equations derived in Chapter 2, relevant to SRS in warm plasmas with a linear density profile in the kinetic regime:

$$\mathcal{L}_0 A_0 = -\frac{e}{4m_e}\frac{k_L}{\omega_0}\varepsilon_L A_1, \tag{4.1}$$

$$\mathcal{L}_1 A_1 = \frac{e}{4m_e}\frac{k_L}{\omega_1}\varepsilon_L^* A_0, \tag{4.2}$$

$$\left(\mathcal{L}_L + ic_L\kappa' x - i\tilde{\eta}|\varepsilon_L|^{1/2}\right)\varepsilon_L = \frac{e}{4m_e}\frac{k_L}{\omega_L}\omega_{pe}^2 A_1^* A_0. \tag{4.3}$$

The finite difference scheme used to solve these equations is given in detail in Appendix 6.2. In brief, the three waves are integrated using an adaptation of the method developed by Crank and Nicholson[70], combining both forward and backward Euler schemes. To minimise numeric damping, the EM waves and Langmuir wave were integrated using different spatial meshes, each tailored to the specific group velocity of the waves. The coupling terms on the RHS of Eqs. (4.1-4.3) were then calculated using interpolation between the different spatial meshes.

The parameters with which the three-wave equations were solved were again chosen so as to be relevant to the NIF. A linear density profile was chosen for clarity in determining autoresonance and reducing possible complications arising from absolute growth, contained within a simulation window of LHS and RHS boundaries $[x_L, x_R]$. The plasma was chosen to be of length 100 μm, with 10 μm vacuum spaces at each boundary, with the three waves resonant in the centre of the plasma at $x = x_{res} = 0$. This length corresponds to the approximate expected size of a "hot-spot" in laser intensity, defined in Sec. 1.5.1.1. A pump with intensity I_0 was injected at x_L, while a seed of intensity I_1 was injected at x_R. An artificial damping ν_w was applied to the edges of the simulation window in order to contain the Langmuir wave (i.e. to prevent it propagating into the vacuum). The plasma profile (both positive and negative density gradients) and damping window used to prevent the propagation of the Langmuir wave into the vacuum are shown in Fig. 4.1.

The parameters used to solve Eqs. (4.1-4.3) were the following: $\lambda_0 = 351$ nm, $I_0 = 5 \times 10^{15}$ Wcm^{-2}, $I_1 = 5 \times 10^{9}$ Wcm^{-2}, $n_0 = 4.5 \times 10^{20}$ cm^{-3} ($n_e/n_c = 0.05$), $T_e = 1$ keV, $L = \pm 100$ μm and $\eta = 0.25$ (or $\eta = 0$), giving $k_L\lambda_D = 0.33$. All parameters were calculated at $x = x_{res} = 0$ and all were taken to be constant, although the variation in the wave coupling strength, due to the inhomogeneous density profile, on the RHS of Eq. 4.3 was included. The solutions to Eqs. (4.1-4.3) under these conditions are shown in Figs. 4.3, 4.2 and 4.4.

In Fig. 4.3, the plasma reflectivity (left) and the Langmuir wave amplitude (right) are shown. In both the left and right figures, the autoresonant case ($L = +100$ μm, green line), the non-autoresonant case ($L = -100$ μm, blue line) and the Rosenbluth saturation case ($L = +100$ μm, $\eta = 0$, red line) are given. The reflectivity R is calculated by measuring the intensity of the reflected pump wave (or, equivalently, the amplified seed) at x_L.

4.1.0.1 Rosenbluth saturation in three-wave coupling simulations

In the Rosenbluth saturation case, defined in Chapter 2, kinetic effects are neglected and the RHS seed is amplified by a factor of $\exp(G_R)$ (or $\exp(2G_R)$ in intensity) as it passes through x_{res}, where $G_R = 1.26$ and the amplification takes place over the length defined approximately by the turning points $x_t = x_{res} \pm 2.7$ μm, calculated using Eq. (2.82). The agreement between the analytic result and the numerical solution, shown in Fig. 4.3 (left, red line), demonstrate that the level of numeric damping and general inaccuracy of the integration scheme are both low (the value of saturation is in agreement with the analytic result to 4 significant figures). An estimation of the time taken for the reflected light to reach saturation after the pump wave has reached the resonance point t_{sat} is given by Eq. (2.80). For the parameters used here, $t_{sat} = 0.06$ ps.

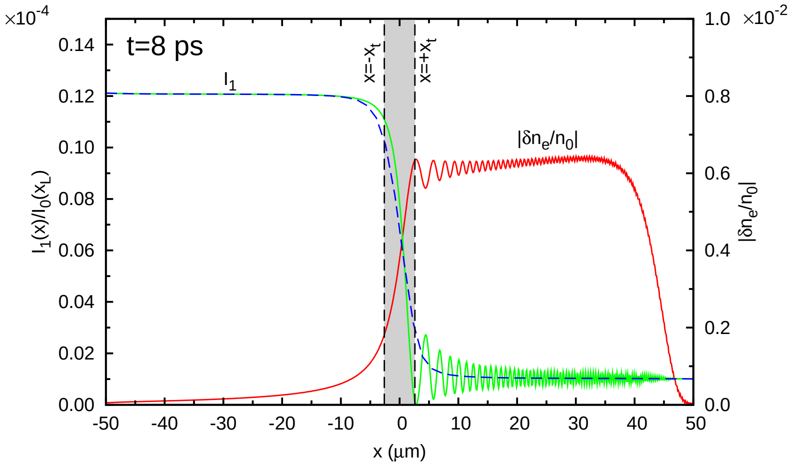

Figure 4.2: Rosenbluth saturation observed in three-wave coupling simulations after the system has reached a steady state. (Green solid line) The seed injected at x_R undergoing amplification. (Blue dashed line) The seed strength after spatial averaging. (Red solid line) The amplitude of the Langmuir wave envelope. The turning points are shown at $x = \pm x_t$, where by calculation $x_t = 2.6$ μm. The grey region is the approximate spatial extent over which amplification occurs. The pump is essentially constant across the window.

The pump wave requires approximately 0.26 ps to reach the resonance point after being injected at x_L, and the scattered wave requires a similar time to propagate from the resonance point to x_L, thus we expect saturation of the reflected light as measured at x_L to occur at approximately 0.6 ps, in agreement with Fig. 4.3 (left, red line). In Fig. 4.2, a solution is given at $t = 8$ ps, well after saturation of the reflected light. At this time, the Langmuir wave has propagated from its point of origin $x \sim 0$ to the edge of the plasma, where it is subsequently damped. In this figure, the location of the turning points is shown, clearly identifying the region over which growth occurs in the case where $\eta = 0$.

4.1.0.2 The impact of kinetic effects on three-wave coupling simulations at low seed strengths

In Fig. 4.3, solutions to the autoresonant case ($L = +100$ μm, green line), the non-autoresonant case ($L = -100$ μm, blue line) are shown. In the case where the gradient is of an incorrect sign to produce autoresonance ($L = -100$ μm), it is observed with these parameters that not only is no autoresonant growth possible, but that the response of the Langmuir wave to the EM waves is lower than the case where there is no kinetic nonlinear frequency shift. This is simply explained:

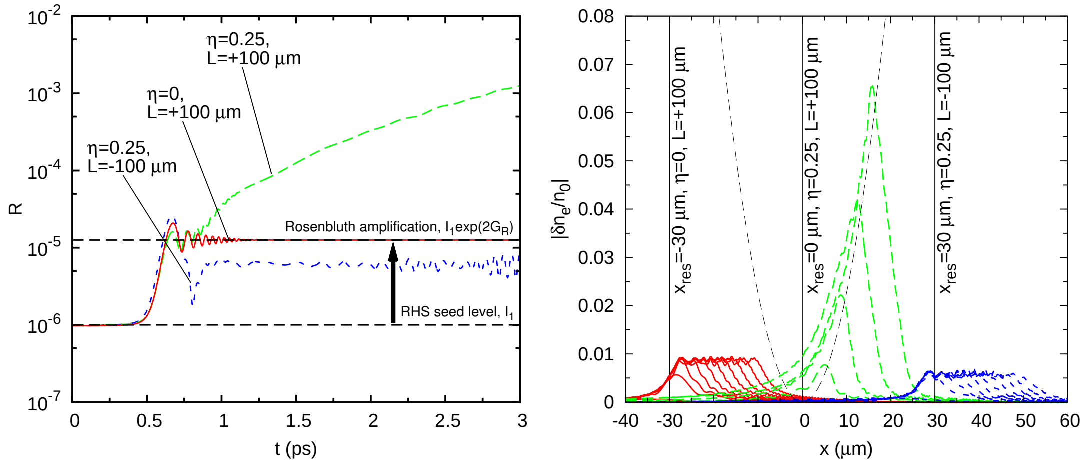

Figure 4.3: (Left) BSRS reflectivity of the plasma taken from solutions to the three-wave equations. In the case $\eta = 0$, Rosenbluth gain saturation limits the growth of the daughter waves, quickly saturating the reflectivity (the sign of L does not change the result in this case). In the autoresonant case $\eta = 0.25$, $L = +100\ \mu$m, there is a cancellation between the kinetic nonlinear frequency shift and the wave number detuning due to inhomogeneity, leading to a growth in Langmuir wave amplitude well above the Rosenbluth result. In the case $\eta = 0.25$, $L = -100\ \mu$m, autoresonance is not possible and the kinetic nonlinear frequency shift enhances the effect of the wave number detuning, in this case saturating the daughter waves at a level below the Rosenbluth result. (Right) Langmuir wave envelope amplitude at a series of times ($\Delta t = 0.5$ ps), taken from solutions to the three-wave equations. The parabola (black dashed line) plots the Langmuir wave envelope amplitude corresponding to an exact cancellation between the two shifts. Other than those stated, the parameters are identical in each case and are calculated at $x = 0$. The three cases have been spatially offset for clarity.

The initial growth of the Langmuir wave is at x_{res}, unchanged from the growth in the absence of kinetic effects. However, as the Langmuir wave grows, so too does the frequency shift due to kinetic effects. Cancellation between the kinetic nonlinear frequency shift and the wave number detuning due to inhomogeneity is still possible, but it is now *behind* the point of initial resonance in the negative density profile and travels in the *negative* x-direction as the Langmuir wave (and frequency shift) grows. Since the Langmuir wave propagates in the positive x-direction, autoresonance is not possible. As a result of this process, the region in space over which the Langmuir wave is resonant with the EM waves is reduced compared to the case where kinetic effects are suppressed, and consequently there is an overall reduction in the growth of the daughter waves.

In the case where the gradient is of the correct sign to produce autoresonance ($L = +100\ \mu$m), we see that both daughter waves grow well beyond the values observed during Rosenbluth saturation. Thus, we see that autoresonance is an effective mechanism for increasing the reflectivity of the plasma, and is by no means limited to being driven in a prescribed fashion. In Fig. 4.4, the Langmuir wave envelope amplitude and three-wave phase difference are shown at a series of times. Instead of merely the Langmuir wave phase being constant as in the prescribed driver case discussed in the previous chapter, it is the envelope phase difference $\phi = \phi_0 - \phi_1 - \phi_L \approx \pi/2$ that must remain constant during autoresonance. The phases are calculated by taking the argument of the complex envelope amplitude of the three waves and unwrapping it over 2π to reconstruct the full behaviour of the phase. The phase-locked region is observed to propagate at the same velocity as the autoresonant wave front, extending in space as the wave front propagates away from the initial point of resonance. These results show a remarkable agreement with prescribed driver simulations, indicating that autoresonance under these conditions is the dominant growth mechanism and is the principle factor in determining the behaviour of both of the daughter waves.

These results are applicable to the seed and pump strengths used here, where the seed intensity is of the order of thermal noise that we expect in the plasma. If the pump (or seed) is increased significantly in intensity, the solution may eventually become destabilised. This is discussed further later in the chapter.

4.1.1 The effect of pump strength

In Fig. 4.5, the reflectivity R of the plasma obtained by solving the three-wave equations is shown for a range of pump intensities (1.25×10^{15}, 2.5×10^{15}, 5×10^{15}, 1×10^{16} and 2×10^{16} Wcm^{-2}). The seed was introduced as before at $x = x_R$, the RHS boundary of the simulation window, with intensity $I_1/I_0 = 1\times10^{-6}$. The plasma conditions and profile were identical in each case to those given in Sec. 4.1.

In each case, the initial fast growth and subsequent plateau (although short-lived at higher pump intensities) is described by Rosenbluth saturation[20]: In the absence of kinetic effects or pump depletion, the seed saturates at $I_1(x = x_L) = I_1(x = x_R)\exp(2G_R)$, for which G_R is proportional to the pump intensity, as described by Eq. (2.79). In Chapter 3, it was shown that the curve along which the Langmuir wave grows is independent of the strength of the ponderomotive drive (and thus laser intensity). However, it was also shown that the level at which growth saturates is highly dependent of the strength of the ponderomotive drive. For pump intensities of 5×10^{15} Wcm^{-2} and weaker, the Langmuir wave solution is essentially completely determined by autoresonance. The wave evolves

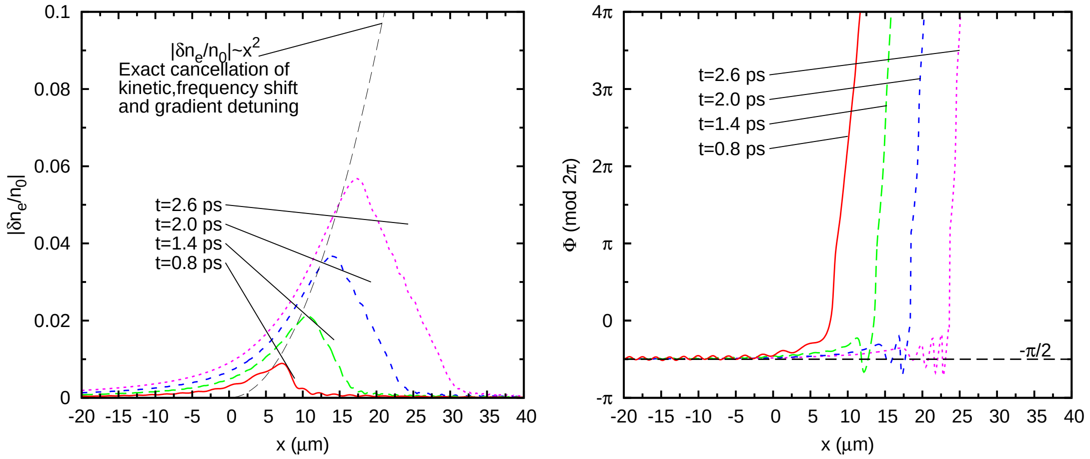

Figure 4.4: (Left) Solution to the three-wave equations showing the autoresonant Langmuir wave envelope amplitude at a series of times, $t = 0.8,\ 1.4,\ 2.0,\ 2.6$ ps. The single-frequency seed $I_1/I_0 = 1 \times 10^{-6}$ ($I_0 = 5 \times 10^{15}\mathrm{Wcm}^{-2}$) in this case is relatively weak, approximately at the level of thermal noise. (Right) The phase difference between the three wave envelopes. Phase locking occurs at $-\pi/2$, modulo 2π.

in a predictable fashion, growing in amplitude as it propagates. The cancellation between the wave number shift due to inhomogeneity and the kinetic nonlinear frequency shift is almost exact, leading to a parabolic growth in Langmuir wave envelope amplitude, as defined in Eq. (3.21). As predicted, the autoresonant growth is greater (and saturates later in time) with increasing pump strength.

For pump intensities of over 5×10^{15} Wcm^{-2}, the situation is more complex. For $I_0 = 1 \times 10^{16}$ Wcm^{-2}, shown in Fig. 4.6, the solution is autoresonant until $t \sim 1.5$ ps. Up to this time, the Langmuir wave is strongly phase-locked and the behaviour of the Langmuir wave is predictable. Shortly after 1.5 ps, the autoresonant solution becomes unstable behind the wave front, and behaves for a period of time in an absolutely unstable fashion. At later times, the growth of the Langmuir wave becomes saturated by the depletion of the pump wave, and the solution is chaotic and maintains a reflectivity close to $R = 1$, i.e. nearly all pump energy is reflected. For $I_0 = 2 \times 10^{16}$ Wcm^{-2}, the situation is similar, but absolute growth and the subsequent saturation is achieved more quickly. By reducing the seed strength, the transition from autoresonant behaviour to absolute growth may be delayed, but the behaviour of the reflectivity is not significantly altered (This is the valid unless the seed strength is reduced so much that there is no significant autoresonant growth. In this case, Rosenbluth saturation is observed

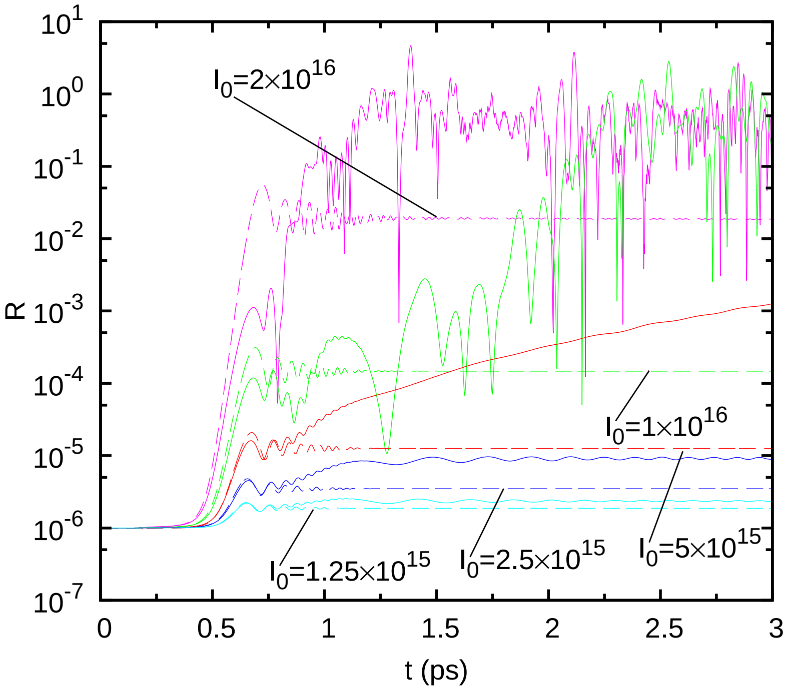

Figure 4.5: Reflectivity of the plasma under a range of pump intensities, taken from solutions to the three-wave equations. The solid lines represent the solutions obtained when kinetic effects are included ($\eta = 0.25$), while the dashed lines show Rosenbluth saturation, obtained when kinetic effects are neglected ($\eta = 0$). Pump strengths of $I_0 = 1 \times 10^{16}$Wcm^{-2} and above display autoresonant behaviour for a limited duration before an absolute growth dominates the evolution of the daughter waves.

and the solution is stable.).

These findings are summarised in Fig. 4.7, where the gain of the plasma (equal to $(1/2)\log(R/I_1)$) is plotted as a function of the Rosenbluth gain factor G_R. The reflectivity shown is the value at saturation. In the case of gains of 1.26 and below (here equivalent to powers of 5×10^{15} Wcm^{-2} and below), the saturation of the reflectivity is a result of the loss of autoresonance due to the growth of the Langmuir wave causing a dephasing from the drive, as discussed in the previous chapter. In Fig. 4.7, gains above 1.26 are annotated with a pair of numbers in brackets. The first number in this pair is the time up to which the behaviour of the Langmuir wave is determined by autoresonance, or the time at which absolute growth of the Langmuir wave begins. The second number is the time at which the reflectivity reaches saturation due to the depletion of the

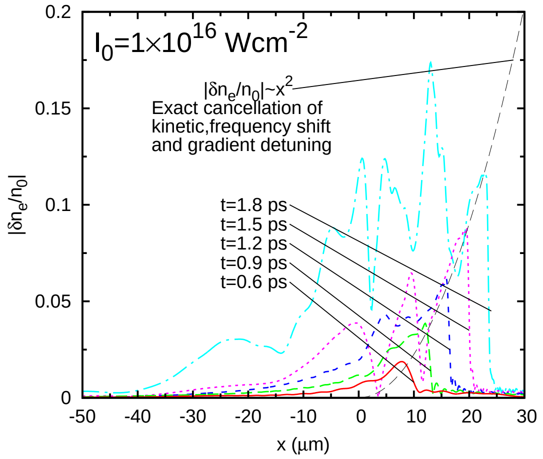

Figure 4.6: Solution to the three-wave equations showing the Langmuir wave amplitude at a series of times, $t = 0.6,\ 0.9,\ 1.2,\ 1.5,\ 1.8$ ps, driven by a pump of intensity 1×10^{16} Wcm^{-2}. The solution is governed by autoresonance until $t \sim 1.5$ ps, after which the Langmuir wave experiences an absolute growth behind the autoresonant wave front.

pump wave, after which the reflectivity chaotically oscillates around an average value of $R \sim 0.3$. The shaded region indicates the range of gains attained in the plasma after Rosenbluth saturation has taken place but before the gain has become saturated. The shade region is bound by the saturation gain.

From Fig. 4.7, it is clear that there is a range of gain factors ($0.75 < G_R < 6$) spanning laser intensities of 2.5×10^{15} Wcm^{-2} to 2.5×10^{16} Wcm^{-2} in which autoresonance and later absolute instability greatly enhances SRS. The size and shape of this region is of course sensitive to other parameters, such as $\tilde{\eta}$ and the plasma conditions. However, the figure shown indicates that for parameters relevant to ICF experiments, autoresonance may be of great importance.

4.1.1.1 The propagation of the kinetic nonlinear frequency shift

The Langmuir wave phase velocity v_ϕ, and hence the velocity around which particles are trapped, is significantly greater than c_L (for the parameters used here, $v_\phi/c_L = 4.0$). This raises an important question: At what velocity does the Langmuir wave propagate in the kinetic regime? In a series of recent publications, Bénisti *et al.* [71,72,73,74] proposed a new model for the Langmuir wave in an attempt bring theoretical predictions of the group velocity and nonlinear behaviour of the Langmuir wave in the kinetic regime closer to observations in Vlasov simulations. In summary, Bénisti *et al.* argued that the Langmuir wave

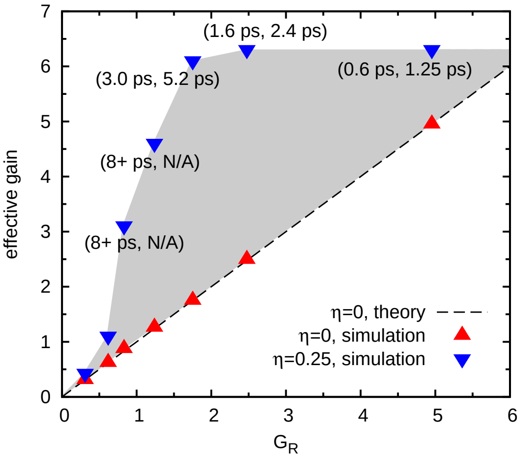

Figure 4.7: The reflectivities of Fig. 4.5 expressed as a gain factor plotted against the corresponding Rosenbluth gain factor. The black dashed line shows the analytical prediction of Rosenbluth gain saturation, in the absence of kinetic effects ($\eta = 0$). The red triangles indicate the saturation reflectivities obtained using the three-wave code, again in the absence of kinetic effects. The inverted blue triangles indicate the results of the three-wave code, including kinetic effects ($\eta = 0.25$). Where given, the pairs of numbers in brackets indicate the time at which autoresonance no longer dictated the evolution of the Langmuir wave, followed by the time at which growth became saturated.

is best modelled by considering the trapped and untrapped electron populations somewhat separately, and suggested that the observed velocity of propagation of a Langmuir wave (driven, or initially driven and then freely propagating) is best described by a weighted average of the velocities of the trapped and untrapped electrons, depending on the degree of trapping present. In the model constructed,

$$[\partial_t + c_L \partial_z + C(|\epsilon_L|)(\partial_t + v_\phi \partial_z)]\, \varepsilon_L = P, \tag{4.4}$$

where C is a slowly-varying function of the Langmuir wave amplitude. Using this model, the resultant Langmuir group velocity v_C is therefore a mix of c_L and v_ϕ, such that

$$v_C = (c_L + C(|\varepsilon_L|)v_\phi)/(1 + C), \tag{4.5}$$

where in this case c_L is the driven group velocity in the absence of trapping, described in detail in Ref.[74]. The group velocity observed by Bénisti *et al.* varied strongly as a function of the strength of the local electric field, with the degree of sensitivity dependent upon $k_L\lambda_D$. For example, for $T_e = 2$ keV, $k_L\lambda_D = 0.3$ and $\tilde{\varepsilon}_L = e\varepsilon_L/k_B T_e \sim 0.3$, where k_B is Boltzmann's constant, it was observed that

$v_C/c_L \sim 2.5$, where the driven value of c_L is smaller than the undriven value (i.e. the value obtained by differentiation of the Bohm-Gross relation) by a factor of 0.7.

Since Morales and O'Neil published their paper on the frequency shift of an electron plasma wave in the kinetic regime[18], most three-wave treatments have adopted a purely perturbative approach, where the effect of particle trapping is strictly to shift the frequency of the natural mode of the Langmuir wave envelope (in addition to reducing the Landau damping strength). This perturbative approach was adopted in this thesis, but with an additional consideration: In the three-wave simulations presented in this paper, the frequency shift was propagated *separately* from Langmuir wave envelope at v_ϕ, rather than c_L.

In three wave coupling simulations in this thesis, the local shift is equal to whichever is greater out of the following:

1. The local amplitude of the Langmuir wave envelope propagated at c_L, such that $\delta\omega^{nl} = \tilde{\eta}|\varepsilon_L|^{1/2}$.
2. The shift generated at an earlier time behind the point in question, propagated at v_ϕ.

We label the velocity of the kinetic nonlinear frequency shift propagation v_K. While it is only the frequency shift, and not the Langmuir wave envelope, that propagates at this raised velocity (i.e. the velocity in the operator $\mathcal{L}_L$, and hence in the finite difference integration scheme of the Langmuir wave, remains equal to c_L), there is an observable impact on the propagation of the autoresonant wave front of the Langmuir wave. This difference is however only observable when the Langmuir wave is strongly driven; in the examples earlier in the chapter, where the seed strength is such that $I_1/I_0 = 1 \times 10^{-6}$, there is no discernable difference between solutions to obtained using v_K equal to either c_L or v_ϕ.

In contrast, when the seed is increased such that, for example, $I_1/I_0 = 0.002$, a number of interesting things occur: First, at early times, the response of the Langmuir wave to the large ponderomotive drive provided by the strong pump and seed is sufficiently fast that the Langmuir wave front is tied to the propagation of the pump wave, i.e. the maximum in Langmuir wave envelope amplitude is at the front of the pump wave, thus the speed of Langmuir wave propagation is temporarily close to c_0. This is visible in Fig. 4.8, where the blue lines indicate the times at which the Langmuir wave is still affected by the group velocity of the pump (times $t = 0.3$ and 0.5 ps). It is also clearly apparent in Fig. 4.9, where the steep gradient in Langmuir wave propagation velocity is visible at the start of the Langmuir wave growth.

After the pump has crossed the simulation window, the Langmuir wave begins to grow autoresonantly, and it is now that the impact of differing values of v_K

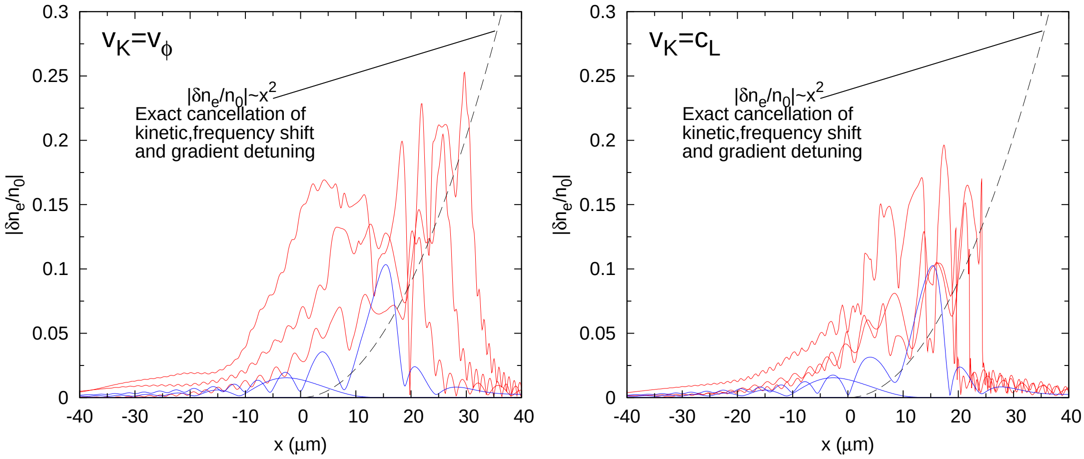

Figure 4.8: Langmuir wave envelope amplitude, obtained by solving the three wave equations. In both cases, the parameters are identical but for the velocity at which the kinetic nonlinear frequency shift propagates, v_K. (Left) Solution obtained for $v_K = v_\phi$. (Right) Solution obtained for $v_K = c_L$. In both cases, the blue lines indicate the initial response of the Langmuir wave to the passing of the pump wave. The red lines indicate the subsequent autoresonant evolution of the envelope amplitude. The interval between solutions is given by $\Delta t = 0.2$ ps, and both figures left and right show solutions in the range $t = 0.3 - 1.1$ ps.

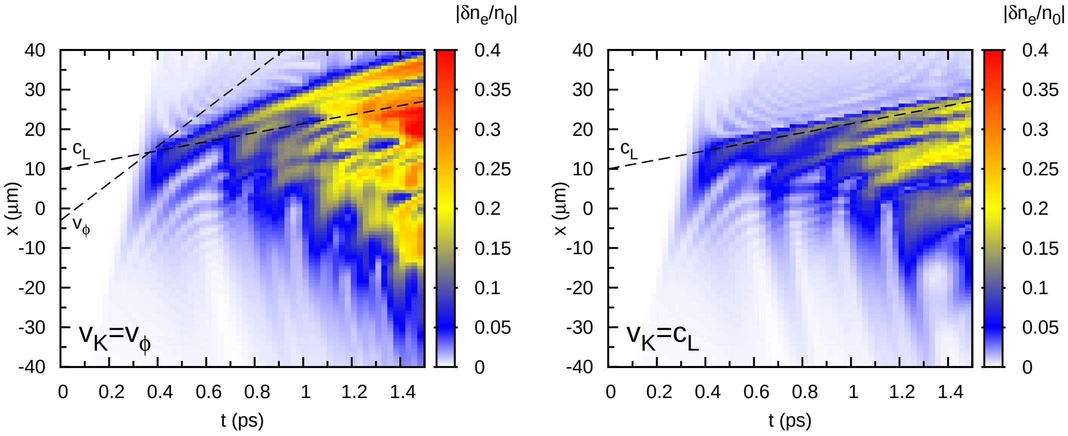

Figure 4.9: As above, but with the Langmuir wave envelope amplitude displayed as a function of both space and time. The case where $v_K = v_\phi$ displays a significantly increased autoresonant wave front velocity.

may be observed. Essentially, the velocity of propagation of the autoresonant Langmuir wave front is increased when v_K is increased. This effect is shown in Fig. 4.8, where both left and right figures have been generated using identical parameters but for the value of v_K, and are displayed for the same range of times ($t = 0.3 - 1.1$ ps, with sampling interval $\Delta t = 0.2$ ps). After 1.1 ps has elapsed in both simulations, the autoresonant wave front has propagated a significantly greater distance in the case $v_K = v_\phi$. This phenomenon is shown in detail in Fig. 4.9, where it is clear that in the case $v_K = v_\phi$ the speed of propagation of the autoresonant wave front lies roughly midway between c_L and v_ϕ, while in the case $v_K = c_L$, the speed of propagation of the autoresonant wave front is equal to c_L.

The important result of these simulations is the following: During autoresonance, the *observed* speed of propagation of the autoresonant Langmuir wave is not necessarily equal to the group velocity of the Langmuir wave, and for high pump intensities (i.e. pump intensities that generate a strong linear response in Langmuir wave amplitude), the speed of propagation may lie close to the phase velocity of the Langmuir wave. This phenomenon was not captured by the simple prescribed drive models used in the previous chapter, and is important in discussing the results of PIC simulations.

4.1.2 Autoresonance with three-wave coupling in a parabolic profile

In Sec. 3.4.4, autoresonance in a parabolic profile was demonstrated for a Langmuir wave driven by a prescribed (constant) ponderomotive force. While Rosenbluth[20] showed that a parabolic density profile was capable of supporting absolute growth for sufficient laser intensity, Picard and Johnston (1983)[75,76] showed that all non-linear inhomogeneous profiles were capable of doing so for a sufficient laser intensity (or sufficiently shallow gradient curvature). The presence of non-linear effects greatly complicates the issue of so-called "gradient stabilisation", and it is known that the inclusion of decay processes such as LDI may destabilise what would otherwise be a stable profile[77].

We once more consider a laser encountering backscattered light in an inhomogeneous profile (such as may be the case near the entrance to a hohlraum) and analyse the amplification of this light. The equations describing the system are

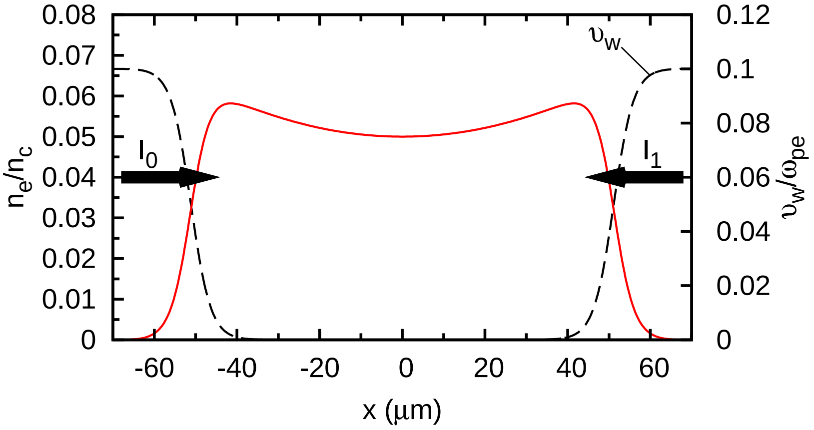

Figure 4.10: Parabolic density profile of the plasma used in three-wave coupling simulations. The red solid line shows the local electron plasma density, while the dashed black line shows the damping υ_w that was applied to the edges of the simulation window to prevent Langmuir wave propagation into the vacuum.

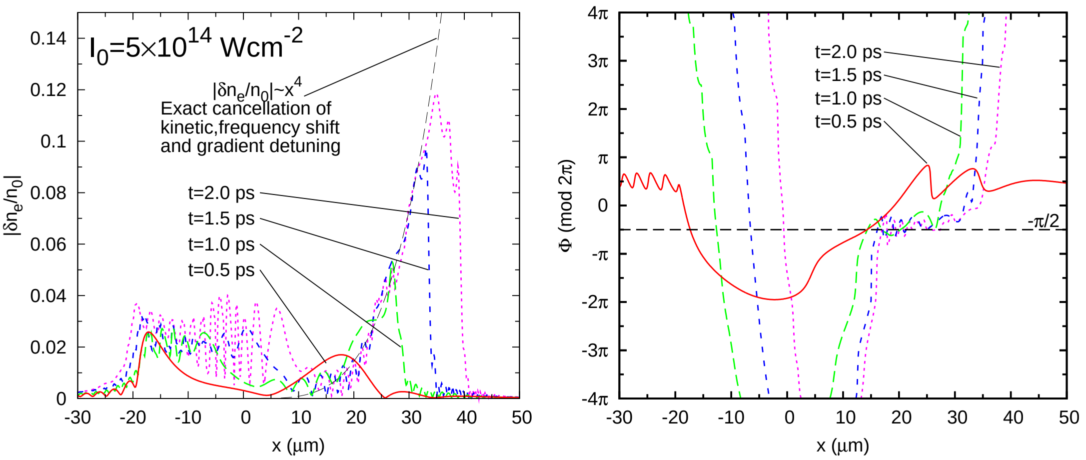

(a) (b)

Figure 4.11: (a) The amplitude of the Langmuir wave envelope showing autoresonant growth without absolute growth in a parabolic density profile in the kinetic regime. The black dashed line shows the exact cancellation of the kinetic nonlinear frequency shift and the wave number detuning due to inhomogeneity. (b) The three-wave phase difference, corresponding to the same series of times as (a).

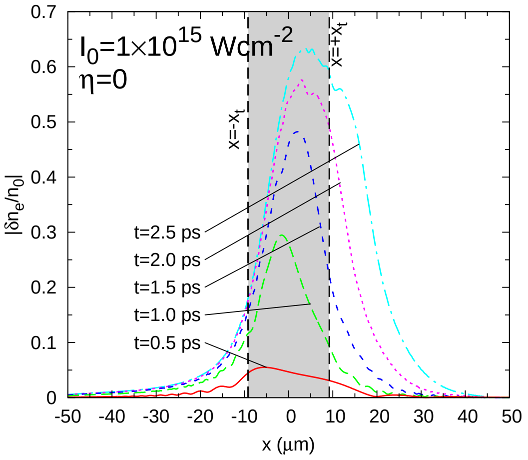

Figure 4.12: The Langmuir wave envelope amplitude, exhibiting initially absolute growth in a parabolic density profile. In the absence of kinetic effects ($\eta = 0$), the growth is stabilised by pump depletion. The turning points $x = \pm x_t$ defined by Eq. (2.90) are also shown.

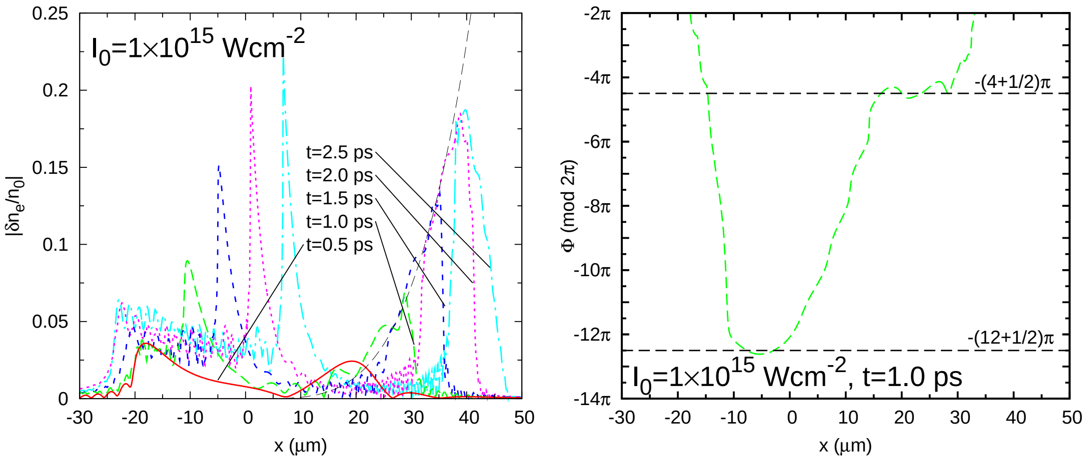

(a) (b)

Figure 4.13: As Fig. 4.11, but with a higher pump strength. (a) There is now a strong growth behind the resonance point in addition to in front of it that begins at the turning point $x = -x_t$ (see Fig. 4.12) and grows convectively. (b) The phase is once more locked at $\Phi = -\pi/2 \bmod(2\pi)$, but there is now an additional region of constant phase behind the resonance point.

the following:

$$\mathcal{L}_0 A_0 = -\frac{e}{4m_e}\frac{k_L}{\omega_0}\varepsilon_L A_1, \tag{4.6}$$

$$\mathcal{L}_1 A_1 = \frac{e}{4m_e}\frac{k_L}{\omega_1}\varepsilon_L^* A_0, \tag{4.7}$$

$$\left(\mathcal{L}_L + ic_L\kappa'' x^2 - i\tilde{\eta}|\varepsilon_L|^{1/2}\right)\varepsilon_L = \frac{e}{4m_e}\frac{k_L}{\omega_L}\omega_{pe}^2 A_1^* A_0. \tag{4.8}$$

In Fig. 4.11, we demonstrate autoresonance in three wave coupling in a parabolic profile *without* absolute growth. Here, $\lambda_0 = 351$ nm, $I_0 = 5 \times 10^{14}$ Wcm^{-2}, $I_1 = 5 \times 10^{12}$ Wcm^{-2}, $n_0 = 4.5 \times 10^{20}$ cm^{-3} ($n_e/n_c = 0.05$), $T_e = 1$ keV, $L = 100$ μm and $\eta = 0.25$, where the density profile is given by $n_e = n_0[1+(x/L)^2]$ and the three waves are initially resonant at $x = x_{res} = 0$. The evolution of the Langmuir wave is qualitatively unchanged from the ponderomotively driven example given in the previous chapter in Fig. 3.5b. The three-wave phase difference (Fig. 4.11b) once more shows phase locking at $\Phi = -\pi/2 \bmod(2\pi)$, leading to a growth in Langmuir wave amplitude that reaches $|\delta n_e/n_0| \approx 0.12$ before encountering the edge of the plasma. In the absence of kinetic effects, the pump strength would, according to Eq. (2.89), be high enough to provoke an absolute growth: $\gamma_0 \gg \gamma_{min}^{abs}, \gamma_{inh}$, where for these parameters $\gamma_0 = 1.4 \times 10^{-3}$, $\gamma_{inh} = 8.8 \times 10^{-4}$ and, because there is no damping, $\gamma_{min}^{abs} = 0$ (this absolute growth would be saturated by pump depletion, however). Despite being above this threshold, the nonlinear shift is sufficient to prevent (or reduce until not significant over the relevant timescales) absolute growth in this case, and autoresonant growth is dominant. There is also a growth *behind* $x = 0$. This growth is possible since the kinetic nonlinear frequency shift may cancel the wave number shift due to inhomogeneity either side of the resonance point, but only to the side towards which the Langmuir wave propagates is autoresonance possible.

We now increase the pump strength to $I_1 = 1 \times 10^{15}$ Wcm^{-2} while keeping the seed at $I_1 = 5 \times 10^{12}$ Wcm^{-2}. In Fig. 4.12, the absolute growth of the Langmuir wave in the absence of kinetic effects ($\eta = 0$) is shown, in addition to the turning points defined by Eq. (2.90). This growth is eventually stabilised by pump depletion. In Fig. 4.13, the evolution of the Langmuir wave amplitude and phase are shown, where kinetic effects are included. There is now a strong growth in Langmuir wave amplitude either side of the resonance point. This growth is accompanied by a region of constant phase at $\pi/2 \bmod(2\pi)$ (shown in Fig. 4.13b). The peak behind the resonance point appears to be growing convectively over the region defined by the turning points $x = \pm x_t = \pm 9.2$ μm, with amplification beginning at $x = -x_t$ (compare Fig. 4.13a with 4.12). The growth then continues until $x = +x_t$, after which the peak propagates without growing. In contrast, the autoresonant growth is *not* bound by the region defined by the turning points, instead provoking strong growth far from the resonance point. We see therefore that in this case, while absolute instability is not obviously restored by the increase in pump strength, that the convective growth rate γ_0 is important. The convective growth behind the resonance point is not present in prescribed drive simulations of any pump intensity. If the pump strength is increased still further ($I_0 \approx 5 \times 10^{15}$ Wcm^{-2} and above), it is difficult to determine the nature of the growth: There is a rapid and peaked growth in the Langmuir wave behind the resonance point and the model quickly reaches the limits of its validity (e.g. $|\delta n_e/n_0|$ approaches and rises above 1).

In the context of the work of Picard and Johnston discussed earlier in this section, a kinetic nonlinear frequency shift appears to stabilise growth in a parabolic profile, with certain caveats. For sufficient laser intensities, the autoresonant growth of the Langmuir wave and the corresponding growth behind the linear three-wave resonance point are significant. While the growth in reflectivity is slower than that which would arise in the absence of a nonlinear frequency shift, it remains substantial: for $I_0 = 5 \times 10^{15}$ Wcm^{-2}, reflectivities observed were in the region of $R = 0.1$ after 2 ps, and tended towards the pump depletion limit ($R \sim 0.3$) at later times. For laser intensities of $I_0 = 1 \times 10^{15}$ Wcm^{-2} and below, however, the growth was far slower, with reflectivities only of the order of $R \sim 0.03$ after 5 ps.

4.1.3 A broadband seed

Generating suitable noise is rarely simple. While many methods were tried, the simplest method to produce satisfactory results is summarised here.

Noise may be introduced to the three-wave equations in the form of either electromagnetic noise or electrostatic noise. Past unpublished studies have indicated that noise entering into the three-wave equations via the equation of the Langmuir wave in the form of electromagnetic noise more closely matches PIC simulations, thus it is this approach that is adopted here. The noise generated must be sufficiently broad in frequency so as to be able to drive all possible modes of Langmuir waves in the plasma (or, if introduced as electrostatic noise, to be able to drive all possible modes of backscattered light), even after a significant phase shift due to inhomogeneity and kinetic effects has been applied. In addition, in the absence of a varying wave coupling strength, no frequency should be preferentially driven. Thus, the noise frequency spectrum must also be flat in amplitude.

To this end, noise was generated with a Langevin equation of the form

$$\frac{dA_1(x_R)}{dt} = -\frac{A_1(x_R)}{\tau} + \frac{S}{\tau}, \tag{4.9}$$

where $|S|$ is the seed amplitude at the RHS boundary and $\arg(S) = 2\Xi\pi i$, for which Ξ is a random number in the interval $[0,1]$, and τ parameterises the spread in the frequency (and thus wave number) of the noise. It is also possible to write Langevin equations for both space and time and generate noise at every spatial point in the plasma. This was also done, but the results were observed to be effectively identical to simulations where the noise was generated at the boundary and propagated through the plasma. The parameter τ must provoke a noise that accounts for the largest frequency and wave number shifts. The maximum possible frequency shift of the Langmuir wave from the natural mode of the envelope is given by $\eta\omega_L|\delta n_e/n_0|_{max}^{1/2}$, where $|\delta n_e/n_0|_{max} = 1$. The maximum shift due to inhomogeneity that we consider is given by $c_L\kappa' x_{max}$, where $x_{max} = \max(|x_L|, |x_R|)$. Eq. (4.9) generates a noise about a central frequency and wave number peaked at zero that is symmetric, allowing for frequencies (and wave numbers) both greater and smaller than the natural mode of the envelope. Typically, in the three-wave simulations performed here, τ was a factor of 5 greater than necessary, ensuring that the spread of frequencies and wave numbers generated by the Langevin equation was effectively flat across the range relevant to the simulation window.

4.1.3.1 Results

We solve now the three-wave equations using a broadband noise to seed the system. As before, the seed was introduced at x_R and allowed to propagate fully throughout the simulation window before the pump was switched on. In Fig. 4.14, the reflectivity of the plasma for the autoresonant case ($\eta = 0.25$, blue line) and the case where kinetic effects are suppressed ($\eta = 0$, red line) are shown. The case where kinetic effects are suppressed displays an initial growth followed by saturation at a low value of R. We attribute this growth to Rosenbluth gain saturation, as observed earlier with a single-frequency seed.

The broad-frequency nature of the seed makes a direct comparison with single-frequency results difficult in the case $\eta = 0.25$, but for $\eta = 0$, the situation is essentially unchanged. In the envelope approximation, all parameters are calculated at a reference density, since the group velocities must be fixed for reasons of numeric stability. The coupling strength is however be allowed to vary, since this is strongly dependent on the local density. If instead *all* parameters are determined locally (and no natural mode is assumed), the gain factor G_R is in fact only weakly dependent on the local density: all factors of ω_{pe} and ω_L (i.e. parameters that vary strongly with density) in Eq. (2.79) cancel out, and the inhomogeneity of G_R is mostly due to the dependence of G_R on k_L^2. For the parameters used here, this means that the gain factor only varies in the range $1.261 < G_R < 1.265$ across the whole length of the simulation window. However, given the envelope formation adopted, the dependence of G_R on the local density is somewhat stronger,

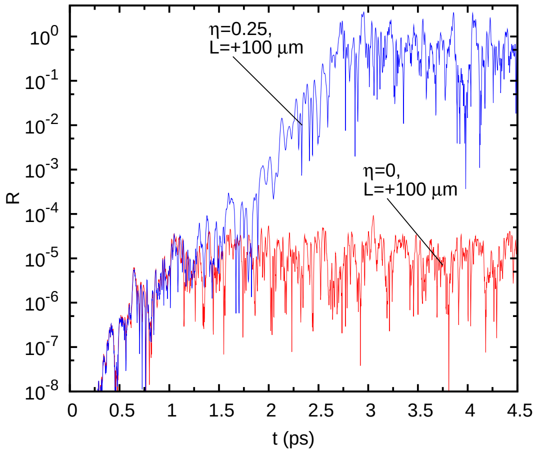

Figure 4.14: Reflectivity of the plasma, obtained by solving the three wave equations seeded with a broadband noise. The reflectivity of the plasma is greatly enhanced (red line) above the level reached in the absence of kinetic effects (blue line).

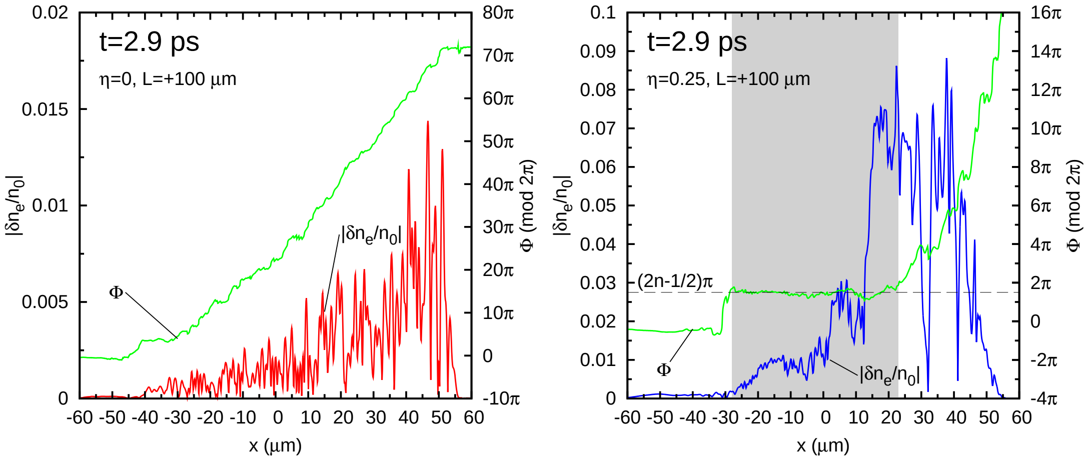

Figure 4.15: Solution to the three-wave equations showing the autoresonant Langmuir wave amplitude and phase at time $t = 2.9$ ps, at the end of the first growth in reflectivity shown in Fig. 4.14. (Left) Langmuir wave envelope amplitude and phase, solved in the absence of kinetic effects ($\eta = 0$). The phase changes rapidly and there is little growth in the Langmuir wave. The growth observed is consistent with Rosenbluth gain saturation. (Right) Langmuir wave envelope amplitude and phase, solved with kinetic effects ($\eta = 0.25$). The region of constant phase (light grey rectangle) corresponds closely to the region in the plasma experiencing a significant growth in Langmuir wave envelope amplitude, suggesting the importance of phase-locking in the determination of the behaviour of the Langmuir wave.

and consequently the gain varies in the range $0.63 < G_R < 1.89$ across the window. Since the seed is injected with an amplitude of $I_1(x_R)/I_0(x_L) \sim 1 \times 10^{-6}$, this is in agreement with Fig. 4.14 (red line), where the noise is amplified to $I_1(x_L)/I_0(x_L) \sim 1 - 2 \times 10^{-5}$. Thus, we see that the Rosenbluth solution is stable and accurate even with a broad-frequency noise. In Fig. 4.15 (left figure, red line), we see that the Langmuir wave envelope amplitude saturates at a level determined by the local gain factor (thus saturating at a level that increases with density). Also shown in Fig. 4.15 (left figure, green line), the three-wave phase difference Φ is observed to grow rapidly across the simulation window in an approximately linear fashion with no evidence of regions of constant phase (compare to Fig. 4.15, right figure, green line).

The case where $\eta = 0.25$ displays starkly different behaviour. In Fig. 4.14 (blue line), the reflectivity of the plasma quickly rises above the level of Rosenbluth saturation until it is stabilised by depletion of the pump wave. The Langmuir wave envelope amplitude shown in Fig. 4.15 (right figure, blue line) displays rapid growth over regions of constant phase. After 2.9 ps, the amplitude of the Langmuir wave is greater by a factor of ~ 10 compared to the case where $\eta = 0$ (note also the smaller range over which Φ varies). Growth occurs at $\Phi = (2n - 1/2)\pi$, where n is an integer, and ends where the phase is observed to change rapidly. Although the growth appears absolute, there are strong similarities between the simulations when resonance occurs at a single point (where the seed is of a single frequency) and the simulations presented here where the seed is of a broadband nature.

4.2 A Raman amplifier

From the results of Chapter 3, it is clear that autoresonance may arise in a wide range of plasma conditions and may therefore be present in many plasma experiments. We consider in this section one such experiment.

In ICF experiments, SRS is a highly undesirable process, and consequently an array of techniques are employed to mitigate it and other scattering processes. As discussed earlier in this chapter, SRS of laser light may be seeded by thermal fluctuations in the plasma. However, it is also quite possible to drive SRS deliberately using a second laser beam: By selecting the operating wavelengths of the two lasers, a single Langmuir wave mode may be resonantly driven at a particular frequency (and thus density) in the plasma. Under these conditions, the laser of lower frequency will be amplified by the SRS process. This arrangement forms the basis of an amplifier, typically referred to simply as a “Raman amplifier”.

Shvets *et al.*[78] described how an initially short ($< 1/\omega_{pe}$) laser pulse can be superradiantly amplified by a counterpropagating long low-intensity pump while remaining ultrashort. Malkin, Shvets and Fisch[79] subsequently described how laser light may be strongly compressed by SRS in a plasma over a timescale that is sufficiently short such that filamentation instabilities do not have time to develop. The compression of laser light in this way would permit the generation of multi-MJ, multi-exawatt laser pulses more easily than by other current means; many pulse compression schemes already exist, but ultra-high laser intensities are damaging to the optics required during amplification. Plasma thus provides an attractive alternative, both in terms of cost and simplicity.

In Ref.[6] (described further in Ref.[80]), significant advances were made over previous attempts at pulse amplification. In previous experiments, amplification efficiencies had been of the order of 1%, but recent advances have progressed to 6.4%, with pulse amplifications of two orders of magnitude above the pump intensity (2×10^4 times greater than the initial pulse): Over a 2 mm plasma, intensities of the order of 10^{20} Wcm^{-2} were achieved, with a planned target intensity in future experiments of 10^{25} Wcm^{-2}. The generated plasma was strongly inhomogeneous over certain regions, and employed a unique "double pass" system where the pulse passed through the plasma twice used to achieve the amplification levels reported (future experiments using many passes through the plasma are envisaged).

The limiting effects of Raman amplification are summarised in Ref.[81], namely frequency detuning due to the chirp of the pump wave (though this a smaller concern for longer pump durations), frequency detuning due to compression of the pulse wave, wave number detuning due to inhomogeneity, wave breaking of the Langmuir wave and Landau damping.

In Fig. 4.16, the "ideal" case of Raman amplification is shown. At the RHS of the window, a pulse of $I_1 = 1 \times 10^{15}$ Wcm^{-2} is injected into an oncoming pump wave of equal intensity that has already crossed the window from the LHS where it is injected to the RHS. The plasma has a temperature of 1 keV and a homogeneous density profile, for which $n_e/n_c = 0.05$. The pump wave has wavelength $\lambda_0 = 351$ nm, while the pulse wavelength is chosen so that the linear dispersion relations of the three waves are satisfied throughout the plasma. Spatial amplification of the pulse leads to an efficient growth in the pulse intensity as it crosses the window, with only pump depletion limiting the growth; while nonlinear Landau damping and kinetic effects were included, these did not play a significant role in the evolution of the pulse. The Langmuir wave reached amplitudes of approximately $|\delta n_e/n_0| \sim 0.2$. In a similar experimental case (or in full kinetic simulations), increasing the pump intensity would not necessarily result in a significant increase in amplification due to the onset of wave breaking.

The inhomogeneous plasma generated during the amplification experiments of Ref.[6] is depicted in cross-section in Fig. 4.17. The density gradient is approximately linear at the edges of the plasma, with a scale length of $L \sim 250$ μm. Ra-

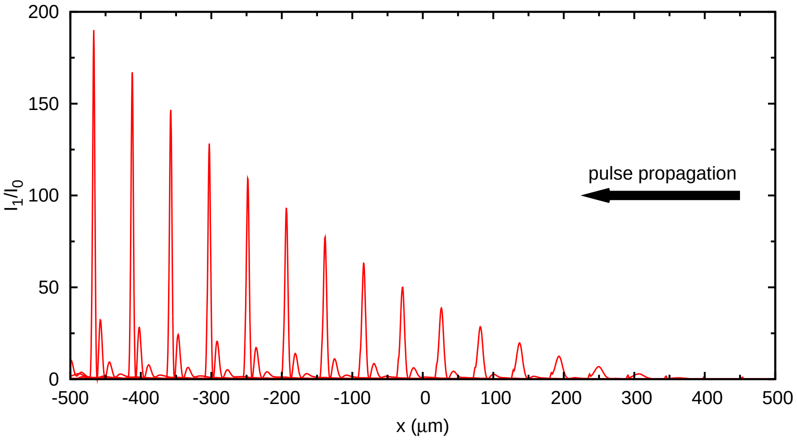

Figure 4.16: A series of snapshots showing Raman amplification of a short pulse after a single passage across the plasma. The amplified pulse is introduced at the RHS of the window with an intensity of 1, normalised to the LHS pump intensity I_0.

man amplification in inhomogeneous plasmas in the absence of kinetic effects was considered by Malkin *et al.*[82], who reported that inhomogeneity was desirable under certain conditions: by performing the amplification in an inhomogeneous density profile, a reduction in potentially problematic interaction of the pump wave with thermal noise rather than with the pulse is possible. Yampolsky and Fisch[52] considered a reduction in the nonlinear Landau damping due to kinetic effects. In Ref.[83], the same authors considered both a nonlinear Landau damping and a kinetic frequency shift due to trapping. Brief mention is made in this article of the possibility of compensating the kinetic nonlinear frequency shift with a wave number shift arising from inhomogeneity, and it is with this same concept in mind that autoresonance is sought in this section.

In Ref.[6], the first pulse entering the plasma is of a duration of 500 fs, and is injected at an intensity below that of the pump wave. Since the pulse undergoes significant compression during amplification (down to the order of 30 fs in Ref.[6]), longer initial seed pulses are generally desirable, permitting a greater amount of energy to be carried in the final pulse. The pulse is then passed through the plasma a second time, now having a higher intensity. We therefore look at two cases: the passage of a weak pulse ($I_1 \ll I_0$) through an inhomogeneous density profile and a stronger pulse ($I_0 = I_1$) through the same profile. The impact of autoresonance will then be determined by comparing results from positive and negative profiles.

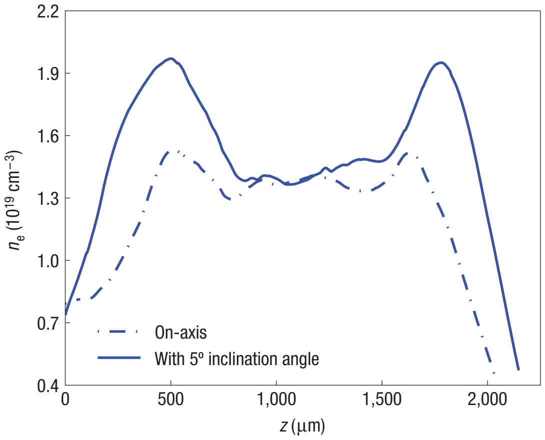

Figure 4.17: Typical density profile used in Raman amplifier experiments. Adapted from Ref.[6].

In Fig. 4.18, an example of the passage of a pulse through a linearly inhomogeneous ($L = \pm 250$ μm) density profile is shown. In the figures shown here, $k_L\lambda_D \approx 0.36$, in agreement with the range of values of $k_L\lambda_D$ used in experiments (see Ref.[81] and references therein). Using pump and pulse intensities of $I_0 = 1 \times 10^{15}$ and $I_1 = 1 \times 10^{13}$ Wcm^{-2}, respectively, the resulting transmitted pulse is shown in Fig. 4.18(a). Simulations performed with a higher seed intensity are shown in Fig. 4.18(b), where pump and pulse intensities of $I_0 = I_1 = 1 \times 10^{15}$ Wcm^{-2} were used.

The positive density gradient is associated with a raised amplification of the pulse in both cases compared to the negative gradient. However, the quality of the pulse is somewhat negatively affected, with a loss of temporal confinement, but this may be of little importance after the pulse undergoes compression during subsequent amplification across the more homogeneous parts of the plasma. The difference between positive and negative density profiles in Fig. 4.18(a) is smaller than that in Fig. 4.3 owing to the comparatively short seed pulse duration in Raman amplifiers. However, this larger difference may be recovered in future experiments employing longer seed pulses. Current experimental techniques involve the repeated passing of the pulse through the plasma, providing multiple chances for autoresonance to take place. Further studies are planned to better examine autoresonance in Raman amplifiers; through control of the density profile produced, autoresonant effects could be enhanced or suppressed accordingly. The interplay between the bandwidth-broadening effects of amplification and autoresonance should also be investigated.

Although not of relevance to ICF, lower electrons temperatures such as $T_e =$

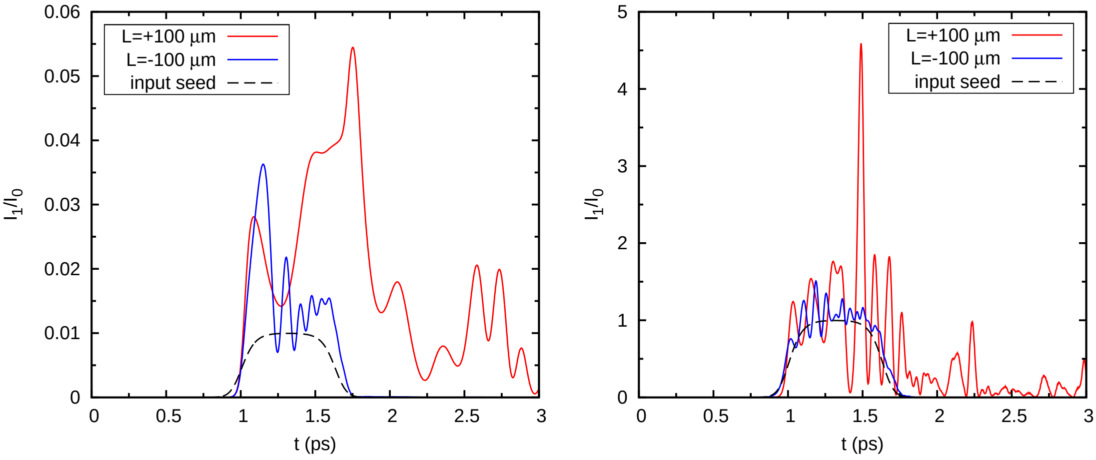

(a)

(b)

Figure 4.18: Pulse amplification in a Raman amplifier in inhomogeneous plasmas. (a) At initial low pulse intensities ($I_1/I_0 = 0.01$), the pulse gains a significantly greater amount of energy when propagating through a positive density profile compared to a negative density profile. (b) At higher pulse intensities ($I_1 = I_0$), there is little amplification in either profile, but high-amplitude oscillations in the pulse are observed in the positive density profile case.

200 eV may be found in Raman amplifier experiments (although these may rise significantly due to thermalisation of decay waves and scattering), while still being in the kinetic regime[81]. In this case, the Langmuir wave does not propagate a significant distance over the relevant timescales. At first inspection, an effectively stationary Langmuir wave would seem to make spatial autoresonance impossible. However, simulations indicate that, while not identical to the autoresonance mechanism discussed in Chapter 3, a spatial cancellation of the kinetic nonlinear frequency shift and the wave number mismatch due to inhomogeneity is still possible. This is demonstrated in Fig. 4.19, where the two curves show the Langmuir wave response to a Gaussian pulse (FWHM width $\Delta\tau = 500$ fs) in a plasma where $T_e = 200$ eV, $n_e/n_c = 0.01$, $k_L\lambda_D \approx 0.37$, $I_0 = 1 \times 10^{15}$ and $I_1 = 1 \times 10^{13}$ Wcm^{-2}. The plasma gradient scale length was chosen to be $L = \pm 250$ μm. Since $c_L\Delta\tau$ is small compared to the size of the simulation window (and the region over which the Langmuir wave may interact with the EM waves), the group velocity of the Langmuir wave is negligible and the equation governing the Langmuir wave evolution is flipped about $x = 0$ under a change of sign of L, producing the mirror-image solutions for the Langmuir wave growth in the two cases shown in Fig. 4.19 (The reflection is not perfect since c_L is not

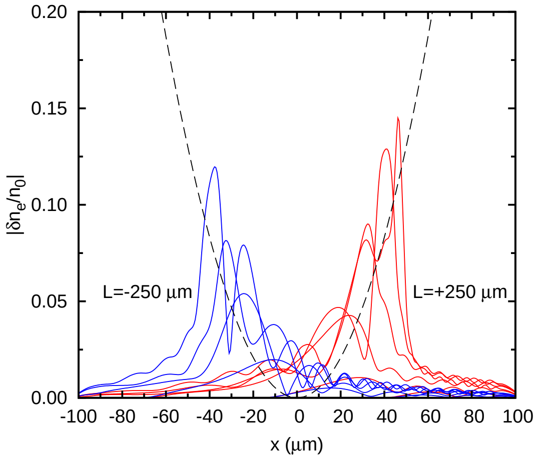

Figure 4.19: Langmuir wave envelope amplitude after passage of a Gaussian pulse through an inhomogeneous profile. In this case, the plasma temperature is sufficiently low that the Langmuir wave group velocity is negligible. The dashed line indicates the growth expected for an exact cancellation of the kinetic nonlinear frequency shift and wave number detuning due to inhomogeneity. The time step between snapshots is $\Delta t = 0.2$ ps, taken over an interval $0 < t < 1.2$ ps. In both cases, growth begins at $x = 0$ and propagates away from the resonance point.

exactly zero. The symmetry is further broken by the asymmetry in the electromagnetic wave propagation.). Similar to the discussion of velocity in Sec. 4.1.1.1, this effect is only observed at higher ponderomotive drive strengths; decreasing the seed pulse amplitude to $I_1 = 1 \times 10^9$ Wcm^{-2} simply results in the resonant growth remaining stationary around $x = 0$.

4.3 Chapter summary

The results presented in this chapter show that autoresonance is possible in three-wave coupling. In a linear profile, autoresonance may provoke a growth in Langmuir wave amplitude and scattered light far greater than the level at which saturation would be expected in the absence of kinetic effects calculated by Rosenbluth[20], and greater also than the level observed when the gradient is of the incorrect sign to allow the cancellation of the kinetic frequency shift and the wave number shift due to inhomogeneity.

When a pump wave encounters a low-amplitude seed in a linear plasma density profile, we expect that the amplitudes of the daughter waves will saturate at a level determined by the gain coefficient of the plasma, as calculated by Rosenbluth[20] (assuming that pump depletion is not significant). The presence of kinetic effects permits an autoresonant growth in the Langmuir wave amplitude that enhances the reflectivity of the plasma. Following a period of autoresonant behaviour, kinetic effects may also destabilise the system and provoke an absolute growth in the daughter wave amplitudes, further enhancing the reflectivity of the plasma. In parabolic density profiles, autoresonance in three-wave coupling is still possible. However, the solutions obtained display a lower stability than those obtained in a linear density profile. In the following chapter, particle-in-cell simulations are used to confirm these findings.

Chapter 5

Autoresonance in PIC simulations

In the previous chapters, a theoretical model for three-wave coupling and autoresonance was presented. Simulations were performed using a fluid code, so-called because the plasma was modelled as a charged fluid. In these fluid simulations, autoresonance was observed in both linear and parabolic density profiles, and was shown to be robust to a nonlinear Landau-type damping. The collective results of these studies points to the possibility of spatial autoresonance in SRS in the kinetic regime, acting to enhance the growth of the Langmuir wave and scattered light to levels of relevance to ICF.

To move closer to experimental conditions, we now look for autoresonance in particle-in-cell (PIC) simulations. PIC simulations are a direct and powerful tool for investigating a wide range of phenomena in plasmas. The basic methodology is straight-forward: the motion of the individual charged particles that constitute the plasma is numerically modelled in self-consistent electric and magnetic fields. First, the positions and velocities of the particles are used to calculate the current and charge densities on a spatial mesh fine enough to resolve the collective behaviour (typically, the Debye length λ_D must be resolved). The self-consistent electric and magnetic fields are then computed using Maxwell's equations. These fields, in addition to any externally applied fields, are then used to advance the positions and velocities of the particles, using a time step small enough to resolve the highest frequencies present.

If the number of particles is not sufficient or the spatial mesh and time step are too coarse, PIC codes are susceptible to detrimental numerical noise and instability[84]. Consequently, the number of particles used in PIC simulations is large (in the simulations presented here, up to 6×10^3 particles per cell were used in over 5×10^4 cells, although higher resolutions were used to check convergence). The high particle number coupled with the fine spatial mesh and small time step size required to correctly resolve the particle motion means that PIC codes are computationally expensive. Under conditions similar to those used in this chapter, Masson-Laborde *et al.*[46] recently found that the evolution of the Raman instability was dominated by one-dimensional (1D) effects, and two-dimensional (2D) processes were only important after the first saturation of the reflectivity. This study also supports the use of a kinetic nonlinear frequency shift in three-wave coupling models of the form described in Chapter 2, Sec. 2.4.4.1. Thus, we restrict our treatment here to the use of the 1D PIC code EMI1D, developed by Anne Héron and Jean-Claude Adam.

PIC codes incorporate a much broader range of physical phenomena than fluid codes, thus better represent experimental conditions. Consequently, however, the results are often difficult to interpret. The comparison between fluid codes and PIC codes is therefore an extremely useful one, since the physical processes present in fluid are simply those that are written into the code as additional terms in the envelope equations of the three waves. In this chapter, a range of PIC simulations results are presented. First, SRS levels in inhomogeneous plasmas of varying density gradient are presented, generated by the interaction of a laser with broadband noise (In PIC codes, this noise originates primarily from the granularity of the particle representation and is proportional to $N^{-1/2}$, where N is the simulated number of particles per cell. This noise should correspond to thermal fluctuations in the plasma.). Next, the value of η that parameterises the kinetic nonlinear frequency shift used throughout this thesis is calculated. Finally, an unambiguous example of autoresonance in PIC simulations is sought by driving a Langmuir wave using counter-propagating beams, and results are compared to fluid simulations carried out under equivalent conditions.

5.1 PIC simulations of SRS in inhomogeneous plasmas using a single laser

We begin by considering a single laser propagating through a plasma. In PIC simulations, a wide array of laser-plasma interactions are possible. At a plasma density of $n_e/n_c \sim 0.05$ and in the regime $k_L\lambda_D \sim 0.33$, we expect backward SRS to be the dominant scattering process of the laser. This should be clearly apparent in the spectrum of light reflected (and transmitted) by the plasma: For a given laser frequency ω_0 and local plasma frequency ω_{pe}, the dispersion relations of the three waves defined in Eqs. (2.38-2.40) may be solved, and the mechanism responsible for scattering the laser light confirmed.

As discussed in fluid simulations in Sec. 4.1.3, the laser may resonantly drive SRS at every point in the plasma due to the broad spectrum of noise present in the simulation. Autoresonance is consequently possible throughout the plasma. Since growth is possible at all points in the plasma, no apparent parabolic spatial growth in Langmuir wave amplitude is expected. However, as found in fluid simulations, we would expect the reflectivity of the plasma to be higher when the density gradient increases in the direction of propagation of the BSRS-driven Langmuir wave, allowing the cancellation of the wave number detuning due to inhomogeneity and the nonlinear frequency shift due to electron trapping.

In Figs. 5.1(a)-5.1(f), a range of linear density profiles are shown. In each case, the plasma conditions are identical, where $T_e = 1$ keV and at the centre of the plasma, $n_e/n_c = 0.05$. In total, six cases are presented, differentiated by the value of the density gradient parameter $L = [(1/n_0)dn_e/dx]^{-1}$ used to generate the density profile: $L = \pm 100$, ± 200 and ± 300 μm, where $n_e = n_0(1 + x/L)$. Laser light of intensity 5×10^{15} W/cm^2 and wavelength 351 nm is then introduced at the LHS of the simulation window.

The resulting reflectivity of the plasma, collected at the LHS of the window (and after spectrally filtering out laser light reflected without scattering by the discontinuity in density at the vacuum-plasma boundaries), is presented in Fig. 5.3. Figs. 5.3(a)-5.3(f) are the reflectivities of the plasma profiles 5.1(a)-5.1(f). The reflected light was found to be of a frequency within the range expected due to SRS, broadened by the range of densities present and the frequency shift due to kinetic effects. In each case, it is clear that the reflectivity is significantly increased when the density gradient is positive (for $L = \pm 400$ μm, this is true until after the first saturation of the reflectivities, after which the eventual saturation values are approximately equal). The negative density profile reflectivities reach saturation sooner, and in the case $L = -400$ μm, the initial growth is faster that the case $L = +400$ μm (this is simply because the SRS growth rate is highest at the maximum density, thus when the gradient is negative, the laser encounters the maximum density after propagating a shorter distance).

The difference between positive and negative density profiles is greatest when the gradient is steepest i.e. for the values presented here, $L = \pm 100$ μm. This is as expected: using the relation

$$\left|\frac{\delta n_e}{n_0}\right| = \left(\frac{c_L \kappa'}{\omega_L \eta}\right)^2 (x - x_{res})^2, \tag{5.1}$$

it is clear that decreasing L (and therefore increasing κ') will result in a more rapid growth in Langmuir wave amplitude. It was also demonstrated in Sec. 3.4.4 that while increasing the rate of autoresonant growth, decreasing L lowers the level at which autoresonant growth of the Langmuir wave saturates. However, as the level of reflected light throughout the plasma increases (due to resonant SRS or autoresonance), the strength of the ponderomotive force that drives the autoresonant Langmuir wave will increase, rasing the level at which saturation due to the loss of autoresonance occurs.

These findings are supported by studies performed by Strozzi[7], shown in Fig. 5.2. These simulations, performed using the Vlasov code ELVIS, were carried out under similar conditions: $T_e = 3$ keV, $n_e/n_c = 0.1$, a plasma length of 100 μm, and $L = \pm 167$, ± 250 and ± 500 μm. Here, $I_0 = 2 \times 10^{15}$ W/cm^2, $\lambda_0 = 351$ nm for the laser, and $I_1 = 2 \times 10^{10}$ W/cm^2, $\lambda_0 = 574$ nm for the seed, and $k_L \lambda_D \sim 0.36$. Qualitatively, the same behaviour as that which was found in the PIC simulations presented here is observed, with the plasma reflectivity showing significant enhancement when the gradient is positive as opposed to negative. Indeed, the effects of autoresonance may be greater in this regime than in the regime discussed earlier, since the higher electron temperature and consequently the higher Langmuir wave group velocity result in a significantly higher autoresonant growth rate.

While these findings agree with the behaviour predicted by autoresonance, it is not possible to say with certainty which mechanism is responsible for the enhancement of the reflectivity in the simulations presented here, since autoresonance does not provide an obvious signature in the reflected light of the plasma. It is desirable therefore to arrange conditions favourable to autoresonance so that its presence in kinetic simulations may be unambiguously established. This is performed later in the chapter.

5.1.1 Calculating η

Throughout this thesis, the free parameter η has been used in analytic calculations and three-wave coupling models in order to determine the size of the kinetic nonlinear frequency shift $\delta\omega = -i\eta\omega_L|\delta n_e/n_0|^{1/2}$. The accurate determination

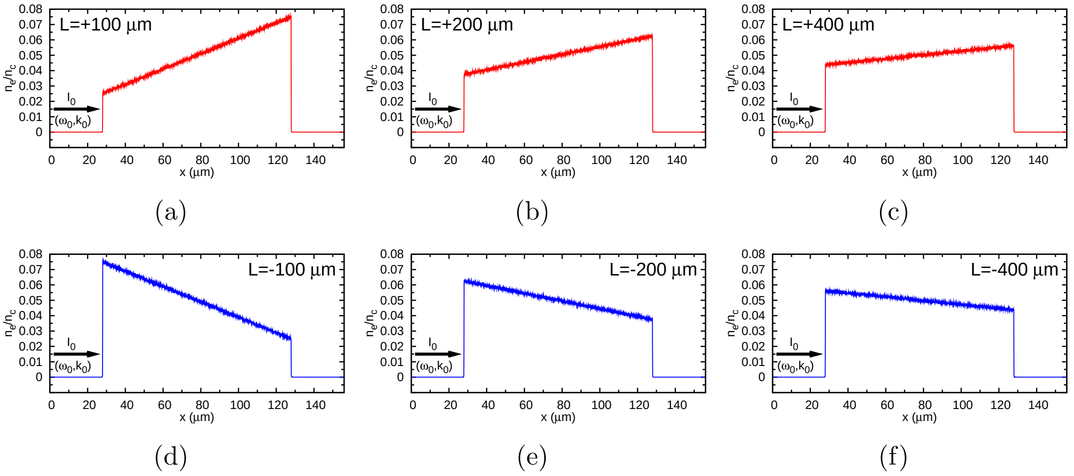

(a) (b) (c)

(d) (e) (f)

Figure 5.1: Plasma density profiles used in PIC simulations where a single laser is used to drive SRS. All parameters but the density gradient parameter L are identical in each case.

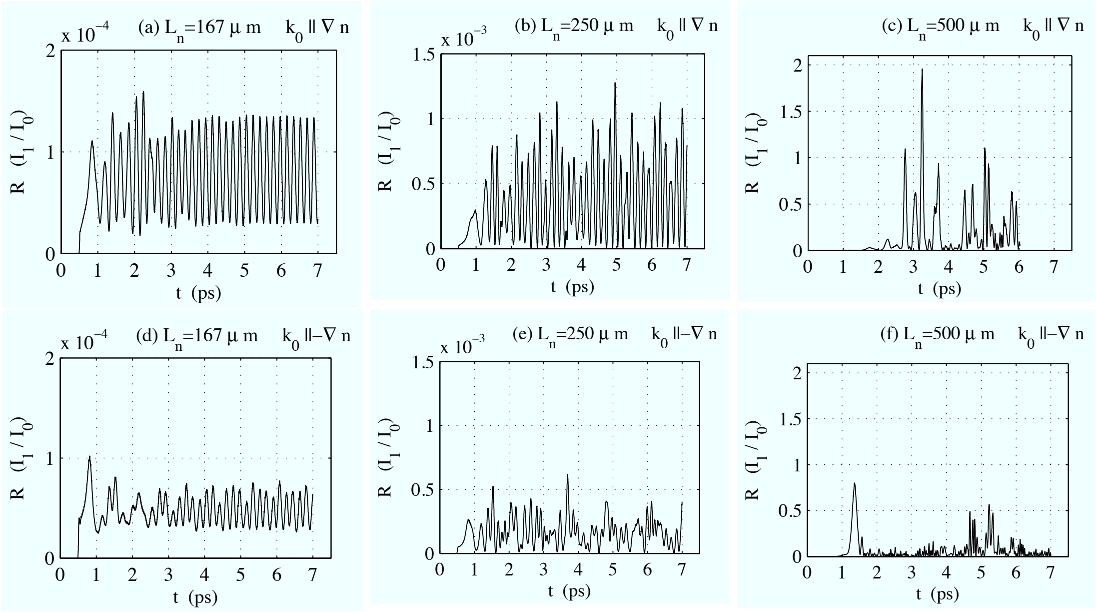

Figure 5.2: SRS reflectivities calculated using the Vlasov code ELVIS, written and run by D. Strozzi[7]. SRS levels are significantly raised when the gradient increases in the direction of propagation of the Langmuir wave resonantly driven by the laser (here, k_0 is the Langmuir wave vector, and the only parameter varied between each simulation is the density gradient parameter $L_n \equiv L$). The plasma parameters are similar enough to allow qualitative comparison with Fig. 5.3. Figures adapted from Ref.[7].

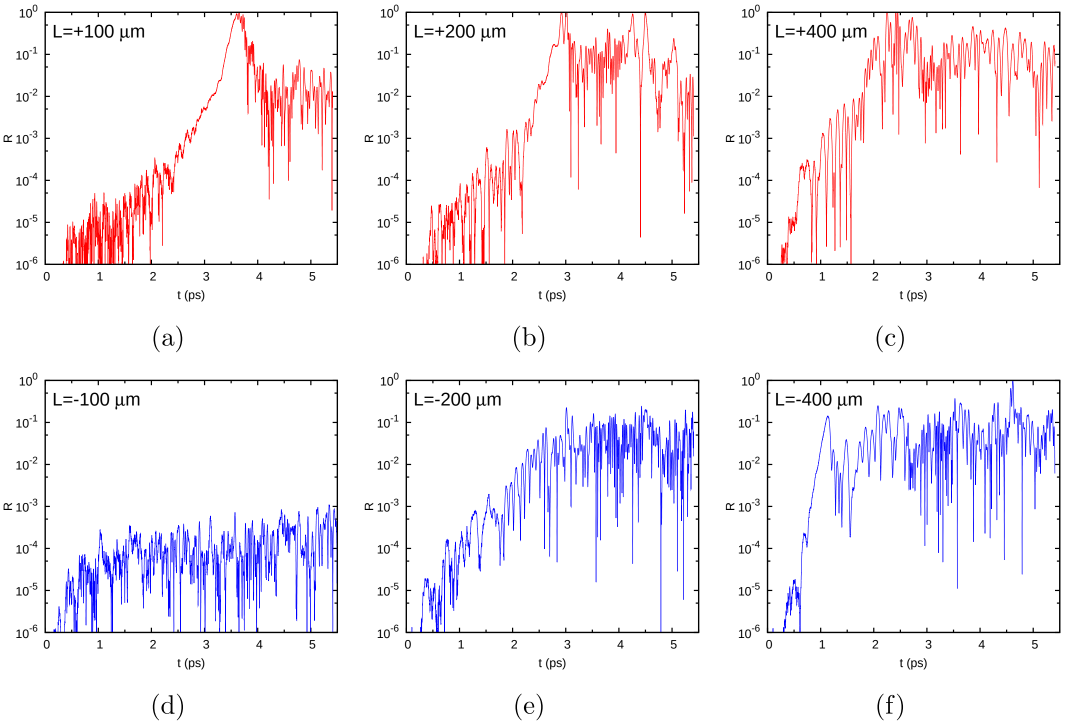

(a) (b) (c)

(d) (e) (f)

Figure 5.3: Plasma reflectivity from PIC simulations where a single laser is used to drive SRS. Each simulation is performed with identical laser parameters and under identical plasma conditions, but for the density gradient parameter L. The density profile used in each case corresponds to those shown in Fig. 5.1. In each case, it is clear that the reflectivity of the plasma is greater when the gradient increases in the direction of propagation of the BSRS-driven Langmuir wave.

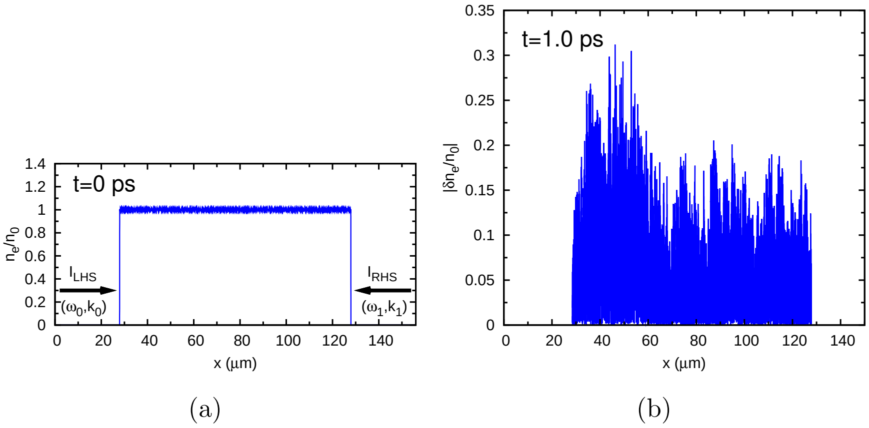

(a) (b)

Figure 5.4: (a) The flat density profile used in PIC simulations to determine η. (b) The Langmuir wave amplitude at $t = 1$ ps, where only the LHS laser is applied.

of η is therefore important. As discussed in Chapter 2, Sec. 2.4.4.1, several theoretical methods for calculating η are known that are applicable in different circumstances. Since we wish to compare and contrast PIC simulation results with analytic calculations, it is desirable to measure directly the value of η that is present in the PIC simulations (and indeed to confirm the presence of the assumed frequency shift due to kinetic effects). Recording $\delta\omega$ using the longitudinal field in the plasma is not practical, since this requires recording the field throughout the plasma with a high time resolution.

The fastest growing mode in the plasma is the resonant mode. Since the laser frequency is fixed at the boundary, the $\delta\omega$ shift of the Langmuir wave frequency may be determined by analysing the corresponding frequency shift of the scattered light. Thus, reflected light may be collected at the boundary of the simulation window, and the frequency shift of the Langmuir wave determined by the analysing the behaviour of the scattered light frequency.

Attempting to measure the frequency shift in an inhomogeneous plasma is difficult due to the broad resonant frequency spectrum present; laser light will scatter from density fluctuations (noise) at all points in the plasma simultaneously. Furthermore, the growth rate of the scattered light is greater at higher densities, thus scattering from higher densities dominates the frequency spectrum. Therefore, in order to isolate the frequency shift of a single Langmuir wave frequency in the plasma, we consider a plasma of homogeneous density such that $n_e/n_c = 0.05$ everywhere within the plasma (shown in Fig. 5.4, left). We then introduce laser light at the boundaries of the simulation window as before. As described earlier, we choose laser parameters and plasma conditions of relevance to NIF experiments, where $\lambda_0 = 351$ nm, $I_0 = I_{LHS} = 5 \times 10^{15}$ Wcm^{-2}, $n_0 = 4.5 \times 10^{20}$ cm^{-3} ($n_e/n_c = 0.05$) and $T_e = 1$ keV. So far, laser light has only been applied at the LHS boundary, but later in this chapter, counter-propagating beams will be used to drive autoresonance. In Fig. 5.5, the reflectivity of the plasma is shown in these two cases: The uppermost figure shows the reflectivity of the plasma, collected at the LHS of the simulation window, when *only* the LHS laser is switched on. In this case, the frequency of the reflected light increases slowly as a function of time as the Langmuir wave grows, until an eventual plateau. The dashed line indicates the reference frequency ω_1^{ref}, equal to the frequency at which the backscattered light will be produced in the absence of a nonlinear frequency shift [calculated by solving the linear dispersion relations, Eqs. (2.38-2.40)]. The result is as we expect: The laser frequency ω_0 is determined at the LHS boundary. The frequency of the Langmuir wave ω_L *decreases* as its amplitude grows due to kinetic effects. The frequency of backscattered light ω_1 that is resonant with the Langmuir wave therefore *increases* in time in order to fulfill the three-wave resonance condition $\omega_0 = \omega_1 + \omega_L$.

In Fig. 5.5, the lower figure shows the reflectivity of the plasma when *both* the

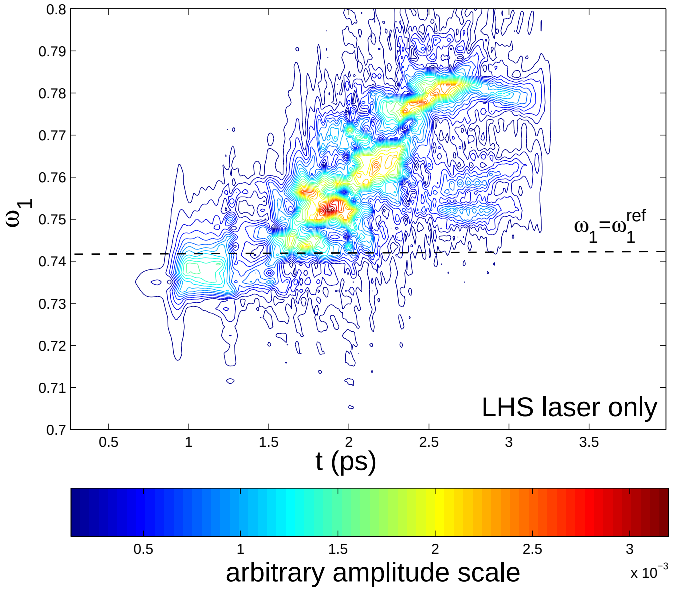

(a)

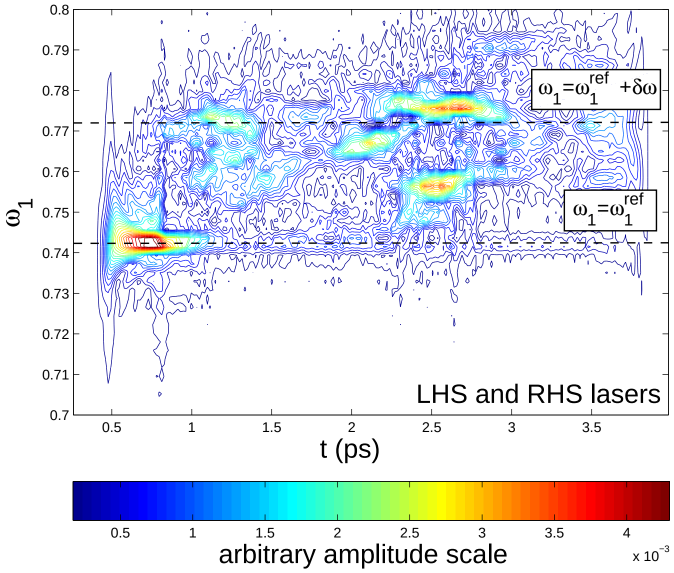

(b)

Figure 5.5: The reflectivity of a plasma of homogeneous density profile (Fig. 5.4, left) showing the kinetic nonlinear frequency shift, measured using PIC simulations. (a) The reflectivity obtained when only the LHS laser is switched on. (b) The reflectivity obtained when both LHS and RHS lasers are switched on. While the frequency shifts are similar, the timescales differ greatly.

LHS and RHS lasers are applied, where $I_1 = I_{RHS} = 1 \times 10^{13}$ Wcm^{-2}. As in the previous case where only the LHS laser was applied (Fig. 5.5, top), both lasers will scatter from density perturbations in the plasma. However, since the amplitude of the field fluctuations present in the plasma is much lower than that of the lasers, the growth of scattered light due to the noise will be much slower than the interaction between the two fixed-frequency lasers and the plasma, resonant at $x = x_{res} \approx 78$ μm. The direction and plateau amplitude of the frequency shift are essentially unchanged from the previous case. It is a useful and important result that the kinetic nonlinear frequency shift is applicable to both a Langmuir wave that grows slowly from noise and to a Langmuir wave that is strongly driven by counter-propagating laser beams.

Since autoresonance driven by counter-propagating occurs over timescales of around 1 ps, we will measure η at this time in the driven case. At 1 ps, we observe a frequency shift of $\delta\omega \sim 0.03$. At this time, we see in Fig. 5.4 (right) that the Langmuir wave envelope amplitude is of the order $|\delta n_e/n_0| \sim 0.2$ in the growing region of the plasma (i.e. the region which is responsible for the majority of the backscattered light). Using the expression for the frequency shift $\delta\omega = -\eta\omega_L|\delta n_e/n_0|^{1/2}$, we find a value of $\eta \sim +0.25$. It should be stressed that while this value is approximate, three-wave simulations using the fluid code generally display a low sensitivity to variations of η in the range $0.2 < \eta < 0.3$. Measurements of η at densities near $n_e/n_c = 0.05$ showed little variation. It is this value of $\eta = 0.25$ that was used in all simulations in this thesis.

5.2 Driving autoresonance using counter propagating beams

The enhancement of plasma reflectivity levels in positive density profiles compared to negative density profiles was established in Sec. 5.1. We wish now to provide a clear, unambiguous example of autoresonant Langmuir wave growth using PIC simulations. In PIC simulations, the noise level may be lowered only by increasing the particle number for given physical conditions in the plasma. However, a second source of laser light, introduced at the RHS of the simulation window, may be used to strongly drive a Langmuir wave at a particular point in space and with a particular frequency and wave number (before nonlinear effects shift these values). Using a seed that is significantly stronger than the noise present in the plasma should allow the generation of autoresonant Langmuir waves similar to those presented in the previous chapter using a fluid code (or indeed a prescribed drive model for autoresonance).

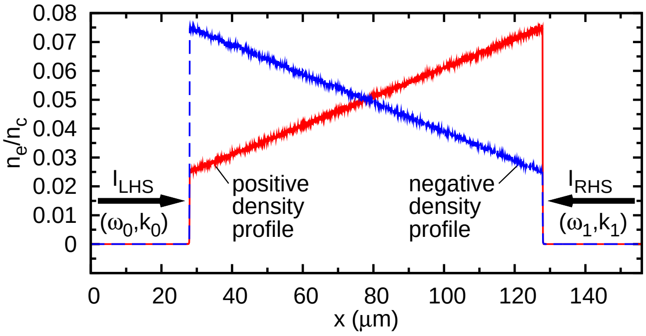

Figure 5.6: Electron plasma density profile for $L = +100$ μm (positive density profile, red solid line) and $L = -100$ μm (negative density profile, blue dashed line). The two counterpropagating laser beams with intensities I_{LHS} and I_{RHS} are introduced *in vacuo* at the LHS and RHS boundaries of the simulation window, respectively.

5.2.1 Langmuir wave amplitude and three-wave phase difference in inhomogeneous plasmas

We now once again introduce a linear density gradient to the plasma of the form

$$n_e = n_0 \left(1 + \frac{x - x_{res}}{L} \right), \tag{5.2}$$

for which $L = \pm 100$ μm for positive and negative density gradients, respectively. The plasma parameters are kept identical to those used in PIC simulations in Sec. 5.1 ($T_e = 1$ keV, $n_0/n_c = 0.05$, $k_L\lambda_D = 0.33$), while the LHS and RHS lasers have intensities $I_0 = I_{LHS} = 5 \times 10^{15}$, $I_1 = I_{RHS} = 1 \times 10^{13}$ W/cm^2 and wavelengths $\lambda_0 = 351$, $\lambda_1 = 473$ nm ($\omega_1/\omega_0 = 0.74$), respectively. The LHS and RHS lasers are switched on at $t = 0$, meeting at the resonance point $x = x_{res} \approx 78$ μm. Since $\omega_0 > \omega_1$, the LHS laser acts as a pump and the RHS laser as a seed, initially resonant with a Langmuir wave at x_{res}. The initial electron density profile is shown in Fig. 5.6.

After the lasers are switched on, they propagate through the plasma until they meet at x_{res} and begin to resonantly drive a Langmuir wave at this point. The evolution of this Langmuir wave is shown in Fig. 5.7 at a series of instances in time. Below, in Fig. 5.8, three-wave coupling simulation results are shown, generated using the same set of parameters as the PIC results above. There is clear autoresonance visible in the PIC simulation results: The amplitude of the Langmuir wave grows along a parabola defined by the cancellation of the wave number detuning due to inhomogeneity and the kinetic nonlinear frequency shift, where

$$\left|\frac{\delta n_e}{n_0}\right| = \left(\frac{c_L \kappa'}{\eta \omega_L}\right)^2 (x - x_{res})^2. \tag{5.3}$$

While the parabola plotted in Fig. 5.7A provides reasonable agreement with the observed growth of the Langmuir wave, the Langmuir wave growth in PIC simulations is slightly steeper than the given parabola. This is not surprising, given the approximate nature of η, but may also be due to a reduction in ω_L due to trapping leading to a steepening of the parabola [the value of ω_L used in calculating c_L in Eq. (5.3) is simply the constant linear value]. Additionally, the parabola plotted is offset from its expected position, with growth beginning slightly behind the intended resonance point. To a lesser extent, this phenomenon is reproduced in three-wave coupling simulations (Fig. 5.7B), caused by the inexact cancellation of the wave number detuning and the kinetic nonlinear frequency shift: The linear growth of the daughter waves is faster than the autoresonant growth until the linear growth becomes saturated, after which autoresonance determines the evolution of the daughter waves. SRS (autoresonant or not) occurs throughout the plasma, but grows more quickly in the region of higher Langmuir wave amplitude produced by the autoresonant growth. Additionally, other frequency shifts are likely present in the plasma (fluid effects such as harmonics, for example), which complicate the situation compared to the simple three-wave coupling model used here.

The three-wave envelope phase difference $\Phi = \phi_0 - \phi_1 - \phi_L$ plotted in Fig. 5.7B was calculated by Fourier analysing each wave. For the Langmuir wave, this process was straight-forward: The real longitudinal field $E_x(x)$ was transformed into k-space. The complex amplitude of the wave was then determined by selecting one half of the distribution in k-space (since the wave propagates in the positive direction, $k_L > 0$ was chosen). The result was then transformed back into x-space and multiplied by the conjugate of the quickly-varying phase of the wave using the linear value of k_L at $x = x_{res}$, giving the complex envelope amplitude of the Langmuir wave. The phase of this wave was then determined by simply taking the argument of the complex envelope and unwrapping the result over the 2π phase range.

The phase of the electromagnetic waves is slightly more difficult to determine, since both real transverse fields overlap in space. The process was similar to that of the Langmuir wave: The real transverse total field (including I_{LHS}, I_{RHS}, all scattered light and noise) was transformed into k-space. The wave numbers of I_{LHS} and I_{RHS}, set at the boundaries of the plasma, were then sufficiently distinct that they could be separated in k-space, in effect isolating each of the forward and backward propagating waves, with care taken to include the shifted wave numbers of the scattered light. The complex wave amplitudes were then

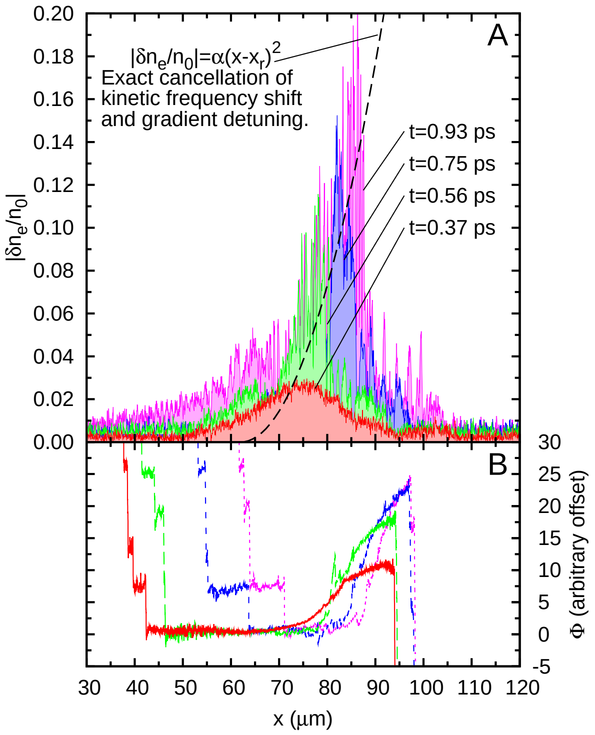

Figure 5.7: The Langmuir wave envelope amplitude and three-wave envelope phase mismatch, calculated from PIC simulations. The Langmuir wave grows along the parabola expected when the nonlinear frequency shift cancels the wave number detuning due to inhomogeneity over a region is space. At x_{res}, $k_L\lambda_D = 0.33$.

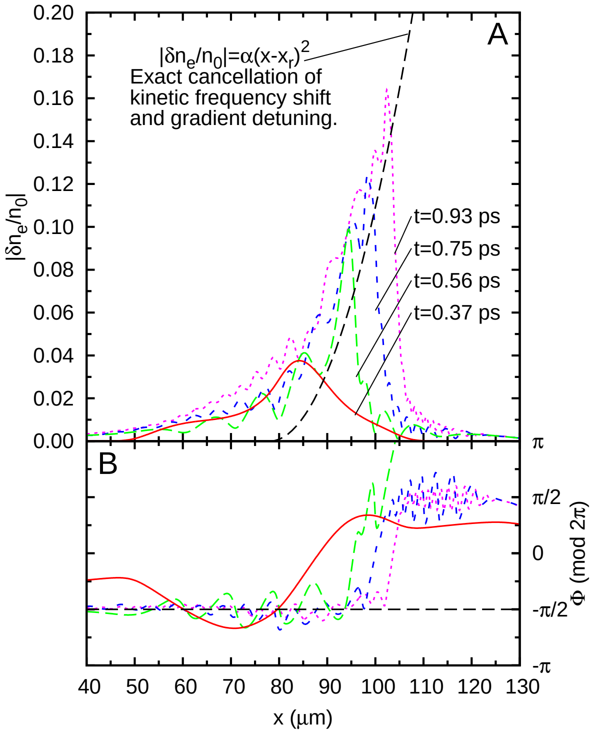

Figure 5.8: The Langmuir wave envelope amplitude and three-wave envelope phase mismatch, calculated using a three-wave fluid code. The Langmuir wave grows along the parabola expected when the nonlinear frequency shift cancels the wave number detuning due to inhomogeneity over a region is space. The three-wave model reproduces the key features present in Fig. 5.7. At x_{res}, $k_L\lambda_D = 0.33$.

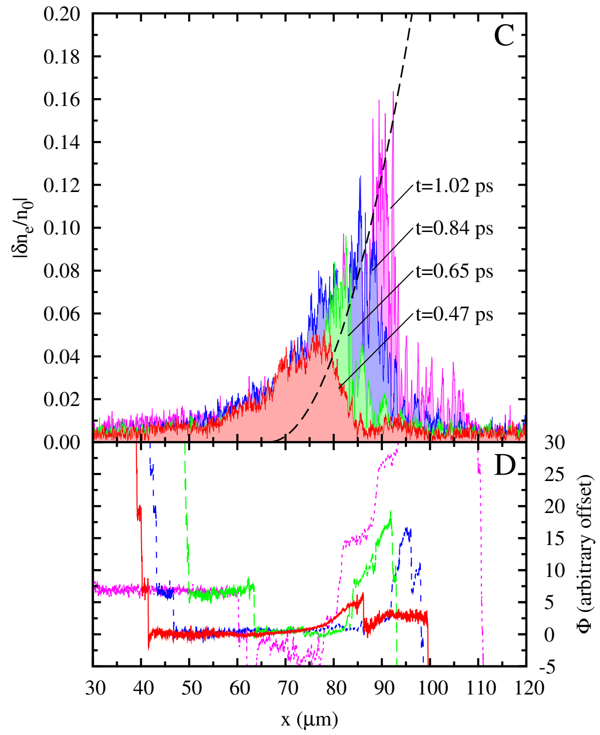

Figure 5.9: The Langmuir wave envelope amplitude and three-wave envelope phase mismatch, calculated from PIC simulations. The Langmuir wave grows along the parabola expected when the nonlinear frequency shift cancels the wave number detuning due to inhomogeneity over a region is space. At x_{res}, $k_L\lambda_D = 0.37$.

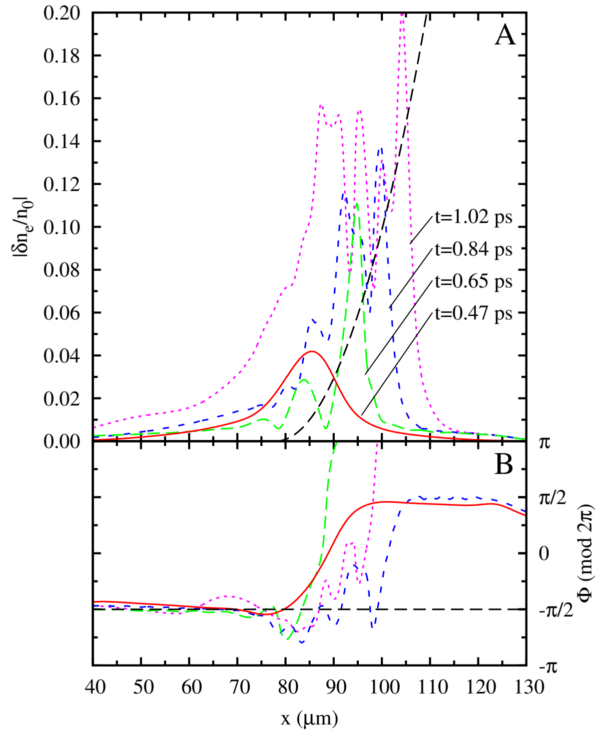

Figure 5.10: The Langmuir wave envelope amplitude and three-wave envelope phase mismatch, calculated using a three-wave fluid code. The Langmuir wave grows along the parabola expected when the nonlinear frequency shift cancels the wave number detuning due to inhomogeneity over a region is space. The three-wave model reproduces the key features present in Fig. 5.9. At x_{res}, $k_L\lambda_D = 0.37$.

multiplied by the conjugate of their quickly-varying phases, giving the complex envelope amplitudes. The phases were then determined by the same method as that used for the Langmuir wave.

The resultant three-wave phase difference is plotted in Fig. 5.7B. Clear phase-locking is visible over a region that extends in space as the autoresonant wave front propagates away from the initial point of three-wave resonance. It should be noted that the apparent glitches in the unwrapping of the phase in Fig. 5.7B are smooth transitions with intermediate points, and are in fact *not* errors. The qualitative behaviour of the phase is essentially unchanged from the that of the three-wave simulations: The three-wave coupling simulation results presented in Fig. 5.8 clearly reproduce the principle features of the kinetic simulations presented in Fig. 5.7, with good agreement found in both the timescale over which the Langmuir wave grows and the amplitude that the Langmuir wave envelope has at a particular time.

In Figs. 5.9 and 5.10, the same quantities are plotted as in Figs. 5.7 and 5.8. All parameters are identical in the two cases but for the profile density, resulting in a different value of $k_L\lambda_D$ at x_{res}; Figs. 5.9 and 5.10 were generated using a profile with $k_L\lambda_D = 0.37$ at x_{res}. The resulting autoresonant Langmuir wave is qualitatively unchanged from the case discussed previously where $k_L\lambda_D = 0.33$ at x_{res}.

5.2.1.1 The electron distribution function during autoresonance

In order to better understand the kinetic processes happening in the plasma, we analyse the distribution of electrons in (x, v_e)-space, where v_e is the local electron velocity. During trapping, we expect that the initially Maxwellian distribution of electrons will form a plateau around the phase velocity v_ϕ at which trapping occurs. The degree of trapping, and the amplitude of this plateau in (x, v_e)-space, should therefore increase with the local amplitude of the Langmuir wave. In Fig. 5.11, the electron distribution function (EDF) is plotted (the local number density has been normalised to 1 in order to remove the change in number density due to the spatial gradient of the electron plasma density) at an instant in time, $t = 0.931$ ps. Due to trapping, the initially Maxwellian distribution is no longer symmetric around $v_e = 0$: at $v_e = v_\phi \approx 0.15$, the distribution function is flattened to form a plateau in (x, v_e)-space, confirming the presence of electron trapping. Beginning just behind the resonance point x_{res}, the plateau increases in size as a function of space, corresponding to the parabolic growth in Langmuir wave amplitude due to autoresonance. In Figs. 5.11B, 5.11C and 5.11D, detail of the distribution function is given. In Fig. 5.11B, the trapping separatrix of the type shown in Fig. 2.3 is visible, showing the closed electron orbits of trapped electrons (compare to Fig. 2.3). This is the case up to and including the autoresonant wave

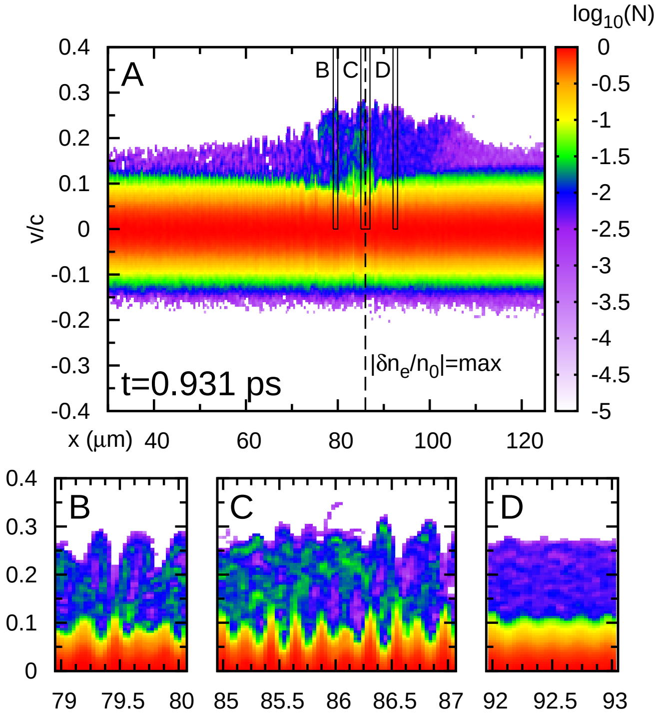

Figure 5.11: The electron distribution function with local normalised particle number N at time $t = 0.931$ ps, calculated from PIC simulations.

front, Fig. 5.11C, where the local Langmuir wave amplitude is at a maximum. Beyond the autoresonant wave front, shown in detail in 5.11D, the phase of the electrons is mixed, signalling the abrupt end of the autoresonant region in phase space.

It is instructive to integrate the EDF over regions in space in order to see a cross-section of the distribution at various points. The integrated EDF is shown in Fig. 5.13, where the integration has been performed over the spatial ranges given in square brackets. It is here clear that both the length in v_e and amplitude in electron number of the plateau increase as a function of distance up until the autoresonant wave front, after which they begin to drop. Inset in Fig. 5.13, the distribution at the autoresonant wave front is shown where the plateau is at its greatest.

5.2.2 Comparison of positive and negative density profiles

Earlier in the chapter in Sec. 5.1, it was confirmed that under the irradiation of a single laser beam, the reflectivity of the plasma is greater when the density increases in the direction in which the laser light propagates, compared to a

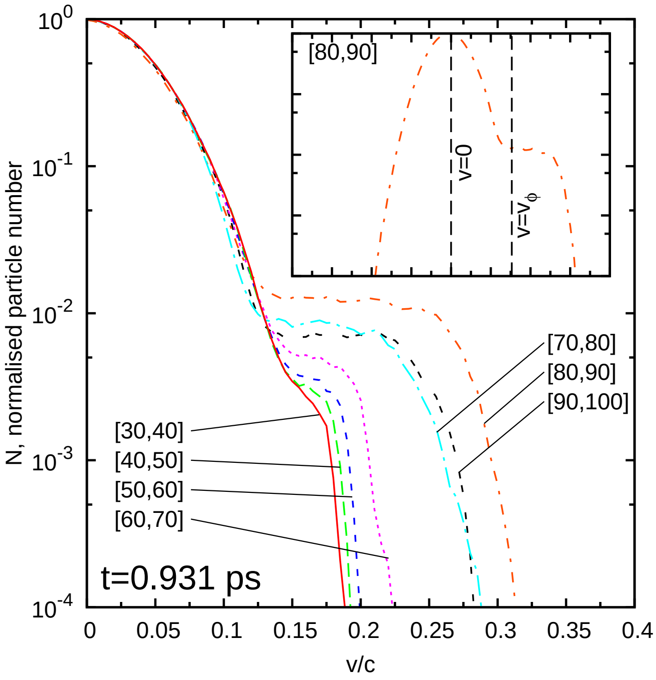

Figure 5.12: The electron distribution function with local normalised particle number N at time $t = 0.931$ ps, integrated over a series of intervals in space, calculated from PIC simulations. The values in square brackets (in μm) show the range over which the integral was performed.

density profile which decreases in the same direction. This behaviour should be observable when, as in the previous section, two laser beams are used to preferentially drive a single autoresonant Langmuir wave envelope.

In Fig. 5.13, the reflectivity of the two plasmas shown in Fig. 5.6 is presented. In Fig. 5.13, the time-averaged reflectivity $\langle R\rangle_t = (1/t)\int^t dt' R$ is shown for positive (red) and negative (blue) density profiles, while inset, the corresponding instantaneous reflectivities are shown. Inset, the seed level injected at the RHS is shown (lower black dashed line), as well as the expected level of the seed after Rosenbluth amplification has taken place near x_{res} (upper black dashed line). Similar to the findings of Sec. 4.1.0.1 (in particular, Fig. 4.3), when the slope of the gradient is negative, the seed intensity I_{RHS} is amplified to a level *below* the level predicted by Rosenbluth in the absence of kinetic effects, $I_0(x = x_L) = I_{RHS}\exp(2G_R)$. When the gradient is positive, the reflectivity is significantly enhanced above the level predicted by Rosenbluth, in agreement with the results of Sec. 5.1 when only the LHS laser was switched on.

Beyond ~ 1.2 ps, the autoresonant wave front shown in Fig. 5.7A does not

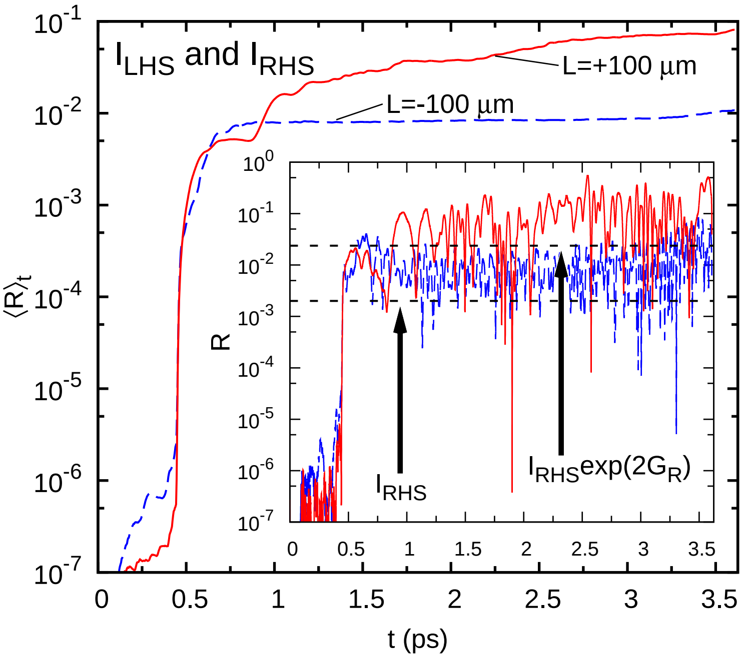

Figure 5.13: The normalised cumulative reflectivity $\langle R\rangle_t = (1/t)\int^t dt'R$ of the plasma with respect to the LHS laser, measured at the LHS of the simulation window as a function of time for positive (red solid line) and negative (blue dashed line) density profiles. Inset, the instantaneous reflectivity is shown.

continue to grow in amplitude as it propagates. Instead, rapid growth is observed over the whole region behind the autoresonant wave front, leading to a further rise in the reflectivity of the plasma (i.e. an increase in addition to the increase occurring during the autoresonant growth of the single strongly-driven mode). The maximum amplitude attainable due to autoresonance of a single mode in kinetic simulations may be limited due to a number of causes, such as:

1. A loss of phase-locking due to the growth of the Langmuir wave, as observed in prescribed drive and three-wave coupling models
2. Damping of the Langmuir wave, as in Fig. 3.4.3
3. Wave breaking, described in Sec. 2.4.4
4. The vanishing of the value of k_L as the Langmuir wave propagates to higher densities

In the autoresonant case, increasing the strength of the LHS (or RHS) laser by a factor of 2 increased the amplitude at which the autoresonant Langmuir wave saturated by a factor of ~ 1.2. In Sec. 3.4.1, an analytic expression for the point at which autoresonance is expected to saturate was derived. Solving Eq. 3.38, we find that we expect no saturation of the autoresonant Langmuir wave due to the disappearance of pseudopotential wells; the Langmuir wave is too strongly driven for the wells to disappear for physical values of the wave amplitude (i.e. $|\delta n_e/n_0| < 1$). This, however, assumes that the damping is negligible, which is almost certainly not the case. It is thus likely that the loss of autoresonance here is due to a combination of factors, such as damping and the onset of wave breaking.

5.3 Chapter summary

For fusion-relevant parameters, the plasma reflectivity is observed to be higher in the kinetic regime when the density increases in the direction in which the pump wave propagates. This holds true whether the pump interacts with noise in the plasma, or whether a high-amplitude counter-propagating seed is used to drive a particular Langmuir wave mode in the plasma. This phenomenon is observed in fluid models, PIC simulations and Vlasov simulations, for a range of densities and plasma conditions. In the case where a single Langmuir wave mode is driven by counter-propagating beams, excellent agreement, both in amplitude and time, is found between kinetic and fluid simulations. The spatial transition from a phase-locked region to a region where the three-wave phase is not locked has also been observed in kinetic simulations.

Chapter 6

Findings and future work

In this chapter, the results of this thesis are summarised. The implications of the findings of this thesis and the future work that these findings motivate is discussed.

6.1 Findings

The mechanism of autoresonance

Spatial autoresonance in SRS in warm plasmas may arise when a nonlinear frequency shift in the frequency mismatch between the coupled waves allows the waves to become phase-locked to the wave number detuning due to the inhomogeneity of the plasma. By modelling the three-wave mismatch in phase in SRS as a particle, the phase-locking mechanism of spatial autoresonance may be understood via an analysis of the Hamiltonian of the particle. In the regime dominated by kinetic effects, it may be shown that any profile with a gradient that increases in the direction in which the driven Langmuir wave propagates (a positive density profile) may support autoresonant Langmuir wave growth.

In the fluid regime, where harmonics of the Langmuir wave provide the dominant shift in frequency away from the linearly resonant mode, a threshold in driver strength (laser intensity) is observed and predicted analytically. Autoresonant growth in this regime, however, is not believed to be of relevance to ICF experiments. In contrast, using parameters corresponding to current ICF experiments at the NIF, autoresonance in the regime where the dominant shift is due to kinetic effects is found to be both possible and potentially important as a mechanism of enhanced Langmuir wave growth, thereby increasing the plasma reflectivity and the generation of hot electrons. Autoresonance in the kinetic regime displays no threshold in driver strength, and may occur in any positive density profile regardless of the plasma conditions.

In the kinetic regime, the cancellation of the wave number detuning due to a linearly inhomogeneous density profile and a nonlinear frequency shift due to electron trapping leads to the parabolic spatial growth of a single mode of the Langmuir wave of the following form:

$$\left|\frac{\delta n_e}{n_0}\right| = \left(\frac{c_L \kappa'}{\omega_L \eta}\right)^2 x^2.$$

The spatial extent of the region over which phase-locking may occur, and consequently the region over which autoresonant growth of the Langmuir wave is possible, is determined by the plasma conditions, density profile and laser intensity. However, regardless of the initial parameters chosen, sufficient growth in Langmuir wave amplitude will cause a loss of phase-locking, but for sufficient driver strength, the level at which this occurs may be so high as to not pose a physical limit on autoresonant growth. For typical parameters relevant to ICF, the amplitude at which autoresonant growth saturates is given by

$$\left|\frac{\delta n_e}{n_0}\right|_{max} = \frac{k_L \epsilon_0}{n_0 e} \left(\frac{1}{2} \frac{\omega_L \eta P}{\kappa' c_L^2}\right)^2.$$

In three-wave coupling, the reflected light may grow, causing P to increase and further raising the maximum attainable amplitude.

Damping reduces the saturation amplitude of the autoresonant growth. A Landau-type nonlinear damping that decreases in time to zero will however not change the eventual saturation amplitude of the Langmuir wave.

Autoresonance in three-wave coupling

Autoresonance does not require a prescribed (constant) driver. In three-wave fluid simulations, autoresonance may arise in a linear density profile, leading to a growth in Langmuir wave amplitude above that which is expected in the absence of nonlinear effects based on Rosenbluth's analysis[20]. At sufficient laser intensities, autoresonant growth is followed by an absolute growth in the plasma, leading to high reflectivities ($R \sim 0.3$) saturated by pump depletion. In a parabolic density profile, autoresonance may also arise. However, at sufficient laser intensities, convective growth other than autoresonance is possible, leading to a strong growth in reflectivity.

The plasma reflectivity

The reflectivity of the plasma is clearly and significantly enhanced when the density gradient increases in the direction of propagation of the high-frequency laser (and thus the direction of propagation of the most strongly-driven Langmuir modes) compared to simulations where the density gradient decreases in the direction of the high-frequency laser propagation. This is observed in simulations both where SRS grows out of noise only and where a single Lanmguir wave mode is driven by counter-propagating beams of differing wavelength. The enhancement in reflectivity is observed in fluid, Vlasov and PIC simulations for a wide range of laser intensities and plasma conditions in the kinetic regime. This enhancement is likely to be present in ICF experiments, where reamplification of scattered light occurs in weakly inhomogeneous plasmas in the hohlraum.

6.2 Future work

Beyond the weakly kinetic regime

Autoresonance and the enhancement of plasma reflectivity in positive density profiles has been observed in the regime $0.3 < k_L\lambda_D < 0.37$. Further studies are required to determine whether the enhancement of plasma reflectivity persists at higher values of $k_L\lambda_D$, well beyond the regime typically regarded as weakly kinetic. Kinetic simulations at lower values of $k_L\lambda_D$ (e.g. $k_L\lambda_D < 0.15$) would also be interesting; it is possible that other nonlinear frequency shifts may produce enhancements in the plasma reflectivity similar to those found in the kinetic regime.

Beyond 1D simulations

PIC simulations in 1D and 2D performed by Masson-Laborde *et al.*[46] suggest that the early evolution of the plasma reflectivity in the kinetic regime is dominated by 1D effects, supporting the 1D treatment given in this thesis. Recent studies by Yaakobi and Frièdland[55] provide examples of autoresonance in 3D in a fluid-like regime, while previous studies by Frièdland[54] have shown that autoresonance is not susceptible to weak transverse nonuniformity in the interacting waves. 2D studies of inhomogeneous plasmas would allow insight into the behaviour of autoresonance in higher dimensions beyond the first saturation ($\sim$ 1 ps) in reflectivity. A 2D fluid code is currently being written and tested, while 2D PIC simulations will be performed in the near future.

The recent work of Albrecht *et al.* (2007)[85], Vu *et al.* (2005)[86] and Bénisti *et al.* (2010)[87] indicate the presence in plasmas of what is referred to by Bénisti as "self-optimisation", Here, a shift in frequency $\delta\omega$ is partially matched by a shift in wave number δk in *homogeneous* plasmas under certain conditions such as a laser intensity that decreases as a function of distance. Many models have been proposed and continue to be developed in order to better describe kinetic effects and find agreement with kinetic simulations, such as those put forward in the last 10 years by Rose and Russell[50], Vu *et al.*[39], Lindberg *et al.*[51] and Bénisti *et al.*[53]. The approach taken in this thesis was similar to that adopted by Vu *et al.*, owing to its suitability for analytic study.

The basic three-wave equations used in this investigation into autoresonance are sufficient for reproducing the initial Langmuir wave growth in kinetic simulations and demonstrating the potential effectiveness of autoresonance. Beyond the first saturation of the reflectivity, the agreement found with kinetic simulations was qualitative at best (a common problem in similar models). Further improvements to the model, drawing on other recent works, and potentially the inclusion of other saturation mechanisms are necessary to move closer an adequate description of the physics contained in kinetic simulations.

Raman amplification

Plasma conditions typical of Raman amplification experiments are such that nonlinear kinetic effects are likely to be of importance. Steep inhomogeneous plasma profiles, of a sort well-suited to the generation of autoresonant Langmuir waves, are also present in experiments. The impact of autoresonance in this case is currently unclear: amplification may be enhanced, but the quality of the amplified pulse may be decreased. Current experimental techniques involve repeatedly passing a pulse through the inhomogeneous plasma, providing many opportunities for autoresonant growth. Future work should address whether considerations of autoresonant behaviour should dictate the shape of the plasma profile.

Appendix

We solve the following three-wave system of equations, relevant to a warm plasma with a linear density profile in the kinetic regime:

$$\mathcal{L}_0 A_0 = -\frac{e}{4m_e}\frac{k_L}{\omega_0}\varepsilon_L A_1, \tag{1}$$

$$\mathcal{L}_1 A_1 = \frac{e}{4m_e}\frac{k_L}{\omega_1}\varepsilon_L^* A_0, \tag{2}$$

$$\left(\mathcal{L}_L + ic_L\kappa' x - i\eta|\varepsilon_L|^{1/2}\right)\varepsilon_L = \frac{e}{4m_e}\frac{k_L}{\omega_L}\omega_{pe}^2 A_1^* A_0. \tag{3}$$

The integration of this system of equations poses a number of problems. First, the three waves propagate at different group velocities. For typical ICF parameters, the Langmuir wave group velocity is much smaller than the group velocity of the EM waves, such that $c_L/c_0 \sim 0.05$. We consider first a reduced problem of the form

$$\mathcal{L}_L \varepsilon_L = 0. \tag{4}$$

Discretising the derivatives, we write

$$\varepsilon_{L_x}^{t+\Delta t} = \varepsilon_{L_x}^{t} - \left(\frac{c_L \Delta t}{\Delta x}\right)(\varepsilon_{L_x}^{t} - \varepsilon_{L_{x-\Delta x}}^{t}). \tag{5}$$

The temporal and spatial steps are given by Δt and Δx, respectively, and the superscripts and subscripts of ε_L denote the points in time and space that are being considered. The quantity typically used to parameterise the accuracy of a finite difference scheme is $c_L\Delta t/\Delta x$, where convergence requires $c_L\Delta t/\Delta x \leq 1$. If $c_L\Delta t/\Delta x \ll 1$, there is a strong numeric damping in the system: in this case, each step forward in time will require the averaging of the complex amplitude at x and $x \pm \Delta x$ (depending on the direction of propagation of the wave and the numeric scheme employed). This damping is particularly detrimental when the propagating wave is shifted in frequency with respect to the frequency of the envelope, as is the case when the profile is inhomogeneous or kinetic effects are included. Indeed, for typical parameters such as those used in this thesis, a Langmuir wave beginning with an amplitude of $|\delta n_e/n_0| = 1$ may only propagate as little as a few microns before being fully damped. Since the length scales over which we require accuracy are of the order of 100 μm, this is clearly unacceptable. The point at which $c_L \Delta t/\Delta x = 1$ is a special value, since at this point, there is no numerical damping in the propagation of the wave: the value of $\varepsilon_x^{t+\Delta t}$ is simply equal to $\varepsilon_{x-\Delta x}^t$, and the scheme is exact. This special case is thus highly desirable. However, since c_L is very different to $c_{0,1}$, it is necessary to use two different spatial meshes for the integration of the EM waves and the Langmuir wave (or two different temporal meshes). The strong frequency shifts used in this work meant that $c_L \Delta t/\Delta x$ had to be extremely close to 1 (Even, for example, $c_L \Delta t/\Delta x = 0.99$ was deemed to have an unacceptably strong numeric damping. A value of $c_L \Delta t/\Delta$ effectively equal to 1 was used in simulations.).

Due to the differing spatial meshes, the coupling term on the RHS of Eq. (3) was necessarily calculated using interpolation. While this again involves averaging two terms of different phase (thereby artificially lowering the strength of the coupling terms), the phase of the EM waves varies slowly in comparison to the Langmuir wave, and the resulting interpolation gives an acceptable level of numeric inaccuracy (this was extensively tested using known results, such as reproducing the analytic result of Rosenbluth gain saturation[20] to within an accuracy of 4 significant figures).

The equation used to solve the equation for ε_L between the boundaries x_L and x_R was the following:

$$\begin{aligned}
{\varepsilon_L}_{x=x_L}^{t+\Delta t} &= 0, && (6)\\
{\varepsilon_L}_{x_L<x\leq x_R}^{t+\Delta t} &= [(1 - c_L\Delta t/\Delta x){\varepsilon_L}_x^t + (c_L\Delta t/\Delta x){\varepsilon_L}_{x-\Delta x}^t \\
&\quad - (\Delta t/2)({\gamma_L}_{x-\Delta x/2}^{t+\Delta t/2}{\varepsilon_L}_{x-\Delta x}^t) \\
&\qquad + \Delta t \Gamma_{Lx}(f_{1x}{A_0}_{x_1'}^t {A_1}_{x_1'}^{*t} + f_{2x}{A_0}_{x_2'}^t {A_1}_{x_2'}^{*t}] \\
&\qquad\quad /[1 + (\Delta t/2){\gamma_L}_{x-\Delta x/2}^{t+\Delta t/2}], && (7)
\end{aligned}$$

where γ_L is the sum of the real damping υ_L and the imaginary frequency shift $\delta\omega$. When the Langmuir wave is at position x, the values of the EM waves used in the RHS coupling must be interpolated. The nearest values of $A_{1,0}$ lie just behind and just ahead of the Langmuir wave at x_1' and x_2', respectively. The relative fractions $f_{1,2}$ relating to positions $x_{1,2}'$ are such that $f_1 + f_2 = 1$. $\Gamma_{Lx} = (ek_L/4m_e\omega_L)\omega_{pe}^2(x)$

is the strength of the coupling at position x. The EM waves were then solved using the well-known Crank-Nicholson method[70].

In the absence of coupling to the electromagnetic waves and damping, but retaining the frequency shift such that $\gamma_L = \delta\omega$, this system reduces to

$$\varepsilon_{L_{x_L < x \leq x_R}}^{t+\Delta t} = \left(\frac{1 - (\Delta t/2)\gamma_{L_{x-\Delta x/2}}^{t+\Delta t/2}}{1 + (\Delta t/2)\gamma_{L_{x-\Delta x/2}}^{t+\Delta t/2}} \right) \varepsilon_{L_{x-\Delta x}}^{t}, \tag{8}$$

where $c_L \Delta t/\Delta = 1$. Thus, in this case, $|\varepsilon_{L_x}^{t+\Delta t}| = |\varepsilon_{L_{x-\Delta x}}^{t}|$, as required. The term gamma must be calculated midway between time and spatial steps to fulfill this condition.

Bibliography

[1] N. B. Meezan *at al.*, Phys. Plasmas. **17**, 056304 (2010). xi, 3

[2] P. Michel *et al.*, Phys. Rev. Lett. **102**, 025004 (2009). xi, 3

[3] Http://en.wikipedia.org/wiki/File:Inertial_confinement_fusion.svg. xi, 4

[4] J. L. Kline *et al.*, Phys. Plasmas. **13**, 055906 (2006). xi, 31

[5] T. M. O'Neil, Phys. Fluids **8**, 2255 (1965). xi, 11, 14, 33

[6] J. Ren, W. Cheng, S. Li, and S. Suckewer, Nat. Phys **3**, 732 (2007). xvi, 89, 90, 91

[7] D. Strozzi, Ph.D. thesis, MIT (2005). xvii, 98, 99

[8] D. W. Forslund and P. D. Goldstone, Spring/Summer Los Alamos Science (1985), available at http://library.lanl.gov/cgi-bin/getfile?00326952.pdf. 5, 6

[9] D. W. Forslund, J. M. Kindel, W. B. Mori, C. Joshi, and J. M. Dawson, Phys. Rev. Lett. **54**, 558 (1985). 6

[10] J. Lindl, Phys. Plasmas. **2**, 3933 (1995). 6

[11] R. W. Short, W. Seka, K. Tanaka, and E. A. Williams, Phys. Rev. Lett. **52**, 1496 (1984). 9

[12] B. Afeyan, M. Mardirian, S. Hüller, and J. Garnier, in *GO5.00013, Abstracts of the APS, Chicago* (2010). 10

[13] P. Kaw, G. Schmidt, and T. Wilcox, Phys. Fluids **16**, 1522 (1973). 10

[14] W. B. Mori, C. Joshi, J. M. Dawson, D. W. Forslund, and J. M. Kindel, Phys. Rev. Lett. **60**, 1298 (1988). 10

[15] H. A. Rose and D. F. DuBois, Phys. Rev. Lett. **72**, 2883 (1994). 10

[16] J. C. Fernández, J. A. Cobble, D. S. Montgomery, M. D. Wilke, and B. B. Afeyan, Phys. Plasmas. **7**, 3743 (2000). 11

[17] S. H. Glenzer *at al.*, Science **327**, 1228 (2010). 11

[18] G. J. Morales and T. M. O'Neil, Phys. Rev. Lett. **28**, 417 (1972). 11, 35, 36, 79

[19] R. L. Dewar, Phys. Fluids **15**, 712 (1972). 11

[20] M. N. Rosenbluth, Phys. Rev. Lett. **29**, 565 (1972). 11, 14, 28, 53, 74, 81, 94, 114, 118

[21] C. V. Raman and K. S. Krishnan, Nature **121**, 501 (1928). 13

[22] G. Landsberg and L. Mandelstam, Naturwissenschaften **16**, 557 (1928). 13

[23] D. F. DuBois and M. V. Goldman, Phys. Rev. Lett. **14**, 544 (1965). 13

[24] C. S. Liu, M. N. Rosenbluth, and R. B. White, Phys. Rev. Lett. **31**, 697 (1973). 14

[25] C. S. Liu, M. N. Rosenbluth, and R. B. White, Phys. Fluids **17**, 1211 (1974). 14

[26] D. F. DuBois, D. W. Forslund, and E. A. Williams, Phys. Rev. Lett. **33**, 1013 (1974). 14

[27] V. E. Zakharov and V. I. Karpman, JETP **16**, 351 (1963). 14

[28] D. W. Forslund, J. M. Kindel, and E. L. Lindman, Phys. Fluids **18**, 1017 (1975). 14

[29] D. W. Forslund, J. M. Kindel, and E. L. Lindman, Phys. Fluids **18**, 1002 (1975). 14

[30] D. Pesme, *Chapitre IV: Introduction aux instabilités parametriques, dans La fusion thermonucléaire inertielle par laser, Edited by R. Dautray and J. P. Watteau* (Eyrolles, Paris, 1993). 22, 30

[31] A. Bers, *Chapter 3.2: Space-time evolution of plasma instabilities - absolute and convective, in Handbook of Plasma Physics, Vol. 1, edited by M. N. Rosenbluth and R. Z. Sagdeev* (North-Holland, Amsterdam, 1983). 25

[32] P. Y. Cheung, M. P. Sulzer, D. F. DuBois, and D. A. Russell, Phys. Plasmas. **8**, 802 (2001). 31

[33] D. F. DuBois, D. A. Russell, P. Y. Cheung, and M. P. Sulzer, Phys. Plasmas. **8**, 791 (2001). 31

[34] R. L. Dewar and J. Lindl, Phys. Rev. Lett. **15**, 820 (1972). 32

[35] T. P. Coffey, Phys. Fluids **14**, 1402 (1971). 32, 34

[36] B. J. Winjum, J. Fahlen, and W. B. Mori, Phys. Plasmas. **14**, 102104 (2007). 32

[37] M. N. Rosenbluth and C. S. Liu, Phys. Rev. Lett. **29**, 701 (1972). 32, 45

[38] O. Yaakobi, L. Frièdland, R. R. Lindberg, A. E. Charman, G. Penn, and J. S. Wurtele, Phys. Plasmas. **15**, 032105 (2008). 32, 38, 45, 46, 58, 60

[39] H. X. Vu, D. F. DuBois, and B. Bezzerides, Phys. Plasmas **9**, 1745 (2002). 34, 36, 116

[40] D. S. Montgomery, J. A. Cobble, J. C. Fernández, R. J. Focia, R. P. Johnson, N. Renard-LeGalloudec, H. A. Rose, and D. A. Russell, Phys. Plasmas **9**, 2311 (2002). 34

[41] J. L. Kline, D. S. Montgomery, B. Bezzerides, J. A. Cobble, D. F. DuBois, R. P. Johnson, H. A. Rose, L. Yin, and H. X. Vu, Phys. Rev. Lett. **94**, 175003 (2005). 34

[42] H. X. Vu, D. F. DuBois, and B. Bezzerides, Phys. Plasmas **14**, 012702 (2007). 34

[43] I. B. Bernstein, J. M. Greene, and M. D. Kruskal, Phys. Rev. **108**, 546 (1957). 35

[44] C. Riconda, A. Heron, D. Pesme, S. Hüller, V. T. Tikhonchuk, and F. Detering, Phys. Rev. Lett. **94**, 055003 (2005). 36

[45] R. L. Dewar, W. L. Kruer, and W. M. Manheimer, Phys. Rev. Lett. **28**, 215 (1972). 36

[46] P. E. Masson-Laborde, W. Rozmus, Z. Peng, D. Pesme, S. Hüller, M. Casanova, V. Y. Bychenkov, T. Chapman, and P. Loiseau, Phys. Plasmas **17**, 092704 (2010). 36, 96, 115

[47] L. Yin, B. J. Albright, H. A. Rose, K. J. Bowers, B. Bergen, D. S. Montgomery, J. L. Kline, and J. C. Fernández, Phys. Plasmas **16**, 113101 (2009). 36

[48] H. A. Rose, Phys. Plasmas **12**, 012318 (2005). 36

[49] H. A. Rose and L. Yin, Phys. Plasmas **15**, 042311 (2008). 36

[50] H. A. Rose and D. A. Russell, Phys. Plasmas **8**, 4784 (2001). 36, 116

[51] R. R. Lindberg, A. E. Charman, and J. S. Wurtele, Phys. Plasmas **15**, 055911 (2008). 36, 116

[52] N. A. Yampolsky and N. J. Fisch, Phys. Plasmas **16**, 072104 (2009). 37, 90

[53] D. Bénisti, O. Morice, L. Gremillet, E. Siminos, and D. J. Strozzi, Phys. Plasmas **17**, 102311 (2010). 37, 116

[54] L. Frièdland, Phys. Plasmas **2**, 1393 (1995). 41, 115

[55] O. Yaakobi and L. Frièdland, Phys. Plasmas **15**, 102104 (2008). 41, 115

[56] J. Fajans and L. Frièdland, American Journal of Physics **69**, 1096 (2001). 42, 54, 58

[57] E. M. McMillan, Phys. Rev. **68**, 143 (1945). 44

[58] V. I. Veksler, J. Phys. (USSR) **9**, 153 (1945). 44

[59] A. Loeb and L. Frièdland, Phys. Rev. A **33**, 1828 (1986). 44

[60] O. Naaman, J. Aumentado, L. Frièdland, J. S. Wurtele, and I. Siddiqi, Phys. Rev. Lett. **101**, 117005 (2008). 44

[61] A. Ghizzo, P. Bertrand, J. Lebas, T. W. Johnston, and M. Shoucri, Phys. Plasmas **5**, 4041 (1998). 45

[62] G. B. Andresen *et al.*, Phys. Rev. Lett. **106**, 025002 (2011). 45

[63] A. V. Maximov, R. M. Oppitz, W. Rozmus, and V. T. Tikhonchuk, Phys. Plasmas **7**, 4227 (2000). 45

[64] E. A. Williams *et al.*, Phys. Plasmas. **11**, 231 (2004). 45

[65] P. Khain and L. Frièdland, Phys. Plasmas **17**, 102308 (2010). 45

[66] L. Friѐdland, P. Khain, and A. G. Shagalov, Phys. Rev. Lett. **96**, 225001 (2006). 45

[67] G. B. Whitham, *Linear and Nonlinear Waves* (Wiley, New York, 1974). 54

[68] L. Friѐdland, Phys. Rev. E **55**, 1929 (1997). 54

[69] L. Friѐdland, Phys. Rev. E **59**, 4106 (1999). 54

[70] J. Crank and P. Nicolson, Advances in Computational Mathematics **6**, 50 (1996). 70, 119

[71] D. Bénisti and L. Gremillet, Phys. Plasmas. **14**, 042304 (2007). 77

[72] D. Bénisti, D. J. Strozzi, and L. Gremillet, Phys. Plasmas. **15**, 030701 (2008). 77

[73] D. Bénisti, D. J. Strozzi, L. Gremillet, and O. Morice, Phys. Rev. Lett. **103**, 155002 (2009). 77

[74] D. Bénisti, O. Morice, L. Gremillet, E. Siminos, and D. J. Strozzi, Phys. Plasmas. **17**, 082301 (2010). 77, 78

[75] G. Picard and T. W. Johnston, Phys. Rev. Lett. **51**, 574 (1983). 81

[76] T. W. Johnston *et al.*, Plasma Phys. Control. Fusion **27**, 473 (1985). 81

[77] T. Fouquet and D. Pesme, Phys. Rev. Lett. **100**, 055006 (2008). 81

[78] G. Shvets, N. J. Fisch, A. Pukhov, and J. Meyer-ter Vehn, Phys. Rev. Lett. **81**, 4879 (1998). 88

[79] V. M. Malkin, G. Shvets, and N. J. Fisch, Phys. Rev. Lett. **82**, 4448 (1999). 89

[80] J. Ren, S. Li, A. Morozov, S. Suckewer, N. A. Yampolsky, V. M. Malkin, and N. J. Fisch, Phys. Plasmas **15**, 056702 (2008). 89

[81] N. A. Yampolsky and N. J. Fisch, Phys. Plasmas **18**, 056711 (2011). 89, 91, 92

[82] V. M. Malkin, G. Shvets, and N. J. Fisch, Phys. Rev. Lett. **84**, 1208 (2000). 90

[83] N. A. Yampolsky and N. J. Fisch, Phys. Plasmas **16**, 072105 (2009). 90

[84] H. Okuda, J. of Comp. Phys. **10**, 475 (1972). 95

[85] M. Albrecht-Marc, A. Ghizzo, T. W. Johnston, T. Rveill, D. D. Sarto, and P. Bertrand, Phys. Plasmas **14**, 072704 (2007). 116

[86] H. X. Vu, L. Yin, D. F. DuBois, B. Bezzerides, and E. S. Dodd, Phys. Rev. Lett. **95**, 245003 (2005). 116

[87] D. Bénisti, O. Morice, L. Gremillet, E. Siminos, and D. J. Strozzi, Phys. Rev. Lett. **105**, 015001 (2010). 116